# Biologically-inspired Motion Control for Kinematic Redundancy Resolution and Self-sensing Exploitation for Energy Conservation in Electromagnetic Devices

by

Vahid Babakeshizadeh

A thesis

presented to the University of Waterloo

in fulfilment of the

thesis requirement for the degree of

Master of Applied Science

in

Mechanical and Mechatronics Engineering

Waterloo, Ontario, Canada, 2013

I hereby declare that I am the sole author of this thesis. This is a true copy of the thesis, including any required final revisions, as accepted by my examiners.

I understand that my thesis may be made electronically available to the public.

# Abstract

This thesis investigates particular topics in advanced motion control of two distinct mechanical systems: human-like motion control of redundant robot manipulators and advanced sensing and control for energy-efficient operation of electromagnetic devices.

Control of robot manipulators for human-like motions has been one of challenging topics in robot control for over half a century. The first part of this thesis considers methods that exploits robot manipulators' degrees of freedom for such purposes. Jacobian transpose control law is investigated as one of the well-known controllers and sufficient conditions for its universal convergence are derived by using concepts of "stability on a manifold" and "transferability to a sub-manifold". Firstly, a modification on this method is proposed to enhance the rectilinear trajectory of the robot end-effector. Secondly, an abridged Jacobian controller is proposed that exploits passive control of joints to reduce the attended degrees of freedom of the system. Finally, the application of minimally-attended controller for human-like motion is introduced.

Electromagnetic (EM) access control systems are one of growing electronic systems which are used in applications where conventional mechanical locks may not guarantee the expected safety of the peripheral doors of buildings. In the second part of this thesis, an intelligent EM unit is introduced which recruits the self-sensing capability of the original EM block for detection purposes. The proposed EM device optimizes its energy consumption through a control strategy which regulates the supply to the system upon detection of any eminent disturbance. Therefore, it draws a very small current when the full power is not needed. The performance of the proposed control strategy was evaluated based on a standard safety requirement for EM locking mechanisms. For a particular EM model, the proposed method is verified to realize a 75% reduction in the power consumption.

# Acknowledgments

I would like to express my warmest appreciations to my supervisor, Professor Soo Jeon, from whom I learned priceless lessons and to whom I will remain sincere and indebted for ever. He taught me lessons by his scintillating insight, intelligence, genuineness, and authenticity. I will try my best to follow his professionalism, humility, understanding, and considerateness.

I would like also to thank professor Dong Eui Chang and professor Mir Behrad Khamesee for their invaluable comments on my thesis.

I would like to acknowledge technical staff in Rutherford Controls Int'l for their help and continuous support during the project. I would like to thank specially Ryan McMillan, Nima Talebi, and Mandeep Singh for their affable assistance through different stages of testing and their insight into every problem I faced.

I would like to express my respect and thankfulness to technical staff at the University of Waterloo for their support during implementation stages of my project. I want to thank Neil Griffett, Chris McClellan, James Merli, Andy Barber, and Mark Griffett for their help during electronic circuit implementation.

I also thank my fellow office members Kamal, Olabanjo, Hyunki, Bonghun, Ahmet, and Ammar for being such awesome friends.

I would like to thank my parents for being always besides me while distant. I would like to thank everyone who has contributed even a minute part in my success and progress.

*To my mother...*

*whose love is to be not forgotten,...*

*whose passion for my success no one can describe,...*

*and who has hitherto never stopped worrying about my concerns,...*

*and to my father...*

*who stands against difficulties with his soul and body...*

*to protect his family against all possible discomfort,...*

*and who has been generous in love,*

*patient on my obstinance,*

*and forgiving on my proud.*

# Contents

# List of Figures

# List of Tables

# Chapter 1

# Introduction

In this thesis, two mechanical systems are investigated from distinctive points of view of redundancy resolution: robot manipulators and electromagnetic (EM) blocks. The latter deals with eliminating redundant energy consumption in EM systems while the former is more concerned with kinematic redundant degrees of freedom in robotic manipulators.

## 1.1 Biologically-inspired Motion Control for Kinematic Redundancy Resolution

This section reviews previous works on robot control and introduces the Bernsteîn's degree of freedom (DOF) problem. Different approaches to this problem have been reviewed which are proposed by researchers in various fields from Robotics to Neurobiology. This section ends with general characteristics of a universal controller that resembles brain-like control laws.

### 1.1.1 Redundancy in Robot Manipulators

To satisfy the minimum task requirements, the mechanical system is required to possess a sufficient number of DOFs. When this condition is not satisfied, the control problem becomes ill-posed. In the case of robot manipulators, ill-posedness is often defined as the situation where the solution of the inverse kinematics from the task space to the joint space is not unique. The problem is said to be mathemati-

cally ill-posed as a consequence of indeterminacy in the system. In this case, the target point can be reached with different final configurations of the manipulator that constitute the uncontrolled manifold of the desired point [1]. This situation occurs when the number of DOFs in the task space is less than that in the joint space. One such manipulator is called a "*Redundant Manipulator*".

Surplus DOFs add to the dexterity of the motion as well as variability of the system. Variability has been studied in different fields by introducing the concepts of uncontrolled manifold [1], equilibrium-point manifold [2], self-motion manifold [3, 4], and goal-equivalent manifold [5] all of which are based on a similar concept. They all define a manifold for all joint-space configurations of the system with respect to a unique point in the work space of the robot. This introduces the concept of variability in redundant robot motions which is defined as the convergence to the target point with different final configurations. As there are an infinite number of solutions in the inverse kinematics of redundant manipulators, the reaching tasks can be fulfilled by different final gestures of the system which may differ from one trial to other. All the configurations are acceptable as long as the task-space configuration of the robot converges to the desired task space target point [1].

Excess DOFs of redundant manipulators introduce the opportunity to modify the motion through an optimization problem which selects the best configuration towards task accomplishment. Object avoidance [6, 7, 8, 9], energy consumption minimization [10, 11], time optimal reaching [12, 13], jerk minimization [14], trajectory tracking [15], and singularity avoidance [16, 17] are some of the optimization criteria which utilize self-motions in the null-space of the manipulator to accomplish the primary task along with satisfying a set of secondary criteria. Since these criteria exploit surplus DOFs of the system, they cannot be implemented on non-redundant manipulators.

### 1.1.2 Bio-inspired Robotics and Bernsteîn's Degree of Freedom Problem

Biological organisms possess a high number of DOFs compared to the required number of DOFs in a three-dimensional world. Therefore, almost all animals own kinematically-redundant limbs which increase their freedom and flexibility of motion. This, along with amazing manoeuvrability in animals' movements, motivated many researchers to study such motions and design biologically-inspired robotic systems.

The biologically-inspired motion control of robotic systems has been recently under special attention among researchers. Human and animal body motions demonstrate the existence of an optimal controller that produces body limb movements with high efficiency in different aspects: energy efficiency, optimized trajectory, time optimality, etc. The study of human hand-arm motions, specifically, has been of special interest to researchers in various fields. The main problem under investigation is how the human brain controls over many DOFs involved in the motion. Human hand-arm system, for example, possesses eleven DOFs from shoulder to finger tips. Considering the DOFs involved from torso, this number increases to more than one hundred [18]. This problem has been investigated from different points of view including the performance of central nervous system (CNS) on control and operation of body limbs. The ability of human brain to handle the complications of controlling such a complex system in a timely-efficient manner initiated countless studies on Brain Research and Biology [19], Neuroscience [20], Developmental Psychology and Physiology [21], and Robotics [22].

#### 1.1.2.1 Bernsteîn's Degree of Freedom Problem

Over half a century ago, Nikolai Aleksandrovich Bernsteîn posed a question about the interactions between CNS and human body. The question cast doubt about the existence of any explicit motor control pattern (motor coordination) adopted by CNS to control body motions. Motor coordination is defined as the process of converting the complex structure of moving organs into a controllable system and

dominating the motion of redundant DOFs of the body limbs [23]. As there are a multitude of possibilities for human body movements, Bernsteîn broached the topic of motor coordination by nervous system and how acceptable choices among countless movements for accomplishing one specific task can be selected by brain with comparatively short processing times [23, 24]. He claimed that an explicit relationship between CNS signals and body movements does not and cannot exist as it should include not only the complexity of the control problem, but also its time optimality [25].

#### 1.1.2.2 Resolutions to Bernsteîn's Degree of Freedom Problem

Since the problem introduction, different hypotheses and strategies were proposed to resolve the Bernsteîn's challenging statement. Bernsteîn, himself, considered the case of human hand-arm motion and indicated that planning and controlling complicated movements like human multi-joint motions may not include all DOFs involved in the task. He proposed that some DOFs are freezed and ignored at a time; hence brain deals with fewer DOFs for the first stages of the task; and it recruits more DOFs in the last stages of movements [24]. However, holding variables unchanged during the course of multi-joint actions is not a trivial task and cannot be associated with "easy control". An argument against this hypothesis was discussed in [2] indicating that freezing some of the DOFs does not change the number of DOFs within a motor task. Therefore, even under Bernsteîn's supposition, system's dynamics and control retain their complexity.

To resolve multi-joint-motion problems in systems with surplus DOFs, two strategies may be adopted: decreasing the number of independent elemental variables (i.e. joint angles); or increasing the number of specified spatial/performance variables [26]. The latter can be accomplished by employing some performance criteria for optimization of the motion with respect to predefined motion requirements. The former strategy may recruit constraints on the joint variables with respect to each other by defining synergistic functions relating the joint space variables.

An example of the first strategy is introducing the concept of muscle synergies [27, 28, 29, 30]. Synergy is referred to a class of movements in human motor control system that is employed for fulfilling different tasks. Muscle synergies allow CNS to control the motion by taking into account a limited number of joint variables [2, 19, 31]. This was assumed to be a potential resolution for human brain ability for efficient motion control. However, instead of considering them as a strategy to simplify the control, synergy is suggested to be considered as a close interaction between properties of musculoskeletal system and neural control strategies. Muscle synergies were also argued against in virtue of several experimental results [32]. In [32], several cases were discussed in support and in opposition of muscle synergies. That is, this concept may not represent a complete scope of brain's activities to control body limbs.

The employment of performance indices for defining new performance variables are widely used in Robotics literature. The appended variables are employed to optimize the performance of the system and to introduce a more human-like motion to the robotic system; therefore, rendering a motion with human-skilled characteristics. This type of control belongs with the second category of control methods which are scrutinized further in the next section.

#### 1.1.2.3 Human Hand-Arm Movements

Structural resemblance of robot manipulators to human arm introduced a topic in Robotics literature: *Human-like hand-arm motion*. Robots with human-like motion would offer enhanced dexterity, efficiency, and performance. Designing a controller that renders the robotic system a human-like motion first requires defining the main criteria of such a natural motion. Experiments on human arm motions discovered invariant characteristics [21]. Specifically, for regulation problems in the task space, general characteristics of human-skilled multi-joint movements are as follows [33, 34, 35, 36].

1. The profile of the end-effector trajectory in the task space is nearly rectilinear.

2. The velocity profile of the end-effector in the task space becomes symmetric

and bell-shaped

3. The acceleration profile has double peaks

4. The profile of joint angles and angular velocities may be different for different joints

Finding a promising controller design, however, requires dominance on different aspects of the interactions between human nervous and musculoskeletal systems. Nonetheless, perceived dynamic characteristics of the point-to-point reaching movements introduced countless hypotheses in regard to dynamic and kinematic control of redundant manipulators. These controllers either take into account potential control strategies adopted by human brain or define performance criteria to generate predetermined characteristics of the arm motion through optimizing indices.

### 1.1.3 Control of Redundant Manipulators

Control of robot manipulators can be formulated in either the dynamics level or kinematics level of the system. Dynamics-level control calculates joint torques required to achieve the control objective whereas a kinematics-level control design computes the desired kinematic properties of the motion such as joint velocities and joint accelerations. Despite the difference in their strategy, the controller design involves some standard elements which construe robot structure. The controller design for a redundant manipulator can be decomposed in two parts. One part may have the same structure of a controller as if the robot is non-redundant and the other part is designed for performance optimization.

#### 1.1.3.1 General Approach to Redundancy Resolution Based on Manipulator Jacobian

To control robot manipulators, there have been many controller designs proposed for different applications. Jacobian matrix is a fundamental element used in most

of the proposed controllers. This matrix is defined as

$$J_{ij} = \frac{\partial x_i}{\partial q_j} \tag{1.1}$$

where $J_{ij}$ is the component of the Jacobian matrix on the $i^{th}$ row and the $j^{th}$ column, $x_i$ is the $i^{th}$ task-space coordinate, and $q_j$ is the $j^{th}$ joint-space variable. Jacobian matrix relates the velocities in the task space to those in the joint space as follows.

$$\dot{x} = J\dot{q} \tag{1.2}$$

Therefore, desired motions in the joint space of the robot can be related to the corresponding velocities in the task space via a translation with Jacobian matrix as the mapping function. The inverse Jacobian matrix is correspondingly used for control purposes where desired task-space velocities are given. In this case, the respective velocities in the joint space of the system can be calculated as

$$\dot{q} = J^{-1}\dot{x} \tag{1.3}$$

where $J^{-1}$ denotes the inverse of the Jacobian matrix.

For redundant robot manipulators, as the Jacobian matrix is a non-square matrix, pseudo-inverse Jacobian matrix, [37], can be used as

$$\dot{q} = J^{\dagger}\dot{x} \tag{1.4}$$

where $J^{\dagger}$ is the pseudo-inverse Jacobian derived through an optimization problem and computed as

$$J^{\dagger} = J^T(JJ^T)^{-1} \tag{1.5}$$

with $J^T$ being the transposed Jacobian matrix.

Jacobian matrix and its (pseudo-)inverse are used for projecting the gradient vector of a performance index onto the null-space of the manipulator. This projected vector can augment the controller design for self-motion exploitation of the system for optimization of the performance index. The performance functional introduces constraints on the system; thus, increasing the number of specified spatial variables besides desired spatial coordinates for the end-effector [26]. Design of

such constraints depends on the expectations from the controller. The performance indices are commonly designed as a potential function achieving whose extremums (usually minima) is desired. As an instance, since controlling robot manipulators near singular points becomes more difficult due to degeneracy of Jacobian matrix, manipulability- as a measure of the ability of the robot for manipulation- can be used for singularity avoidance [38, 39]. One such performance index attempts to prevent robot configuration to approach singularities.

The general structure of the augmented controller in the kinematics level can be given as

$$\dot{q} = J^{\dagger}\dot{x} + (I - J^{\dagger}J)\varphi \tag{1.6}$$

where $I$ is the identity matrix, $\varphi$ is the optimizing vector, and the last term on the right presents the projection of $\varphi$ to the null space of the Jacobian matrix. $\varphi$ can be designed as the gradient of an objective function or based on some predefined constraints to the system.

As working with (pseudo-)inverse matrices is computationally expensive, various studies considered transposed Jacobian matrix as a substitution for (pseudo-)inverse Jacobian. It has been also investigated that Jacobian transpose and inverse Jacobian can be both employed in the controller interchangeably. This quality is referred to as *duality property* [40]. One advantage of using Jacobian transpose instead of (pseudo-)inverse Jacobian is its simple process of calculation that eliminates a large portion of required computational processes involved in calculating (pseudo-)inverse Jacobian; therefore, increasing the speed of control process.

Jacobian transpose is a mapping for the generalized forces from the task space to the joint space, i.e.

$$\tau = J^{T}F, \tag{1.7}$$

where $\tau$ is the vector of joint torques and $F$ is the force vector in the task space applied to the end-effector. This property introduces the application of Jacobian matrix for dynamics-level robot control. Exploitation of Jacobian transpose has been investigated for different problems such as regulation problems [22, 41] and

trajectory planning applications [42]. Similar to (pseudo-)inverse Jacobian control laws, performance indices can be added to the transposed Jacobian control law, as well. The corresponding task-space regulator can be designed as

$$u = -C\dot{q} - J^T K(x - x_d) + (I - J^\dagger J)\varphi \tag{1.8}$$

where $u$ is the vector of joint torque control signals, $C$ is a damping matrix, $K$ is a positive-definite gain matrix, representing the stiffness matrix of virtual springs attached to the end-effector, $x$ is the task-space position of the end-effector, and $x_d$ is the coordinate vector of the target point in the work space of the manipulator. The first two terms are in fact a task-space PD controller with damping shaping [43]. The second term is the gradient of the potential function $U = \frac{1}{2}\Delta x^T K \Delta x$, with $\Delta x = x - x_d$, mapped to the joint space torques by Jacobian transpose, and the last term is the performance index projected on the null-space of the Jacobian matrix

#### 1.1.3.2 Control for Human-like Motion

Human-like control approaches consider either satisfying the dynamic or kinematic properties of the motion or evaluating possible control strategies adopted by human brain. The latter attempts to produce the motion by modelling the interaction between CNS and sensory-motor system in human body. The former focuses, exclusively, on generating very well-known motion characteristics by exploiting excess DOFs of the system.

Experiments on body motions in children and adults initiated the hypothesis that instead of a "*computational*" control method, human beings "*learn*" how to control over their body limbs. The applications of reinforcement learning and iterative learning for human-like robot control emerged upon such hypotheses. Experimental results showed a difference in the mastery level of motion in children and adults [33]. This proposes that brain may make decisions based on previous experience which is developed through the course of life. Therefore, motor coordination is not inherently determined by CNS but it gradually evolves during postpartum life [26]. During this continuous learning process, brain develops its

policy to select the best course of action. Therefore, adults, unlike children, do not require a high level of physical or computational effort to accomplish a task. These methods suggest a reduced level of attention to the movement by an adept operator. Application of reinforcement learning, iterative learning, and neural network methods for controlling arm movements showed some potential to create such algorithms [44, 45, 46, 47].

Control methods based on artificial intelligence of the system are developed through experiencing one specific task with reward-weighted results. This process continues until the corresponding policies of the task converge to their optimal values. The convergence time depends on the complexity of the task, rewards, and the objectives; and it may take too long. Methods that offer explicit controllers for rendering redundant manipulators a human-like motion, on the other hand, represent the interaction between CNS and musculoskeletal systems through explicit controller designs.

Segmentation of joints during different stages of the movement was suggested as an approach human brain adopts during arm movements [48]. In this study, the hand-arm system was modelled as a redundant four-link planar manipulator, where the first two joints correspond to shoulder and elbow, and the last two joints are wrist and the index finger. A rigorous mathematical analysis was conducted using adaptive weighting functions to adjust the allocation of the reaching tasks for each joint during the motion. It was suggested that, during the first stages of the motion, shoulder and elbow joints mainly contribute to the reaching by producing large movements. As the end-effector approaches the target point, the last two joints' contribution increases. Small movements correspond to more accurate reaching at the last stages of regulation. If we relate the accuracy of movement to the attention to control, small movements can correspond to higher levels of attention. This suggests that, at the beginning of the motion, attention to control is minimum and it increases close to the target point. Interestingly, this resembles Bernsteîn's hypothesis of DOF freezing. Nonetheless, here the attention to the motion of each

joint is adjusted by an adaptive function of distance to the target point; and thus, controlling all joints start from the beginning of the motion.

Task-space PD controller is one of the simplest controllers which was first introduced for controlling non-redundant manipulators [43]. Equation (1.8) with $\varphi = 0$ represents one such controller, i.e. a simple Jacobian transpose control law without any performance index. The controller design in this case is the derivative of a potential function whose minimum is located at the target point. Artificial potential function can be designed for variety of tasks such as obstacle avoidance [49], and arbitrary path planning and field tracking [50, 39]. In the case of a simple Jacobian transpose method, the controller consists of a viscous damping term along with the gradient vector of the spring-like potential function: $U = \frac{1}{2}\Delta x^T k \Delta x$, which is basically a steepest descent optimization algorithm to find the minimum of the potential function.

Due to the simplicity of the simple Jacobian transpose method, it requires a low level of computation. Application of this controller was also evaluated for human-skilled multi-joint reaching movements. Instead of considering the surplus DOFs and how to resolve the redundancy of the system, this method proposes that human brain ignores them and let the redundancy comply with the variability of the system [51]. In other words, instead of confining the final joint-space configuration of the robot to a set of predefined values, the controller allows the dynamics of the system to determine the best naturally-compliant values. A dynamics-compliant controller was also discussed based on a differential geometry approach [52, 53]. It confirmed that the characteristics of human arm movements can be observed by exploiting inertia-originated movements of multi-body systems based upon an optimization problem on the Riemannian distance in the joint space. This study shows the applicability of this idea for human arm movements and biped walking. It can be concluded that dealing with the complexity of controlling nonlinear dynamics of the system is naturally performed by the dynamics of the system itself.

### 1.1.4 A Universal Control Law

Saccadic eye-movements and arm reaching movements share similar characteristics in terms of trajectory and velocity profiles [19, 54]. Therefore, a unified strategy must be governing most of the control laws that human brain exploits. The structure of motor coordination is different for eye movements and arm movements. Hence, besides quantitative aspects of control which relate to the dynamics and kinematics of the movement, there must exist universal qualitative measures of movement which is controlled by human brain.

For a skilled operator, sensory functions contribute more into the human control laws and brain activities than the attention to the motor control cortex inside the brain [55, 56]. That is, brain tends to not attend to the control process. This agrees with the conclusions from learning methods and many satisfactory explicit controllers [22]. Attention to control can be looked as a quality that is governed by human brain policies during body limbs' motions. Optimizing the attention to the control process can be realized through a minimum-attention controller. Minimum-attention controller was introduced as a controller that tends not to change the control signals during the course of action [57]. The minimum-attention control aims to design a control input whose deviation from a constant control is minimized and thus the controller does not require an intensive computation. Promising performance of minimum-attention control has been approved in networked systems with limited communications or to reduce the computational cost of control [58, 59]. However, in the control of redundant robot manipulators, this controller has been disregarded.

A relatively similar objective to minimum attention is minimum-jerk control [60]. Minimum-jerk control models consider (1.6) where $\varphi$ is designed by using the third-order time-derivative of the joint angles as the objective function. This control law attempts to reduce any change in the joints acceleration by minimizing the jerk in the system. It was shown that this method produces rectilinear trajectories of the end-effector and a symmetric bell-shaped velocity profile [61].

The outcomes of the literature in human-like movements suggest the following conclusions about the characteristics of a potential controller:

1. The basic invariant human-like characteristics in hand-arm movements should be accomplished.

2. The controller should not require heavy computational processes.

3. The controller should exploit the dynamics of the system for accomplishing the task.

4. The controller does not need to take into account the whole complexity of the system as long as the reaching is concerned.

5. The attention to control should be adjusted through the course of action such that a minimum attention is paid to the process.

## 1.2 Self-sensing Exploitation for Energy Conservation in Electromagnetic Devices

The simplicity and convenience of utilization of DC electromagnets have made them an integral part of various industrial devices such as relays, valves, switches, etc. [62]. Recently, EM devices have taken in the place of conventional mechanical blocks because of their fully electronic operation. This is specifically more appealing in applications where an off-site central system is used to manage the security or control the performance of such systems. For example, EM locking mechanisms constitute the basic structure of access control systems where mechanical locks used to be recruited [63, 64].

In spite of the increasing popularity of EM locks, a potential issue exists in their operation which gets recognized more and more, recently. In the normal operational mode, where power is on for operation and off otherwise, an EM device requires continuous supply of electric power to function properly. EM locking mechanisms, for instance, need to consume the full power even if no one really attempts to open the door [65]. Despite the fact that their power consumption may be far less than that of conventional light bulbs, the power loss may not be negligible in a long term use. This is more concerned in applications where the device is hardly affected by the surrounding environment: where the full strength of the system is not always required for successful operation; but special circumstances ask for the full power/strength.

### 1.2.1 Motivation and Approach

Buildings account for a major portion of the world's energy consumption [66]. Thus, conserving energy used in buildings holds a great potential for economic and environmental success [67]. For electrical devices, energy saving can be realized by modifying the system design, improving system's performance, or introducing new alternatives (e.g., time scheduling modification [68], supply adjustment [69], use of renewable energies [70], and the exploitation of natural resources [71]).

The literature on EM devices abounds with many studies about appending the system with an equipment for enhancing the performance of the system or increasing its safety/security [72, 73, 74, 75]. However, energy conservation studies are relatively few for the family of DC electromagnets. In this part of thesis, a new design of EM locks operating in DC voltage mode is synthesized from the energy conservation point of view. The EM locks considered in this study are configured to require the full power only in specific circumstances when there is an attempt to break in. This study, then, incorporates the idea that energy-efficient EM systems can be realized by recruiting a self-sensing technique to detect any undesirable external disturbance applied to the system that may violate the minimum levels of the safety in the system. The EM system can then be used in a semi-idle state with a very low effective holding strength most of the time; and the full power is applied only when is needed. Figure 1.1 illustrates a schematic of the proposed control strategy.

### 1.2.2 Requirements and Challenges

Satisfactory performance of an energy-efficient EM device, as introduced here, requires several consecutive tasks to be completed in a timely manner. External disturbances which alters the safe state of the system need to be detected by a fast detection mechanism as any delay in the performance of such mechanism may result in a deficient performance of the system. After the change is detected, a reliable activation process is required to transfer the system into a secure state. This activation process needs to deal with the inductive behaviour of the solenoid coil and compensate for the corresponding delays. Finally, the system is transferred to a restoration mode that assures the safety of the system with the minimum required electrical energy. Timing plays an important role in the first two stages of this control process. Therefore, the techniques which are designed for these two stages are very crucial in satisfactory performance of the energy-efficient EM system.

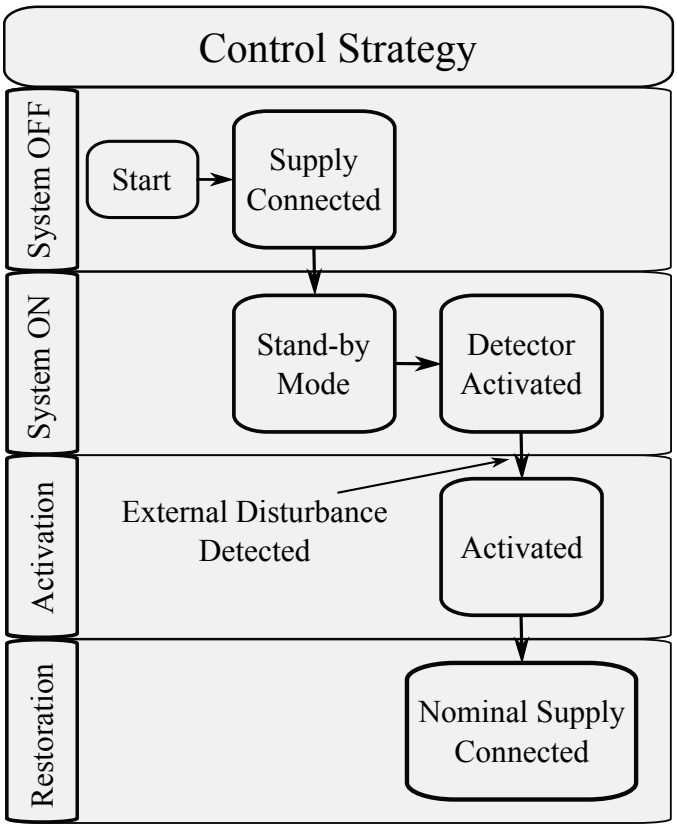


Fig. 1.1: Flowchart of the control strategy

#### 1.2.2.1 Detection of external disturbances

The speed of detection process and the complexity of its implementation and analysis are the main elements that affect the practicality of the method and ensure simple integration of the appended intelligence to the system. Therefore, a sophisticated sensing means needs to be employed that offers an optimized detection time. Responsive behaviour of the EM systems introduced a promising technique for sensing tasks in such systems. Self sensing is referred to as recruiting the existing solenoid coil of EM systems not only as an actuator, but also as a sensing medium through the mechanism of inductive sensing. This method helps reduce the complications of sensory equipment and analyses. Self sensing has been exploited in many applications as a sensing tool in (electro)magnetic systems [76, 77, 78]. This method observes for changes in the system based on induced voltages due to the dynamic behaviour of the system.

Some sophisticated forms of the self-sensing concept have been investigated for the sensor-less operation of the switched-reluctance motors (SRM) [79, 80] and magnetic bearing systems [81, 82, 83]. The main purpose of recruiting this advanced sensing method in the aforementioned applications is the exact estimation of the position of a metal target. In the current application, a fast detection of an undesired change in the system requires a responsive sensing method with high sensitivity. Since the main concern is the speed of the short-term behaviour of sensing during the initiation of any eminent change, sensitivity of self-sensing method offers a promising strategy for the detection task. Any change that alters the state of the system will produce an induced voltage across the EM coil. Hence, tracking this voltage gives insight into the current state of the system. Therefore, the technical approach used in this study utilizes the self-sensing capability of the EM system to reduce the corresponding delays and eliminate potential complications in sensory implementation [77].

A successful detection method is one that detects the change as soon as possible and avoids wrong detections originated from noise signal disturbances. Fast detection of the changes in the system, thus, may not be a trivial task of tracking the induced voltage and comparing the sensing signal with a threshold value. Response time of the simple threshold-check method may be modified by reducing the threshold value. However, due to the detrimental effects of noise signals on the sensing voltage, small threshold values may result in high false-alarm rates. Therefore, the stochastic properties of the sensing signals needs to be taken into consideration in the detection mechanism.

The first change detection problems arose from on-line statistical quality control, e.g., [84]. Since then, stochastic detection algorithms have been studied in various applications such as speech recognition and signal segmentation [85, 86], vibration monitoring [87], seismic signal processing [88], and biomedical signal processing [89]. The main objective of using such algorithms is to ponder how the mean and standard deviation values of signals are changing during a process where

consideration of the effects of the noise signals is indispensable [90].

The statistical change detection algorithms optimizes the change detection process, from $\theta_0$ to $\theta_1$, under two distributions, $p_{\theta_0}$ and $p_{\theta_1}$. One such algorithm scrutinizes the dynamic behaviour of the logarithm of the likelihood ratio (or simply, sufficient statistic), $s(y) = ln\frac{p_{\theta_1}(y)}{p_{\theta_0}(y)}$, and minimizes the detection time and false-alarms rate through an optimization problem [90]. Depending on the problem, the complexity and performance of the methods need to be adjusted. In problems with predetermined initial and final values of the change, the algorithm evaluates the signal based on whether the mean value is closer to the initial value or to the final value. A decision function is defined as a function of sufficient statistic which determines such comparison over the course of detection. The change in the sensing signal manifests as a large increase in the value of a decision function which is, then, compared with a predefined threshold value. In fact, the detection algorithm converts the existing uncertainties of the stochastic problem into a more deterministic problem that can be checked with a simple threshold check.

Elementary on-line change detection algorithms were designed using intuitive perspective of a change in a signal. Most of such algorithms work on data sets with a fixed size. More advanced methods deal with a sliding window which eliminates the requirement of a fixed size of data.

Basic detection methods are concerned with finding the change time from a known initial value $\theta_0$ to a known final value $\theta_1$ . Shewhart, geometric moving average, and finite moving average control charts are examples of such algorithms [91, 92, 93]. They define a detection function based on sufficient statistics to compare if the last observation is closer to the final value or the initial value. The value of the detection function is updated after each observation (data point). An eminent increase in that value indicates the occurrence of a change.

Cumulative summation (CUSUM) algorithm was first introduced in [94]. In its simplest derivation, it is a comparison between the cumulative summation of sufficient statistics- from the beginning of the observations until the current

observation- and an adaptive threshold. This algorithm records the entire information contained in the past observations. Therefore, it requires a progressive need of memory.

Bayesian approach was also introduced for change detection in [95] and was derived theoretically for optimality of detection in [96]. Classical Bayesian idea detects changes when *a posteriori* probability of a change exceeds a predefined threshold. It requires *a priori* information about the distribution of the change time. This method defines the detection function as a function of current observation, and, initial and final values of the signals. Bayesian method assumes the availability of *a priori* distribution of the change time and initial probability which makes this algorithms less practical for implementation [90].

When the final value of the signal after change is not known, two possible resolutions exist. The first one applies weightings on the likelihood ratio with respect to all possible values for the final value. In the second solution, the maximum likelihood estimate of the final value is used as the final value [97]. The weighted CUSUM algorithm is an example of the first strategy which is a direct extension of the CUSUM stopping time [98]. Definition of the detection function in weighted-CUSUM method does not allow a recursive calculation for detection function. Also, it evaluates all the observations from the beginning of process which needs an increasing memory requirement during the course of detection. Therefore, it may not be practical for on-line detection.

Generalized likelihood ratio (GLR) follows the second resolution for unknown final value and offers an optimal algorithm for this case. This method is also known as maximum likelihood method [99]. Detection function in this method is defined as a double optimization problem of the cumulative summation of the sufficient statistics [90]. The value of the detection function increases due to additive changes in the signal. GLR algorithm provides a means for the detection of changes where the final value of the signal after change is not known; however, it can also be recruited if such information is available.

Since the previous observations become less and less important as process advances, to reduce the memory requirements of the algorithm, a sliding window can be defined that traces over the last N data samples and ignores all the signals outside the window. The size of the sliding window should be selected carefully as a small size ignores too many data samples and a large size increases the computational cost. In general, finding an optimal window size is not a trivial task [100].

#### 1.2.2.2 Functional Activation

After an attempt against the stand-by state of the system is detected by the detection mechanism, a robust activation mechanism is needed to recover a safe state of the system. A potential activation mechanism compensates for the inductive properties of the solenoid coil. The magnetic force produced by the EM system should be increased very fast as, otherwise, the distance from the steady-state conditions deteriorates the recovery process.

Possible activation mechanisms can be divided into two distinctive categories: direct and indirect mechanisms. The direct methods ramp-up the current by controlling the supply voltage whereas indirect methods exploit a modified design in order to reduce the time constant of the system. The simplest method to increase the current and, correspondingly, the magnetic force is the application of a high supply voltage. This direct method makes use of the fact that the gradient of the current through an inductive element has proportional relation with the voltage supply. High activation supply can be provided by either a dedicated supply voltage or by an integrated circuit which boosts the nominal supply voltage to a predetermined value. Charge pumps and DC-DC converters can be used for such purposes [101, 102, 103]. Current boosters and power amplifiers are efficient alternatives which use a combination of transistors for ramping up the current [104]. These circuits, in essence, switch the supply voltage from a low voltage to a high value or regulate it during the control process. Inductive behaviour of the load is not always considered in the design procedure of such circuits. Thus, they do not

provide a satisfactory increase in the current flowing through an inductive load. Because some families of EM systems, e.g., EM locks, possess high values of inductance, such characteristics of the system cannot be ignored. Therefore, aside from the high-voltage activation, in this thesis, two other types of activation circuits are introduced which provide a modified design to increase the current very fast. These methods of activation are concerned more with designing a supply electronic circuit which modifies the time constant of the system.

1. Appending a capacitor to the system reduces the inductance by introducing a positive phase in the phase digram of the circuit. Capacitor-based circuits which are introduced in this thesis perform based on reducing the time constant of the circuit by decreasing its inductive properties.

2. Inductors inhibit any abrupt change in the current. The induced voltage over the coil due to the varying magnetic field opposes any change in the current. Since the time derivative of the current is proportional to the voltage across the inductor, a high voltage, e.g., spark voltage, will be needed to ramp up the current very fast. Generating one such voltage is neither practical nor safe. However, if another inductor comparable to the existing coil is available, instead of inducing a high voltage, a current can be imposed to the coil by connecting the two inductors with different currents to each other. This is the basis of inductor-based activation circuits.

#### 1.2.2.3 Eddy Currents

Non-laminated conductors introduce the generation of eddy (or Foucault [105]) currents which are a main source of energy loss in systems with varying magnetic fields. Two of the main energy losses involved in non-laminated conductors are ohmic losses due to current loops inside the conductor, and magnetic field reduction due to counter fields produced by the eddy currents opposing the originally applied fields. Such characteristics have been utilized for heat generation in induction heating systems [106, 107]. Due to the sensitivity of the self-sensing technique to

system's dynamics, energy dissipation corresponding to eddy currents introduces adverse consequences on realization of this method. The amplitude of the induced voltage experiences a reduction which relates to the dissipated energy inside the conductor material impeding the detection process.

The formulation of eddy-current generation and its effects on the magnetic field are investigated by different authors in systems with sinusoidal magnetic fields [108, 109, 110, 111, 112]. In such systems, the time-varying current/voltage source produces a changing magnetic field inside the conducting piece which, in turn, results in the generation of eddy currents. The eddy currents reduce the peak value of the magnetic field and, consequently, the ultimate strength of the system. Most of the eddy-current models consider either an AC supply and solve for steady-state solution [108], or assume small perturbations in the system that yields linearised equations [113]. Both cases, simplify the diffusion equation (governing magnetic field inside conducting material) and its general solution to compute the magnetic field distribution. Cauer Circuit modelling also is used for AC magnetic fields to eliminate the dependency on the frequency (e.g., [114]). This method divides the conductor's cross-sectional area into a number of sections with homogeneous eddy currents in each section. The total flux produced by the eddy currents can be calculated by lumping the effect of each section. This method is also recruited for steady-state calculations of eddy currents in systems with AC supplies.

The analysis of the EM systems with a DC supply does not require any eddy-current consideration in the steady-state conditions as the magnetic field is not changing with respect to time. However, the transient response of the system introduces a complex problem that needs to be solved in EM and structural mechanics environments, simultaneously. Furthermore, due to the potential of large deviations, linearisation of the model produces large inaccuracies and hence is not pragmatic. Therefore, a more sophisticated solution method is required to analyse the dynamics of the coupled modelling of structural mechanics and EM fields.

The basic problem of electromagnetism on a macroscopic level is solving very

well-known Maxwell's equations subject to appropriate boundary conditions. Due to the complex nonlinear dynamics of the system during its transient period, numerical methods offer a practical means to solve the governing equations. To see the complete dynamics of the measurement voltage, a modelling environment is needed which can encompass the rigid body dynamics, the magnetic fields, as well as its interaction with the electric component from which the field is being created.

Finite element method (FEM) has been used as a promising method for EM simulation and modelling. In earlier studies, e.g., [115], the simulation of inductive sensing through FEM has been tried with some simplifications and special modelling techniques to account for the interaction between the magnetic field and electric effect. Advancement of FEM modelling software introduced the opportunity to combine different simulation environments together and solve for their interactions. COMSOL Multiphysics modelling platform is one of the newest FEM modelling tools that efficiently simulates interconnected environments and computes the correlations among them. This software can be used to evaluate the self-sensing capability of the EM systems and to assess detrimental effects of eddy-current generation. In this thesis, we solve for eddy current effects using FEM modelling in COMSOL Multiphysics.

## 1.3 Thesis Overview

### 1.3.1 Part I: Biologically-inspired Motion Control for Kinematic Redundancy Resolution

The first part of this thesis investigates the Bernsteîn's degree of freedom problem. This part is constituted by three chapters as follows.

**Chapter 2** considers transposed Jacobian control law for motion control of redundant robot manipulators and derives sufficient conditions for exponential convergence to the target point in reaching motions. A modification for robust rectilinear trajectory of robot end-effector is also presented in this chapter.

**Chapter 3** introduces a synergy between body limbs which are related to the motion directly (actively) and those which may not seem to contribute to the motion (i.e. they contribute passively). In this chapter, the dynamics of an under-actuated robot manipulator is investigated. All the un-actuated joints are representing unattended degrees of freedom of human body. This chapter proposes that neglecting redundant degrees of freedom is an efficient method that human brain exploits for controlling body limb motions.

**Chapter 4** proposes a minimally-attended controller which controls redundant robot manipulators through a real-time optimization problem which optimizes attention to the control process. This method is presented here as a representative of control laws adopted by human brain for different motions including and not limited to the hand-arm motion.

### 1.3.2 Part II: Self-sensing Exploitation for Energy Conservation in Electromagnetic Devices

The second part of this thesis introduces the application of an advanced sensing mechanism for energy conservation purposes in a family of EM devices. This part is organized in two chapters as follows.

**Chapter 5** provides the system overview and modelling and derives the governing equations of the system. It also synthesises detrimental effects of eddy-current

generation on self-sensing capability of the system. Furthermore, a new variable, namely, *Eddy-displacement* is introduced which provides a novel representation of the effects of the eddy currents inside the conductor material. This chapter discusses the recruited detection algorithm and different activation mechanisms. The simulation results of each algorithm are also presented in this chapter.

**Chapter 6** investigates the application of the proposed control strategy on a family of EM systems as a case study. EM locking mechanisms produced in Rutherford Controls Int'l are used for experiments. The results of computer simulations and experiments are presented approving successful performance of cost-efficient intelligent EM locks.

# Part I

# Biologically-inspired Motion Control for Kinematic Redundancy Resolution

# Chapter 2

# Jacobian Transpose Controller: Stability and Modification

In this chapter, the performance of Jacobian transpose control law for human-like motion of redundant robot manipulators is investigated. Jacobian transpose controller was first introduced for the control of non-redundant robot manipulators [43]. In a task-space regulation problem, the structure of Jacobian transpose controller resembles a PD controller which regulates the position of the end-effector to a desired position in the task-space of the robot. This controller is defined as

$$u = -C\dot{q} - J^T K \Delta x \tag{2.1}$$

where $u$ is the vector of joint torques, $C$ is the matrix of damping shaping, $J$ is the manipulator Jacobian, $K$ is a positive scalar, and $\Delta x = x - x_d$ is the distance from the end-effector to the target point. The second term on the right hand side of this equation is the mapping from an artificial spring-like force, $F = -K\Delta x$, to joint torques. The artificial spring connects the end-effector of the robot to the target point. Figure 2.1 shows the artificial spring and its connection to the end-effector.

For systems where the gravitational force affects the motion and appears in the dynamic equations of the system, (2.1) can be augmented by a third term to compensate for the gravitational force, as follows.

$$u = -C\dot{q} - J^T K \Delta x + g(q) \tag{2.2}$$

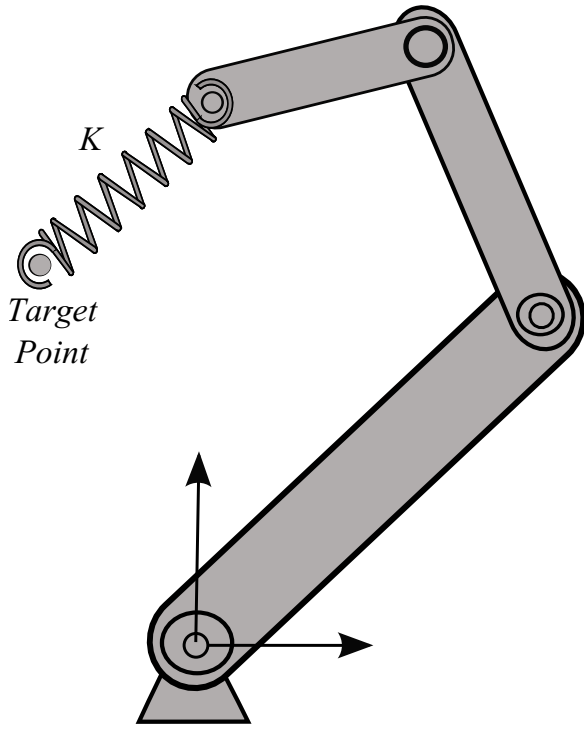


Fig. 2.1: Redundant robot manipulator and the virtual spring in the task space

As it was discussed in [22, 51, 116], by selecting a proper set of coefficients for the controller, stability of the target point can be guaranteed. All the analysis in these studies was done numerically and for a specific set of parameters. This novel idea in controlling redundant robot manipulators, as declared by the authors, challenges the Bernsteîn's degree of freedom problem.

All the proofs in the above referenced papers were presented using numerical analysis for a specific system with specified parameter values. This chapter provides the stability analysis of the system on a manifold and the transferability to a sub-manifold in a parametric way. This approach can be applied to the analysis of more general robot manipulators resembling human arm movements in three dimensions. Here a comprehensive analysis is presented that derives sufficient conditions for global convergence in a task-space regulation problem. The analysis is based on the concepts of *stability on a manifold* and *transferability to a sub-manifold* [22, 41].

## 2.1 Background and Useful Definitions

The general dynamic equation of a robot manipulator can be written as

$$H(q)\ddot{q}(t) + \{\frac{1}{2}\dot{H}(q) + S(q,\dot{q})\}\dot{q} + g(q) = u \tag{2.3}$$

where $q(t) \in \mathbb{R}^n$ is the vector of joint angles, $H(q(t))$ is the $n \times n$ inertia matrix, which is a positive definite symmetric matrix, $S(q(t),\dot{q}(t))\dot{q}(t) \in \mathbb{R}^n$ is the vector of Gyroscopic forces, that is constituted by Coriolis and Centrifugal forces, $g(q(t)) \in \mathbb{R}^n$ is the gravitational force vector, and $u \in \mathbb{R}^n$ is the control input vector to be exerted through joint actuators.

Substituting (2.2) into (2.3), we can express the closed-loop dynamics as following

$$H(q)\ddot{q} + \{\frac{1}{2}\dot{H}(q) + S(q,\dot{q}) + C\}\dot{q} + J^T(q)K\Delta x = 0. \tag{2.4}$$

Defining the total energy of the system such that it comprises the kinetic energy of the system and the potential energy stored in the artificial spring, we have

$$E = \frac{1}{2}\dot{q}^T H(q)\dot{q} + \frac{1}{2}K||\Delta x||^2. \tag{2.5}$$

Let us consider the r-dimensional manifold (UCM [117] or equilibrium-point manifold [118]) in which the end-effector is steadily located at the target point.

$$M^r = \{(q,\dot{q}) : E(q,\dot{q}) = 0\} \tag{2.6}$$

where $r$ is the number of redundant degrees of freedom, i.e. $r = n - m$ where $n$ is the number of joints (elemental variables) and $m$ is the number of task space coordinates (performance variables).

A neighbourhood of the equilibrium point can be defined as

$$N^{2n}(\delta, r_0) = \{(q,\dot{q}) :\ E(q,\dot{q}) \leq \delta^2 \ and\ ||q - q^0||_k \leq r_0\} \tag{2.7}$$

where $\delta > 0$ and $r_0 > 0$ are some positive parameters, $q^0$ is vector of joint angles for which the end-effector is located on the target point, and $||q - q^0||_k \equiv \{\frac{1}{2}(q - q^0)^T H(q)(q - q^0)\}^{\frac{1}{2}}$ is called k-norm of $(q - q^0)$, in this thesis.

The main stability concepts to be studied in this chapter are defined as follows.

**Definition 2.1.1.** Stability on a Manifold [22]

*If for an arbitrary given $\varepsilon > 0$, there exist a constant $\delta > 0$ depending on $\varepsilon$, and another constant $r_1 > 0$ independent of $\varepsilon$ and less than $r_0$, such that a solution trajectory of the closed-loop dynamics of the system starting from any initial state inside $N^{2n}(\delta(\varepsilon), r_1)$ remains in $N^{2n}(\epsilon, r_0)$, then the reference equilibrium state $(q^0, 0)$ is called stable on a manifold.*

**Definition 2.1.2.** Transferability to a Sub-manifold [22]

*If for a reference equilibrium state there exist constants $\varepsilon_1 > 0$ and $r_1 > 0$ $(r_1 < r_0)$ such that any solution of the closed-loop dynamics of the system starting from an arbitrary initial state in $N^{2n}(\varepsilon_1, r_1)$ remains in $N^{2n}(\varepsilon_1, r_0)$ and converges asymptotically as $t \to \infty$ to some point on $M_r \cap N^{2n}(\varepsilon_1, r_0)$, then the neighbourhood $N^{2n}(\varepsilon_1, r_1)$ of the reference equilibrium state is said to be transferable to a sub-manifold of $M_r$.*

The definition of stability as presented here resembles the Lyapunov theory of stability. The energy function vanishes inside the manifold $M^r$ and is positive outside of it. Transferability to a sub-manifold also is similar to the LaSalle's theorem of asymptotic convergence to an invariant set where $\dot{E} = 0$. However, the energy function as defined here is not an explicit positive definite function of the joint angles. Therefore, the definition of the neighbourhood of a point is given using a constraint on the energy function and a specific distance of the system configuration $q$ to a manifold $M^r$.

Now, we propose the following theorem.

**Theorem 2.1.3.** *The reference state $(q^0, 0)$ is stable on a manifold for the closed-loop dynamics of (2.2) under the following conditions*

*1.*

$$Kh(\Delta x, \dot{q}(t)) + f(K; \Delta x, \dot{q}(t)) \geq 0 \tag{2.8}$$

*2.*

$$bI_m \leq 2I_m - KJC^{-1}HC^{-1}J^T \leq aI_m \tag{2.9}$$

where

$$h(\Delta x, \dot{q}) = \Delta x^T J C^{-1}(-\frac{1}{2}\dot{H} - S)\dot{q} - \Delta x^T \dot{J} C^{-1} H \dot{q} - \dot{q}^T J^T J C^{-1} H \dot{q}, \tag{2.10}$$

$$\begin{aligned} f(K; \Delta x, \dot{q}) = \dot{q}^T (C - \frac{\gamma}{2} H - \frac{\gamma K}{4} H)\dot{q} \\ + K \Delta x^T (K J C^{-1} J^T - \gamma I_m - \gamma J C^{-1} H C^{-1} J^T)\Delta x, \end{aligned} \tag{2.11}$$

and $\gamma$, $a$, and $b$ are positive scalars.

*Proof.* See Appendix A. □

Considering (A.12), this proof also shows that the neighbourhood $N^{2n}(\delta, r_1)$ is transferable to a sub-manifold of $M_r$ which is $M_r \bigcap N^{2n}(\varepsilon, r_0)$. Therefore, the following theorem holds

**Theorem 2.1.4.** *If conditions in theorem* (2.1.3) *hold, the neighbourhood* $N^{2n}(\delta, r_1)$ *is transferable to a sub-manifold of* $M_r$.

The analysis provided in Appendix B shows that the value of $\gamma$, as a milestone for the speed of convergence, can be effective on the value of the left hand side of (2.8). Hence, a satisfactory value for $\gamma$ can be found to justify (2.8) for a reasonable set of control parameters. For a known value of $K$, matrix $C$ can also be designed to satisfy (2.9).

### 2.1.1 Jacobian Transpose and Singularity Avoidance

The practicality of the Jacobian transpose method for regulation problems was proved in the previous section. This controller renders the target points exponentially stable. However, it ignores any other desired characteristic of the movement. The only controller parameters which influence on the motion are the stiffness and damping coefficients, $K$ and $C$. Jacobian transpose controller may be proposed as a brain-like control law if it can satisfy other criteria of a human-like motion. For example, human arm does not meet singular configurations during reaching tasks. Therefore, singularity avoidance can be considered for evaluation of a potential

controller. In this section, the closed-loop dynamics of a redundant robot manipulator is analysed to confirm whether the damping matrix $C$ can be designed for singularity avoidance purposes.

First, we assume that the initial configuration of the system is not singular. Hence, one sufficient condition for singularity avoidance is to avoid the magnitude of the change in each joint angles (except the first joint) to be less than the magnitude of the initial joint angles, as considered in [22]. Through this approach the joint angles are bounded in both directions. Here, the system's dynamics is analysed for avoiding changes in joint angles that are less than the negative of initial values of each joint variables, i.e.

$$q_i(t) - q_i(0) \geq -q_i(0) \Rightarrow q_i(t) \geq 0. \tag{2.12}$$

We consider the integrated closed-loop dynamics of the system which gives

$$\begin{aligned} C(q(t) - q(0)) &= -H(q(t))\dot{q}(t) + H(q(0))\dot{q}(0) + \int_0^t (\frac{1}{2}\dot{H} - S)\dot{q}d\tau - K\int_0^t J^T \Delta x d\tau \\ &\geq -Cq(0). \end{aligned} \tag{2.13}$$

In this equation, $\vec{a} \geq \vec{b}$ means that each element of vector $\vec{a}$ is greater than or equal to the corresponding element in vector $\vec{b}$.

Boundedness of matrix $H$ justifies that there exist positive scalars $a$ and $b$ such that

$$-H(t)\dot{q}(t) \geq -a\dot{q}(t), \tag{2.14}$$

and

$$H(0)\dot{q}(0) \geq b\dot{q}(0). \tag{2.15}$$

Furthermore, we can find a constant matrix $A$ such that

$$A\dot{q} \leq (\frac{1}{2}\dot{H} - S)\dot{q} \tag{2.16}$$

that gives

$$\int_0^t A\dot{q}d\tau \leq \int_0^t (\frac{1}{2}\dot{H} - S)\dot{q}d\tau. \tag{2.17}$$

Hence, we have

$$\int_0^t \frac{1}{2}(\dot{H} - S)\dot{q}d\tau \geq A(q(t) - q(0)). \tag{2.18}$$

Furthermore, exponential convergence to the target point indicates that there exist positive parameters $\xi_1, \xi_2, \ldots, \xi_m$ such that

$$\begin{aligned} ||\Delta x_1|| &\leq \xi_1 ||\Delta x_1(0)|| e^{-\frac{\gamma t}{2}} \\ ||\Delta x_2|| &\leq \xi_2 ||\Delta x_2(0)|| e^{-\frac{\gamma t}{2}} \\ &\cdot \\ &\cdot \\ &\cdot \\ ||\Delta x_m|| &\leq \xi_m ||\Delta x_m(0)|| e^{-\frac{\gamma t}{2}} \end{aligned} \tag{2.19}$$

where $\Delta x_i$ is the $i^{th}$ task-space coordinate for $i = 1, 2, \ldots, m$. Defining $\xi = max\{\xi_1, \xi_2, \ldots, \xi_m\}$ gives

$$\begin{bmatrix} ||\Delta x_1|| \\ ||\Delta x_2|| \\ \cdot \\ \cdot \\ \cdot \\ ||\Delta x_m|| \end{bmatrix} \leq \xi \begin{bmatrix} ||\Delta x_1(0)|| \\ ||\Delta x_2(0)|| \\ \cdot \\ \cdot \\ \cdot \\ ||\Delta x_m(0)|| \end{bmatrix} e^{-\frac{\gamma t}{2}} \Rightarrow ||\Delta X(t)||^\dagger \leq \xi ||\Delta X(0)||^\dagger e^{-\frac{\gamma t}{2}} \tag{2.20}$$

where

$$||\Delta X(t)||^\dagger = \begin{bmatrix} ||\Delta x_1(t)|| \\ ||\Delta x_2(t)|| \\ \cdot \\ \cdot \\ \cdot \\ ||\Delta x_m(t)|| \end{bmatrix}. \tag{2.21}$$

Afterwards, we define matrix $\hat{J}$ as the Jacobian matrix with all $sin(q_i(t))$ and $cos(q_i(t))$ functions substituted by their maximum value, i.e. 1. That is

$$\hat{J} = \{J |\ sin(\theta) \equiv 1,\ cos(\theta) \equiv 1,\ for\ all\ \theta\}. \tag{2.22}$$

Now, we can write

$$\int_0^t J\Delta x d\tau \leq \hat{J}\xi\frac{2}{\gamma}(1-e^{-\frac{\gamma t}{2}})||\Delta X(0)||. \tag{2.23}$$

Hence,

$$-K\int_0^t J\Delta x d\tau \geq -\frac{2K\xi}{\gamma}\hat{J}||\Delta X(0)||. \tag{2.24}$$

Therefore, (2.13) becomes

$$C(q(t)-q(0)) \geq -a\dot{q}(t)+b\dot{q}(0)+A(q(t)-q(0))-\frac{2K\xi}{\gamma}\hat{J}||\Delta X(0)|| \tag{2.25}$$

Moreover, we know that, based on the geometric constraints of the system, we have

$$||\Delta x_j(0)|| \leq 2\sum_{i=1}^{n} l_i, \ \ for\ j=1,2,\ldots,m \tag{2.26}$$

where $l_i$ is the length of the $i^{th}$ link of the manipulator. Also, if we assume that the robot is at rest at $t=0$, defining $\omega = q(t)-q(0)$, we can write

$$a\dot{\omega}+(C-A)\omega \geq -\frac{4K\xi}{\gamma}\hat{J}I^m\sum_{i=1}^{n} l_i \tag{2.27}$$

where $I^m$ is an $m\times 1$ matrix with all components equal to 1. Equation (2.27) gives the differential equation governing the link angles when the initial angular velocities for all links are zero. This ODE can be solved for C under the condition on $\omega$ to be greater or equal to the negative of the initial link angles, for all future time. In other words, the solution of this equation has to stay in the following manifold

$$M_n = \{\omega | \omega \geq -q(0)\} \tag{2.28}$$

Also, considering (2.13), we can satisfy that the solution lies on the manifold (2.28), if

$$-(C-A)q(0) \leq -p\dot{q}(t)-\frac{4K\xi}{\gamma}\hat{J}I^m\sum_{i=1}^{n} l_i \tag{2.29}$$

for still initial conditions. We suppose that the angular velocity of each joint actuator has a saturation value, i.e.

$$-\dot{Q} \leq \dot{q}_i(t) \leq \dot{Q}, \ \ for\ i=1,2,...,n. \tag{2.30}$$

So, (2.29) can be simplified to

$$a\dot{Q} - \frac{4K\xi}{\gamma}\hat{J}I^m \sum_{i=1}^{n} l_i \geq -(C-A)q(0). \tag{2.31}$$

The left-hand-side of (2.31) is a constant vector. Denoting it by $L$, we can write

$$L \geq -(C-A)q(0). \tag{2.32}$$

Thus, the condition on each damping factor for singularity avoidance can be found as following.

$$c_i \geq A_i - \frac{L_i}{q_i(0)},\ for\ i = 2, 3, ..., n. \tag{2.33}$$

As can be seen in (2.33), damping factors are related to the initial link angles. That is, as the initial joint angles approach singular points, higher damping factors are required for singularity avoidance. It can be concluded that a universal set of damping coefficients for avoiding singularities in the system cannot be found without imposing limitations on the position of the target point with respect to the initial configuration of the robot.

The limitations in damping factors are found for all joints except the first one that can have any damping factor satisfying stability conditions of equations (2.8) and (2.9). Thus for singularity avoidance, all the equations of stability ((2.8), (2.9)) must be satisfied along with (2.33).

## 2.2 Jacobian Transpose Method with Multiple Performance Elements

In this section, a modified Jacobian transpose controller is introduced whose structure can be adjusted based on different task-space performance requirements. The modification on the control law is introduced by proposing a new objective function whose derivatives are to be appended to the controller as an optimization term. The generalized form of the potential objective function can be considered as

$$U = \frac{1}{2}(\sum_{i=1}^{s} w_i \Delta x^i)^T K (\sum_{i=1}^{s} w_i \Delta x^i) \tag{2.34}$$

where $s$ is the number of artificial springs corresponding to each task-space variable ($\Delta x_i$), $w_i$ is the weighting factor corresponding to the $i^{th}$ spring, $\Delta x_i$ is the elongation in the $i^{th}$ spring which is the appended task-space variable, and $K$ is the stiffness matrix which can be a scalar or a diagonal matrix of the form $K = diag(k_1, k_2, k_3, ..., k_i, ..., k_s)$ where $k_i$ is the corresponding stiffness of the $i^{th}$ spring. Furthermore, the following equation holds for the weighting factors

$$\sum_{i=1}^{s} w_i = 1. \tag{2.35}$$

The controller corresponding to this potential function is

$$u = -C\dot{q} - J^T K(\sum_{1}^{s} w_i \Delta x^i) \tag{2.36}$$

where the second term is the optimization vector in regard with the energy function of (2.34).

#### 2.2.0.1 Imposing Human-like trajectories

To impose a rectilinear end-effector trajectory, the controller should have two performance elements in the task space: an element that show the distance to the target point, $\Delta x^1 = x - x_d$ and a surplus element that corresponds to the distance from a straight line connecting initial and target points $\Delta x^2$ (see Appendix C). In this case, $s = 2$ and we have

$$u = -C\dot{q} - J^T K(w_1 \Delta x^1 + w_2 \Delta x^2). \tag{2.37}$$

In this controller, besides recruiting an artificial spring that connects the end-effector to the final point in the task space, system is augmented with another spring that draws the end-effector towards the hypothetical straight line (see figure 2.2).

The weighting factors $w_1$ and $w_2$ can be adjusted to justify the straightness of the end-effector's trajectory. To be compared with the results of the Jacobian transpose method, the values of stiffness and $w_1$ can be set such that the stiffness coefficient corresponding to $\Delta x_1$, i.e. $kw_1$, is equal to that in the simple Jacobian

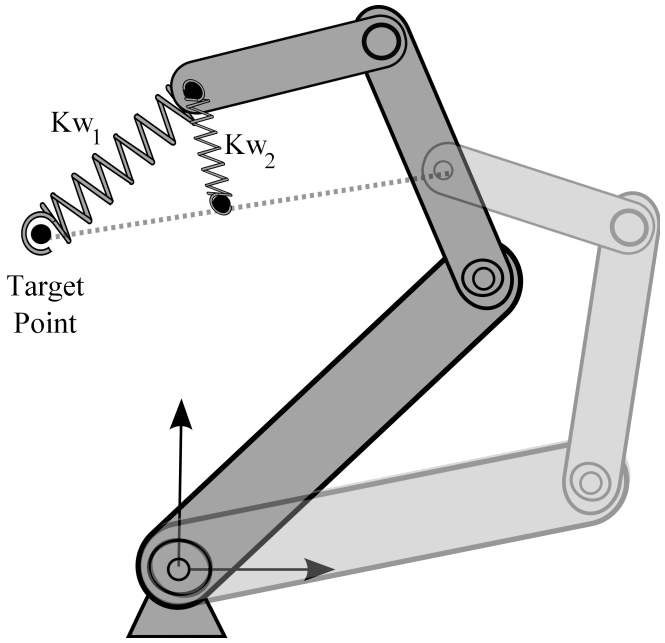


Fig. 2.2: Redundant manipulator with two artificial springs attached to the end-effector

transpose method. Stability on the manifold and transferability to a sub-manifold can be approved by considering the energy function of (2.38) and following the same procedure conducted for the simple task-space PD controller.

$$E = \frac{1}{2}\dot{q}^T H(q)\dot{q} + U \tag{2.38}$$

where $U$ is introduced in (2.34).

## 2.3 Simulation Results and Discussions

In this section, we investigate the behaviour of the system by applying the modified Jacobian transpose method proposed in the previous section. The case study is a four-link robot manipulator whose end-effector is confined to move in a two-dimensional horizontal plane. The initial position and two target points $P_1$ and $P_2$ are chosen as in table 2.1.

Convergence to the target point can be justified by choosing a reasonable set of damping factors and stiffness coefficient. Here we consider two sets of damping coefficients, as in table 2.2, to inspect the variability of the system and the effects

Table 2.1: Initial posture of the system and selected target points.

| Parameter | Value |
|---|---|
| $q_{1_0}$ | $80°$ |
| $q_{2_0}$ | $40°$ |
| $q_{3_0}$ | $50°$ |
| $q_{4_0}$ | $70°$ |
| $P_1$ | $(0, 0.1)\ m$ |
| $P_2$ | $(-0.5, 0.2)\ m$ |

of employing the novel control design.

Table 2.2: Damping coefficients for simulations.

| Parameter | Set one | Set two |
|---|---|---|
| $c_1$ | 1.2 | 1.0 |
| $c_2$ | 0.5 | 0.9 |
| $c_3$ | 0.1 | 0.8 |
| $c_4$ | 0.1 | 0.7 |

Each set is accompanied with different values of weighting factors to examine the effect of weighting factors on the trajectory of the end-effector. The stiffness coefficient is adjusted with the weighting factors for the control law to always give the same value for the proportional coefficient of the simple Jacobian transpose method ($kw_1 = 10$). The following relation between weighting factors holds.

$$w_1 + w_2 = 1 \tag{2.39}$$

Mechanical parameters of the system are listed in table 2.3. Figure 2.3 shows the trajectory of the end-effector towards the first target point $P_1 = (0, 0.1)$ and the task-space velocity of the end-effector for different combination of weighting factors for the first set of damping factors in Table 2.2. The blue graph in this figure corresponds to a simple Jacobian transpose controller. This figure demonstrates

the improvement in the trajectory of the end-effector by increasing the weighting factor of the appended performance variable. The velocity profile remains almost the same for different weighting factors. It increases fast in the beginning and with a semi-bell-shaped profile converges to zero.

Table 2.3: Parameter values of the simulated robot manipulator.

| Parameter | Value |
|---|---|
| $m_1$ | 1.75 $kg$ |
| $m_2$ | 1.25 $kg$ |
| $m_3$ | 0.30 $kg$ |
| $m_4$ | 0.05 $kg$ |
| $I_1$ | 0.01 $kg.m^2$ |
| $I_2$ | 0.01 $kg.m^2$ |
| $I_3$ | 0.0002 $kg.m^2$ |
| $I_4$ | 0.00002 $kg.m^2$ |
| $l_1$ | 0.3 $m$ |
| $l_2$ | 0.31 $m$ |
| $l_3$ | 0.1 $m$ |
| $l_4$ | 0.1 $m$ |

Plots in figure 2.4 show the trajectories and velocity profiles of the end-effector towards the first target point for second set of damping coefficients. This figure shows that the deviation of the trajectories from the straight line can also be reduced by adjusting the damping coefficients. However, as the velocity profiles show, the convergence to the target point takes longer. For reaching tasks to target points close to the initial position of the end-effector, the velocity profiles are expected to converge to zero in around $1s$ [35]. That is, the performance of the simple Jacobian transpose controller is not fast enough when the rectilinear trajectories are achieved.

Figure 2.5 shows the trajectories of the end-effector towards the second target

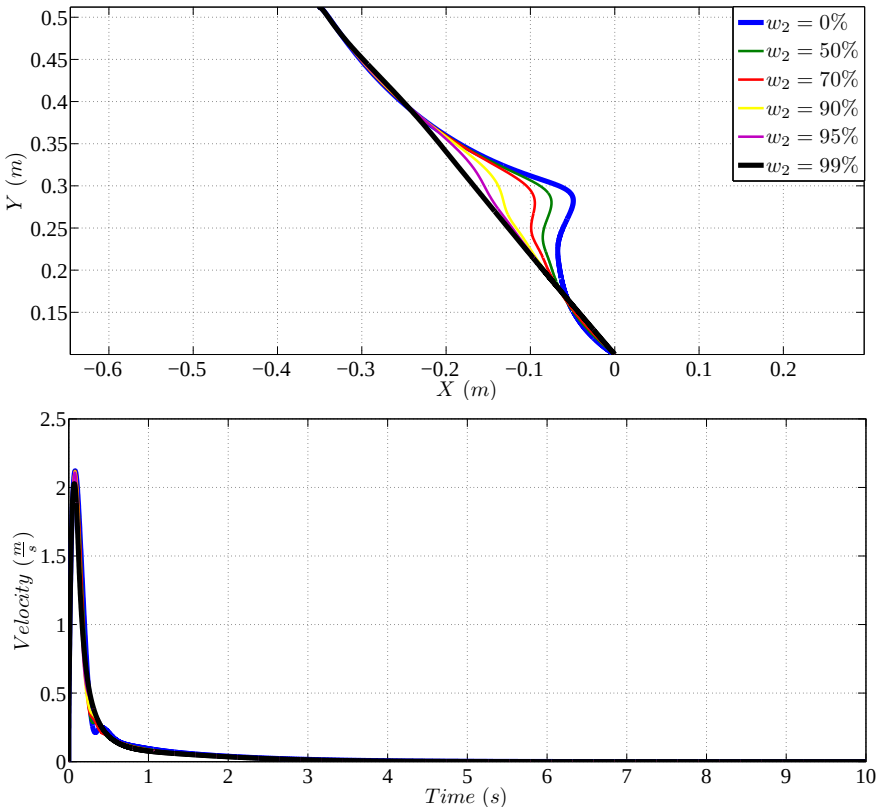


Fig. 2.3: End-effector trajectories towards $P_1$ and velocity profiles for the first set of damping coefficients

point $P_2 = (-0.5, 0.2)$ and the corresponding velocity profiles for the first set of damping coefficients. This figure shows more than one local maximum point in the velocity profiles. Such profiles have been detected for human-like motions in the experiments [35]. The end-effector passes the target point and returns to it which results in intermediate points with zero velocity in the velocity profile.

Figure 2.6 also plots the trajectories of the end-effector towards the second target point and corresponding velocity profiles for the second set of damping coefficients.

Figure 2.7 plots the convergence of the first joint angles for different weighting factors for the two sets of damping coefficients. This picture illustrates the effect of damping coefficients on the variability of the system. Both plots correspond to motion of the robot towards the first target point. The weighting factors change

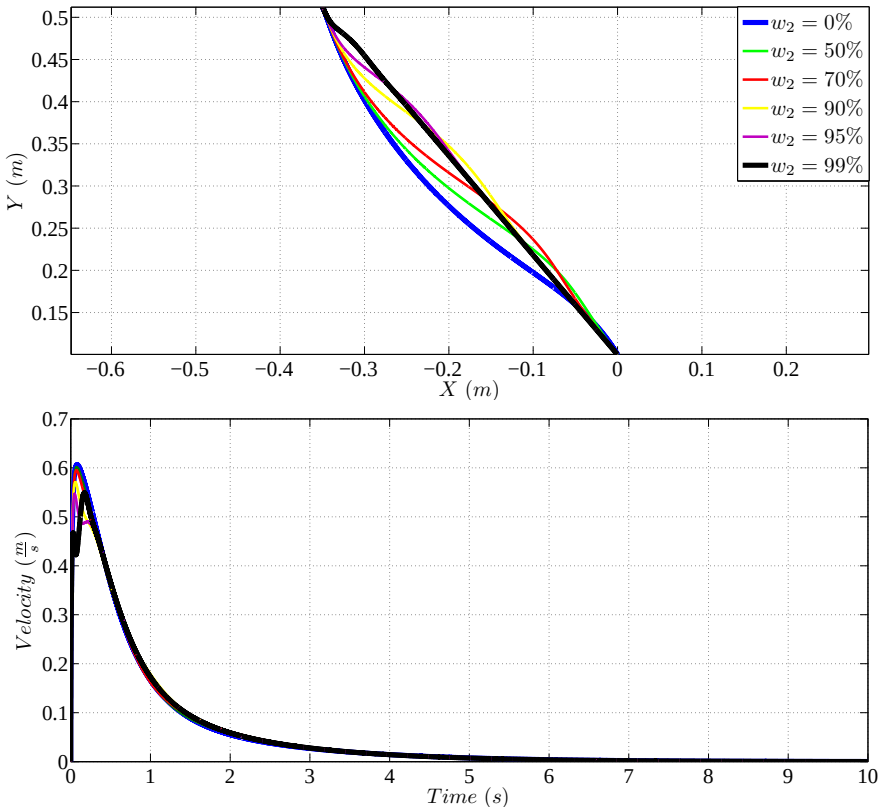


Fig. 2.4: End-effector trajectories towards $P_1$ and velocity profiles for the second set of damping coefficients

the final value of the joint angle but the convergence retains its general profile for different weighting factors. On the other hand, although the final value of the joint angles differ from one set of damping coefficients to another, the change in the profiles is more noticeable in these plots. Figure 2.8 also demonstrates the variability in joint angles for the two set of damping coefficients for the reaching to the second target point when $w_2 = 95\%$

## 2.4 Conclusion

In this chapter, general performance of the Jacobian transpose method was discussed and its exponential convergence was proved based on the definitions of stability on a manifold and transferability to a sub-manifold. A modified potential function was also introduced to enhance linearity of the end-effector trajectories in reaching tasks. The modified controller recruited a set of appended task-space

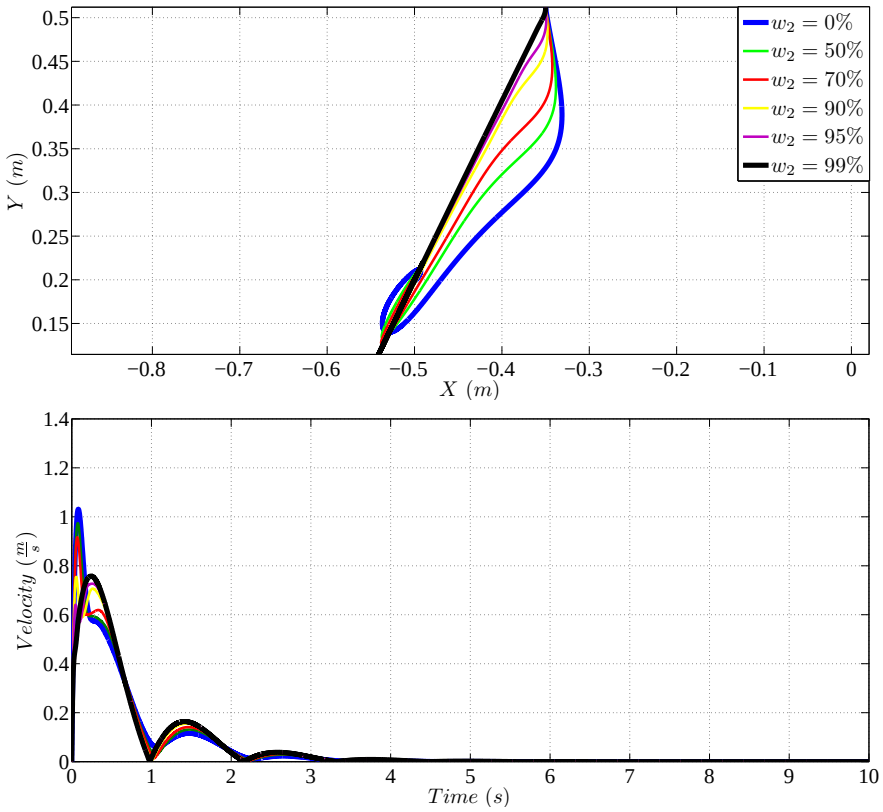


Fig. 2.5: End-effector trajectories towards $P_2$ and velocity profiles for the first set of damping coefficients

variables for introducing extra performance criteria. To account for a human-like motion, the rectilinear trajectory of the end-effector was considered as the criterion by taking into account the distance of the end-effector to the hypothetical straight line (see Appendix C.)

Modified Jacobian controller could satisfy part of the human-like motion characteristics, i.e. rectilinear trajectory, without heavy computations. However, a detailed view of the velocity profiles as shown in figure 2.9 shows that the end-effector velocity profile does not resemble the expected bell-shaped profile. So, the controller design does not cover all aspects of a brain-like control strategy.

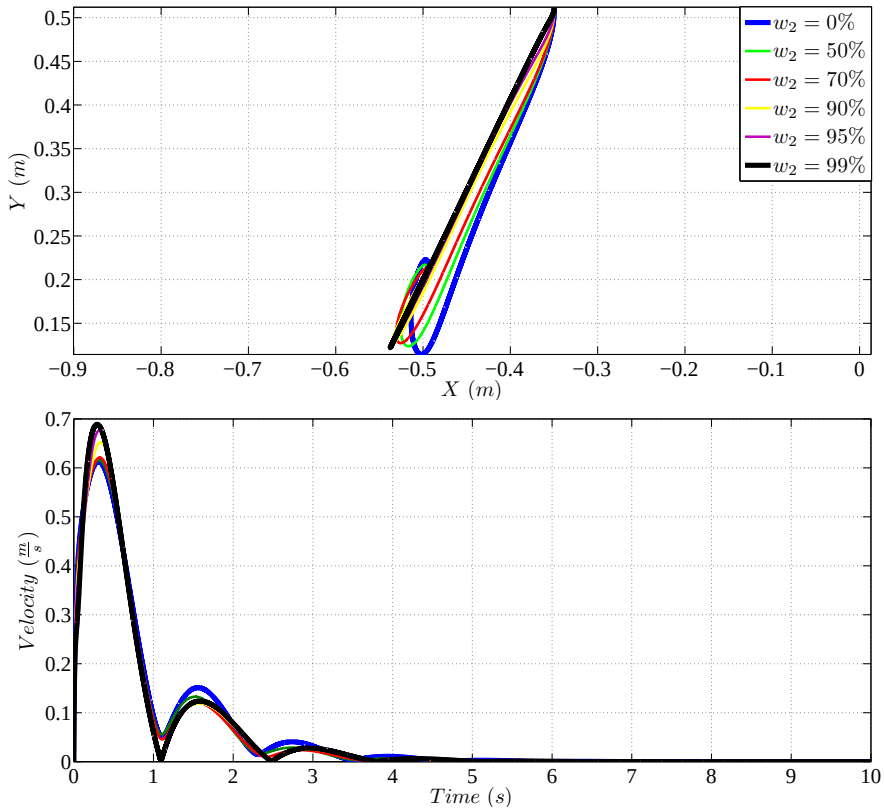


Fig. 2.6: End-effector trajectories towards $P_2$ and velocity profiles for the second set of damping coefficients

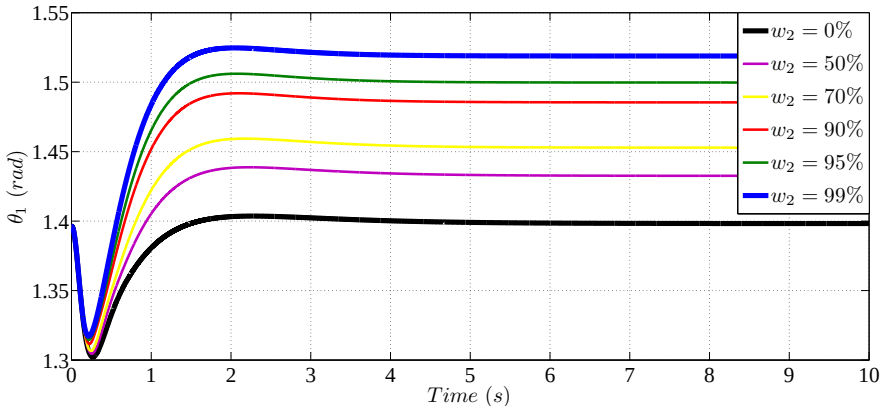


(a) First set of damping coefficients

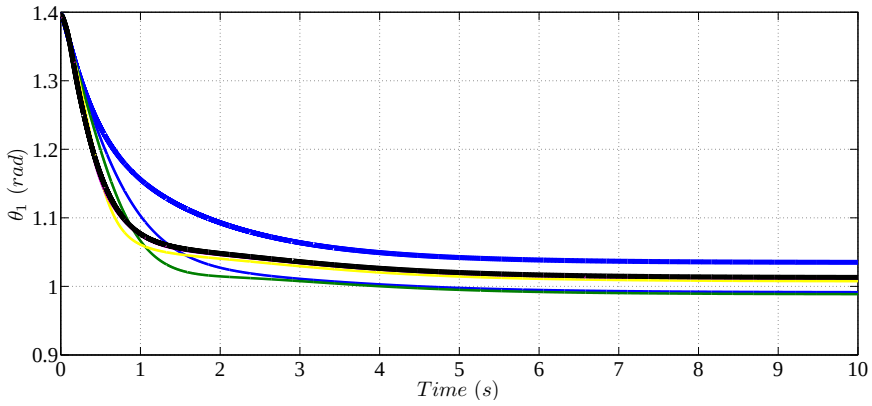


(b) Second set of damping coefficients

Fig. 2.7: Joint angles for different set of damping coefficients

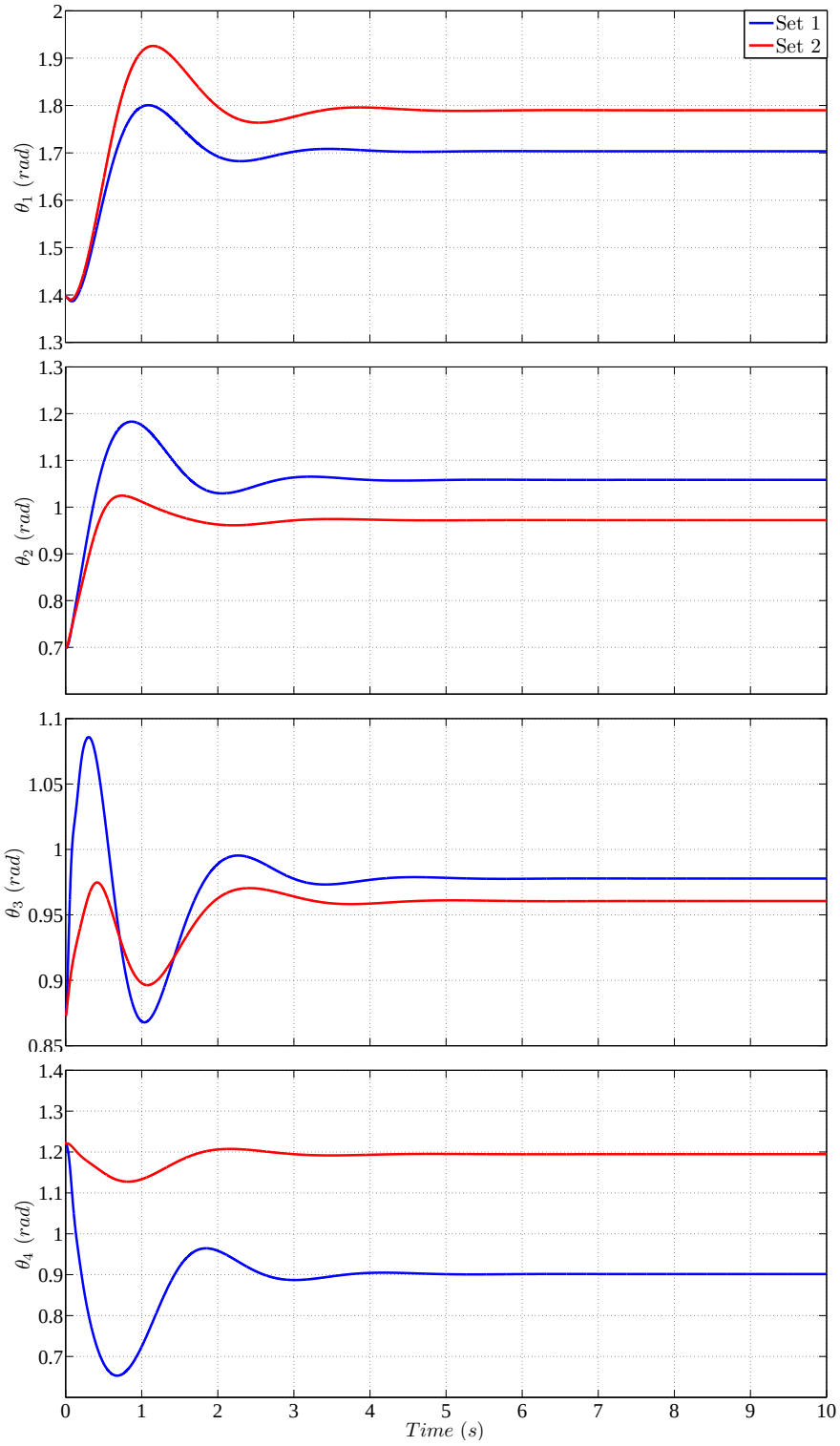


Fig. 2.8: Variability in joint angles for reaching towards $P_2$

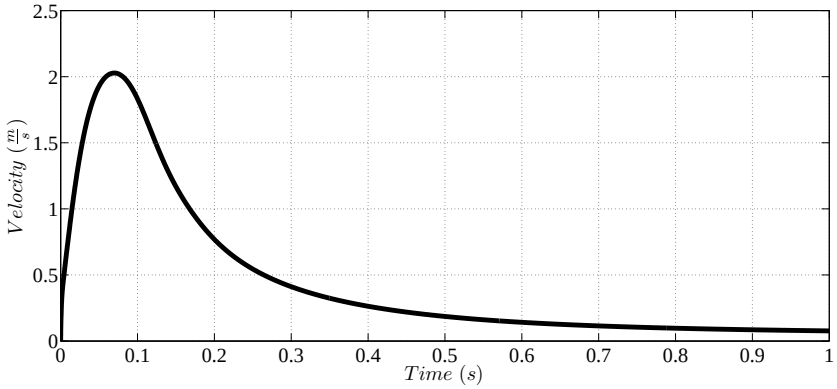


Fig. 2.9: Detailed view of the velocity profile for the motion towards $P_1$ with $w_2 = 99\%$

# Chapter 3

# Abridged Jacobian for Robot Control

In this chapter, a modified version of the Jacobian transpose controller is proposed. This controller limits the attention to control only to specific elements of the system. This method is intended as an improvement on the previous methods in robot control by controlling an abridged dynamics of the system in task-space regulation problems.

Jacobian transpose control law was introduced for the motion control of both redundant and non-redundant robot manipulators as a controller with much less computation compared to model-based controllers [119, 120, 116]. Because of simplicity of this controller and low level of computation, many researches considered modification of this controller by either adding performance indices or defining an effective Jacobian matrix to keep the simplicity of control along with satisfying more criteria. In [121] authors added a learning term to the controller to append a learning capability to the controller. Collision Jacobian matrix is also designed for object avoidance [122]. A recent study investigated the application of Jacobian transpose controller for under-actuated manipulators [123]. In this study, the Jacobian matrix is partitioned into two parts which determine the passive and active joints of the system. The Partition corresponding to the active part is called effective Jacobian and is used in the control law.

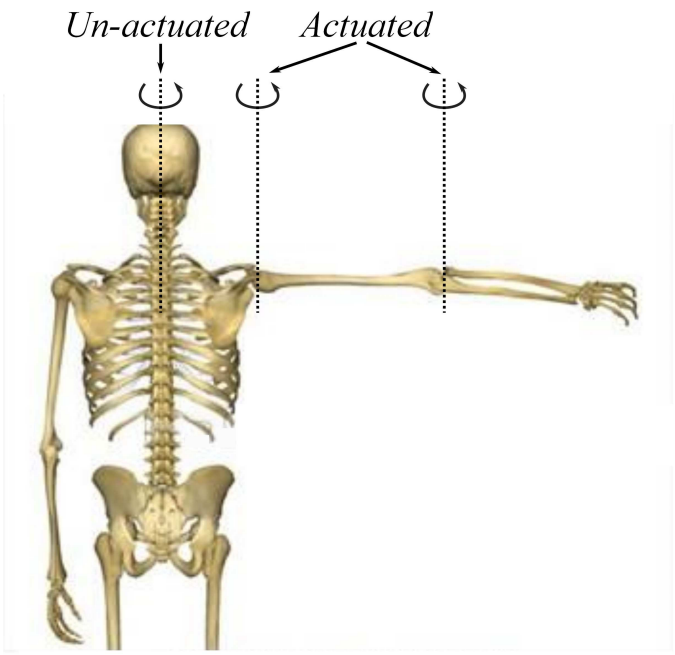


Fig. 3.1: Motion of human torso as an un-actuated variable

In the study of biological motions, the investigations have been limited to the motion of the limb, excluding the effects of other body limb motions. For example, in human hand-arm movement, the motion of human torso is neglected. However, during such motions, changes in the position of the human torso are eminent. Nonetheless, human brain does not seem to consider controlling the motion of such parts. Therefore, the problem of controlling hand-arm motions can be translated into the problem of controlling an under-actuated system. The un-actuated joints in human body during hand-arm motions are all DOFs involved in the motion of human torso, e.g., hip and spine rotation, as depicted in figure 3.1.

The hypothesis of existence of passive/un-actuated joints during biological motions aligns with the hypothesis of ignoring surplus DOFs of the system. This hypothesis reduces attention to the motion by decreasing the complexity of control process as it ignores some part of the system dynamics. Furthermore, removing actuation from the first joints reduces the energy consumption of the system, significantly. So, both attention and energy consumption are reduced in an under-

actuated system. Passive joints may include the motions originated from torso, and even shoulder. This proposes that some DOFs of the human arm are neglected during the task. The control process, however, may increase/decrease the number of DOFs which are attended in different phases of control. In other words, passive joints may experience control signals at some periods during the motion. This type of control introduces a hybrid controller which adopts different structures during the task.

Under-actuation in robot manipulators is usually analysed with free-rotating passive joints with no external (generalized) forces applied to the joint. This results in the conservation of momentum in the system if the passive joints constitute the first joints of the system connected to the base and all forces are applied internally to the joints. One simple example of such system is rotating stool example [124]. Due to the frictionless joint of the system, the total angular momentum of the system remains constant. Now, if a person sitting on the stool tries to spin a rotating wheel in his hands, due to the change in the angular momentum of the wheel about the joint, a reaction torque is created which rotates the stool. Hence, although the angular momentum of the system may remain the same, internal changes in the configuration of the system is still possible. Falling cat phenomenon [125], motion of snake-boards [126], and springboard divers [127] are other under-actuated systems which experience various configurations while retaining a conserved angular momentum.

In this chapter, the redundant manipulator is analysed as an under-actuated system with a series of un-actuated variables. The passive joints of the system are assumed to have a friction force applied to the joints. Recent studies investigated an interesting phenomenon for such family of under-actuated systems where the friction force is assumed to be linear in the joint velocity, e.g., viscous damping force and the un-actuated joints are cyclic [124, 128]. Here the motions of the human torso and hip which contribute to the planar motion of the hand are modelled as un-actuated variables with friction forces. The viscous-like friction forces are

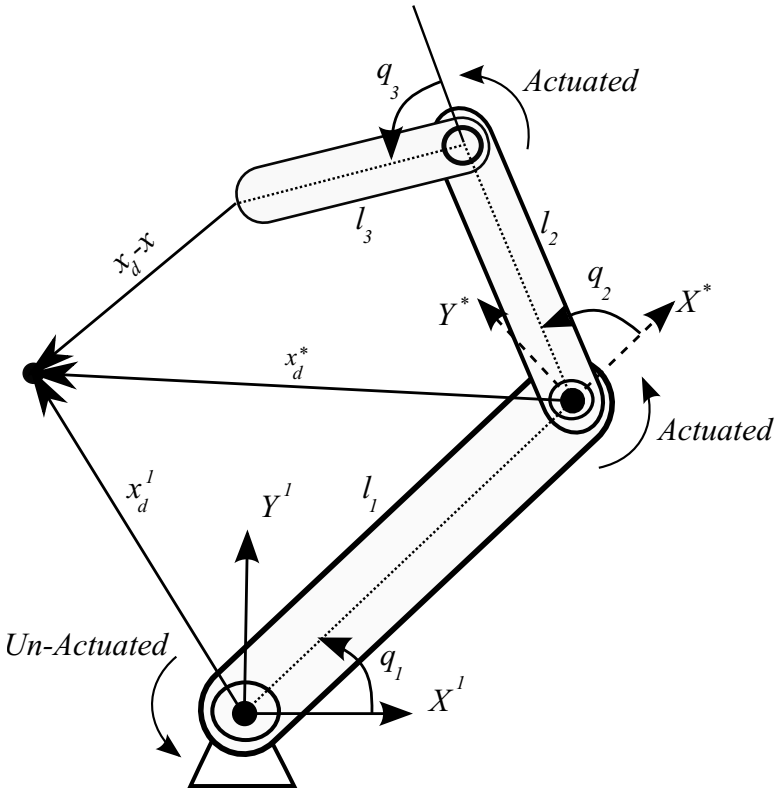


Fig. 3.2: An under-actuated robot manipulator

briefly analysed and other type of forces are also discussed, shortly.

## 3.1 Task-space Regulation Problem for Under-actuated Robot Manipulators

In this section, asymptotic stability of the simple Jacobian transpose method is investigated for under-actuated robot manipulators. Instead of the conventional definition of the Jacobian matrix, an abridged Jacobian matrix is defined which considers only the active joints and relates joint-space and task-space velocities of the active side of the system.

Consider a robot manipulator where the first $n$ joints are un-actuated while the remaining $m$ joints are actuated. We define a new coordinate system whose origin is on the first active joint (i.e. $n^{th}$ joint) and its $x$ direction is along the $n^{th}$ link. Figure 3.2 shows an under-actuated manipulator and demonstrates the passive and active joints and useful denotations.

The relative position of the end-effector with respect to this auxiliary coordinate system can be derived as follows.

$$x^* = \begin{bmatrix} \sum_{i=n+1}^{n+m} l_i c_{n+1:i} \\ \sum_{i=n+1}^{n+m} l_i s_{n+1:i} \end{bmatrix} \tag{3.1}$$

where $x^*$ is the coordinate of the end-effector in the auxiliary coordinate system, $l_i$ is the length of the $i^{th}$ link, and, $c_{n+1:i}$ and $s_{n+1:i}$ refer to $cos(q^{n+1} + q^{n+2} + ... + q^i)$ and $sin(q^{n+1} + q^{n+2} + ... + q^i)$, respectively.

The abridged Jacobian matrix is defined as

$$J^*_{ij} = \frac{\partial x^*_i}{\partial q^*_j} \tag{3.2}$$

where $J^*_{ij}$ is the component of this Jacobian matrix at the $i^{th}$ row and the $j^{th}$ column, and $q^*$ refers to actuated joint variables. This Jacobian matrix is called active-Jacobian matrix, here. We can also write:

$$\dot{x^*} = J^* \dot{q^*} = \begin{bmatrix} \underline{0} & J^* \end{bmatrix} \dot{q} = J^\dagger \dot{q} \tag{3.3}$$

where $\dot{q^*}$ is the time derivative of the active joint variables, $\underline{0}$ is the $p \times n$ matrix of zero elements, where $p$ is the number of task-space DOFs, and $\dot{q}$ is the time derivative of all joint variables. In this study, $J^\dagger$ is called passivity-reduced Jacobian matrix.

The relative position of the target point to the end-effector in the base coordinate system (placed on the first joint) is given by:

$$\Delta x^1 = \begin{bmatrix} \sum_{i=1}^{n+m} l_i c_{1:i} \\ \sum_{i=1}^{n+m} l_i s_{1:i} \end{bmatrix} - x^1_d \tag{3.4}$$

where $\Delta x^1$ is the vector from the target point to the end-effector, and $x^1_d$ is the coordinate of the target point in the base coordinate system. In this study, $(.)^1$ presents vectors in the base coordinate system and $(.)^*$ presents them in the auxiliary coordinate system. Accordingly, we can write:

$$\Delta x^* = R_{-q_{1:n}} \Delta x^1 \tag{3.5}$$

where $q_{1:n} = \sum_{i=1}^{n} q_i$, and $R_{-q_{1:n}} = \begin{bmatrix} c_{1:n} & s_{1:n} \\ -s_{1:n} & c_{1:n} \end{bmatrix}$.

The position of the target point with respect to the auxiliary coordinate system is

$$x_d^* = R_{-q_{1:n}}(x_d^1 - \begin{bmatrix} \sum_{i=1}^{n} l_i c_{1:i} \\ \sum_{i=1}^{n} l_i s_{1:i} \end{bmatrix}) \tag{3.6}$$

where the second term inside brackets is the position of the first active joint in the base coordinate system.

The dynamic equation of the system can be presented as follows.

$$H\ddot{q} + (\frac{1}{2}\dot{H} + S)\dot{q} + g(q) = v \tag{3.7}$$

with $v$ as the vector of the input torques designed as following.

$$v = g(q) + u = g(q) - \begin{bmatrix} \bar{0} \\ kJ^{*T}\Delta x^* \end{bmatrix} - C\dot{q} = g(q) - kJ^{\dagger T}\Delta x^* - C\dot{q} \tag{3.8}$$

where $\bar{0}$ is the zero vector corresponding to the un-actuated joints' inputs, $k$ is a positive constant, $C$ is a constant diagonal matrix of the appropriate dimensions whose first $n$ elements represent the damping coefficients of the un-actuated joints, and $(.)^T$ denotes transposition. Equation (3.8) presents the active-Jacobian transpose controller which ignores the un-actuated joints and limits the control of the system exclusively to controlling the active joints. The target point for this controller is moving based on (3.6). Therefore, for the new coordinate system, the regulation problem is transferred into tracking a moving object. The stability of this controller is investigated in the following theorem.

**Theorem 3.1.1** (Stability of the Active-Jacobian Transpose Controller)**.** *Active-Jacobian transpose controller as defined in* (3.8) *renders the task-space target points asymptotically stable.*

*Proof.* The closed-loop dynamics of the system can be written as

$$H\ddot{q} + (\frac{1}{2}\dot{H} + S)\dot{q} + kJ^{\dagger T}\Delta x^* + C\dot{q} = 0 \tag{3.9}$$

Defining the energy function as the mechanical energy of the system as follows:

$$E = \frac{1}{2}\dot{q}^T H\dot{q} + \frac{1}{2}k||\Delta x^*||^2 \geq 0, \tag{3.10}$$

with the first term as the kinetic energy and the second term as the virtual potential energy of the system, we have:

$$\frac{d}{dt}E = \dot{q}^T H\ddot{q} + \frac{1}{2}\dot{q}^T\dot{H}\dot{q} + k\dot{x^*}^T\Delta x^* \tag{3.11}$$

Factorizing $\dot{q}^T$, we get:

$$\frac{d}{dt}E = \dot{q}^T(H\ddot{q} + \frac{1}{2}\dot{H}\dot{q} + kJ^{\dagger T}\Delta x^*). \tag{3.12}$$

Considering (3.9) and (3.12), we can write:

$$\frac{d}{dt}E = -\dot{q}^T(S + C)\dot{q} = -\dot{q}^T(C)\dot{q} \leq 0 \tag{3.13}$$

Therefore, $\dot{q}$ and $\Delta x^*$ converge to zero as $t \to \infty$.

Also, if only the first joint is un-actuated, the Lagrange equation corresponding to this un-actuated cyclic variable is

$$\frac{d}{dt}(H_{1l}\dot{q}^l) = -C_{1l}\dot{q}^l. \tag{3.14}$$

Integrating (3.14) for constant diagonal matrix $C$ gives

$$H_{1l}\dot{q}^l = -C_{11}\Delta q^1 \tag{3.15}$$

where $C_{11}$ is the first diagonal element of the $C$ matrix, and $\Delta q^1 = q^1(t) - q^1(0)$ is the change in the first un-actuated joint variable from its initial condition. As the left hand side of (3.15) converges to 0 as $t \to \infty$, we can conclude that, $\Delta q^1 \to 0$ as $t \to \infty$. Therefore, the un-actuated joint recovers its initial condition. Thus, $R_{-q_1} \to I_2$ and, (3.4) and (3.5) give $\Delta x^1 \to \Delta x^* \to 0$ as $t \to \infty$. This proves the

convergence to the target point in the task space with one degree of passivity in the joint space of the system.

If the damping coefficients in the un-actuated joints are not constant (or in general, the right hand side of (3.14) is not integrable with respect to time), (3.14) gives

$$H_{1l}\dot{q}^l = -\int_0^t C_{11}\dot{q}^1. \tag{3.16}$$

The left hand side of this equation converges to zero as $t \to \infty$; however, self-recovery phenomenon is not guaranteed. Therefore, the un-actuated cyclic variable may adopt a different final value depending on $C_{11}\dot{q}^1$ function. Furthermore, if $n > 1$, only the first joint variable is cyclic; and (3.14) does not hold for the rest of the un-actuated joints. However, because the physics of the problem indicates that $|\Delta x^1| = |\Delta x^*|$. Therefore, $\Delta x^1 \to 0$ as $t \to \infty$ if and only if $\Delta x^* \to 0$ as $t \to \infty$. Hence, $\Delta x^1 \to 0$ as long as $\Delta x^* \to 0$ and this proves the convergence to the task-space target point with several un-actuated joints.

□

## 3.2 Simulation Results and Discussions

For evaluating the performance of the active-Jacobian transpose controller for the case of human-like motions, arm is modelled as a two-link manipulator connected to a passive joint which represents human torso's rotation. The simulated manipulator is therefore a three-link redundant manipulator which moves in a horizontal plan. The system parameters are listed in Table 3.1. The controller parameters are as follows.

$$K = diag(7, 6),\ C_{2,2} = 0.9,\ C_{3,3} = 0.8$$

where $C_{2,2}$ and $C_{3,3}$ are the second and the third diagonal components of the damping matrix corresponding to the first and the second active joints, respectively.

The controller regulates the end-effector from the initial point $x_0 = (0.27, 0.61)$ (for $q = (30°, 40°, 50°)$) to the target point $x_d = (0, 0.46)$ (for $q = (30°, 70°, 80°)$).

The friction force in the un-actuated joint is assumed to be a viscous damping friction with damping coefficient $\mu = 1$, i.e. $C = diag(\mu, C_{2,2}, C_{3,3})$.

Table 3.1: Parameter values of the manipulator.

| Parameter | Value |
|---|---|
| $m_1$ | 1.75 $kg$ |
| $m_2$ | 1.25 $kg$ |
| $m_3$ | 0.30 $kg$ |
| $I_1$ | 0.01 $kg.m^2$ |
| $I_2$ | 0.01 $kg.m^2$ |
| $I_3$ | 0.0002 $kg.m^2$ |
| $l_1$ | 0.3 $m$ |
| $l_2$ | 0.31 $m$ |
| $l_3$ | 0.2 $m$ |

Figure 3.3 shows the trajectory of the end-effector produced by the active-Jacobian transpose controller. This figure shows that a rectilinear trajectory can be achieved even without a comprehensive consideration of the DOFs of the system. The velocity profile for this regulation is shown in figure 3.4. The end-effector velocity resembles the profile produced by the simple Jacobian transpose controller in terms of having large initial gradients.

Figure 3.5 compares the end-effector trajectories for active-Jacobian transpose controller and simple Jacobian transpose controller. The $K$ and $C$ matrices are selected the same for both controllers. This figure shows that not attending to controlling the first DOF of the system results in a more rectilinear trajectory. Also, figure 3.6 plots the corresponding end-effector velocity profiles. This figure shows similar initial gradients in the velocity profiles. It also shows that the active-Jacobian transpose controller avoids large velocity amplitudes which results in faster convergence to the target point.

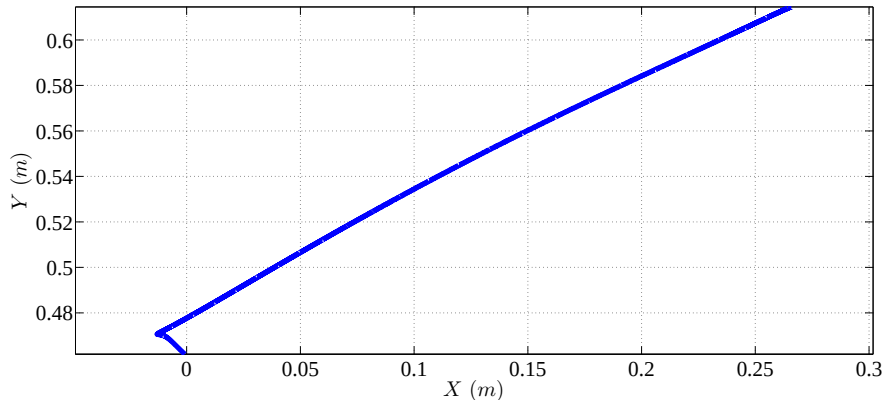


Fig. 3.3: End-effector trajectory for active-Jacobian transpose controller

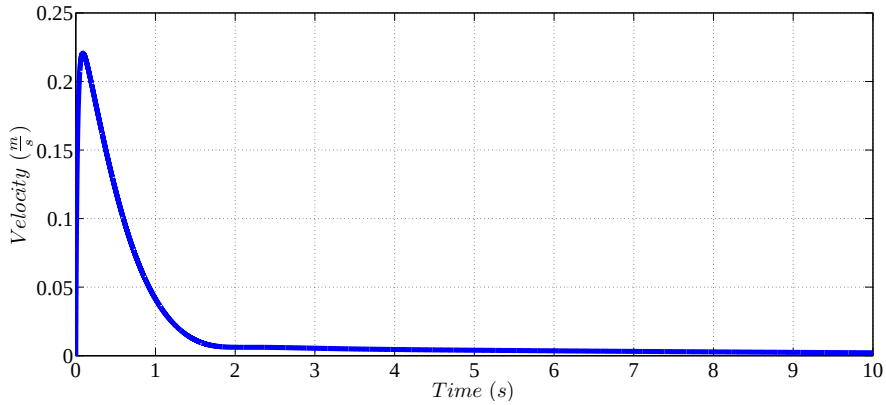


Fig. 3.4: End-effector velocity for active-Jacobian transpose controller

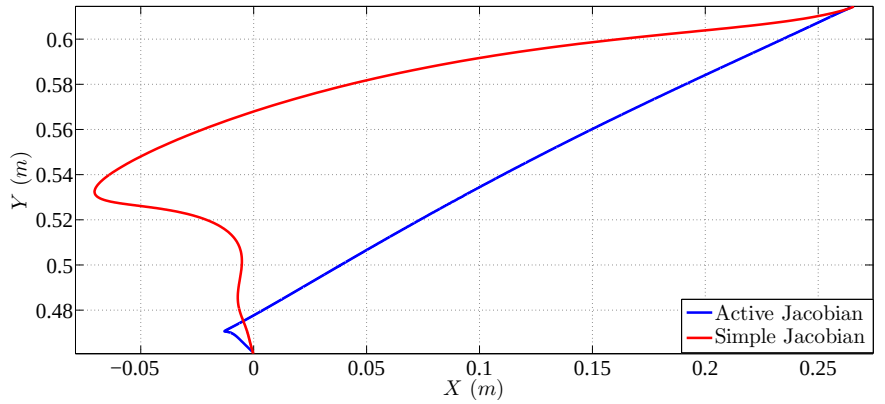


Fig. 3.5: Comparison between end-effector trajectories for active-Jacobian transpose and simple Jacobian controllers

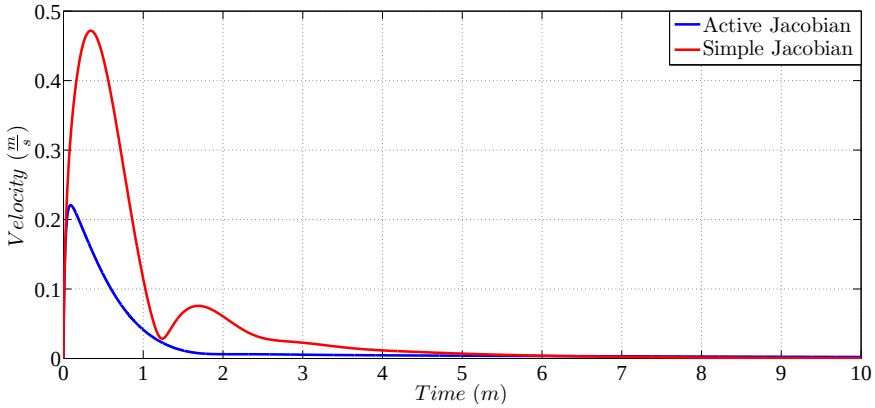


Fig. 3.6: Comparison between end-effector velocities for active-Jacobian transpose and simple Jacobian controllers

## 3.3 Conclusion

In this chapter, an abridged Jacobian matrix was introduced and stability of the task-space regulation problem for the active-Jacobian transpose controller was evaluated. Simulation results for reaching problems were also presented which approved the convergence to the target point. Rectilinear end-effector trajectory was observed under the application of this controller and the velocity profile resembled that of simple Jacobian transpose controller.

This controller introduces the opportunity to reduce the number of attended DOfs of the system during the control process; thereby, eliminating a portion of computations. The performance of this controller indicates that as long as reaching is concerned, the number of controlled DOFs of the system can be reduced to the number of the task-space DOFs. That is, the system can be treated as a non-redundant system without any alteration in achieving the requirement of the problem (reaching)).

# Chapter 4

# Minimally-attended Regulator

Jacobian Transpose controller was analysed in chapter 2 and its performance was compared with a modified version of the controller. It was seen that the modified controller can produce the expected end-effector rectilinear trajectory. Another kinematic characteristic of human hand-arm motions is a bell-shaped end-effector velocity profile [35]. Jacobian Transpose control considers the distance to the target point and adjusts the control signals only based on this parameter. Consequently, as the distance is maximum at the beginning of the motion, the control signals create large initial accelerations resulting in an abrupt increase in the end-effector velocity at the start of motion. On the other hand, the velocity profiles of a natural motion starts smoothly, increases to a maximum value, and then reduces smoothly tracing a symmetric bell-shaped profile. A controller that reduces attention to the distance to target point or the magnitude of control signals, can decrease the initial acceleration of the system and smooth the velocity profile.

Based on [55, 56], for a skilled operator, sensory functions contribute more to human control laws and brain activities than the attention to the motor control cortex inside the brain. Hence, the attention to control is minimized by human brain. Less attention to the control process agrees with previous hypothesis on the functionality of human brain. Examples include Bernsteîn's hypothesis on freezing DOFs of the human body during motion, the evolution of learning strategies which introduce a series of policies which are adopted and developed by brain and con-

verge to optimal values, and finally the Jacobian transpose method which ignores the complexities of the system.

The concept of minimum attention was first introduced in [57]. The minimum attention control aims to design a control input whose deviation from a constant control is minimized and thus, by reducing time and state feedback dependency of the control law, the controller does not require an intensive computation. This concept has been mostly applied in networked systems to reduce the computational costs or to compensate for the limited communications to the system [59, 129, 58]. The performance objective to be minimized in this controller is defined as

$$J = \int_0^\infty (\frac{\partial u^T}{\partial x}\frac{\partial u}{\partial x} + \frac{\partial u^T}{\partial t}\frac{\partial u}{\partial t}). \tag{4.1}$$

For a constant control signal, $J = 0$. In the current application, we consider only the derivative of the control signal with respect to time. So, the performance index is reduced to

$$J = \int_0^\infty (\frac{\partial u^T}{\partial t}\frac{\partial u}{\partial t}). \tag{4.2}$$

To contribute this minimization problem into a regulation problem, the performance index should be modified. Next section investigates a generalized performance index which includes minimum attention index as well as regulation indices through introduction of *minimally-attended regulator (MAR)*

## 4.1 Minimally-attended Regulator

A minimally-attended controller is designed through an optimization problem whose solution minimizes the required attention to the computation of the control signals. The first part of this section analyses this controller in the continuous-time domain and the second part provides corresponding formulations in the discrete-time domain.

### 4.1.1 Continuous-time Case

We define a minimally-attended regulator in continuous-time domain as follows.

**Definition 4.1.1.** *Infinite-horizon Continuous-time Minimally-Attended Regulator (ICMAR)*

*For the affine control system*

$$\dot{x} = f(x,t) + g(x,t)u, \tag{4.3}$$

*define the cost function*

$$J = \frac{1}{2}\int_0^\infty (\dot{u}^T R \dot{u} + x^T Q x)dt \tag{4.4}$$

*with $Q \geq 0$ and $R > 0$. Solution to the following optimization problem yields the controller that optimizes attention to the control.*

**Problem Statement 1** (ICMAR)**.**

$$\begin{aligned} \underset{\dot{u}}{\text{Minimize}} \quad & J = \frac{1}{2}\int_0^\infty (\dot{u}^T R \dot{u} + x^T Q x)dt \\ \text{subject to} \quad & \dot{x} = f(x,t) + g(x,t)u \end{aligned}$$

A more general form of the problem statement can be presented which contains the control signals, the states of the system, and the time derivative of them. The cost function for this problem is

$$J = \frac{1}{2}\int_0^\infty (u^T R_1 u + \dot{u}^T R_2 \dot{u} + x^T Q_1 x + \dot{x}^T Q_2 \dot{x})dt. \tag{4.5}$$

The corresponding optimization problem can be then reposed as

**Problem Statement 2** (ICMAR with General Cost Function)**.**

$$\begin{aligned} \underset{u,\dot{u}}{\text{Minimize}} \quad & J = \frac{1}{2}\int_0^\infty (u^T R_1 u + \dot{u}^T R_2 \dot{u} + x^T Q_1 x + \dot{x}^T Q_2 \dot{x})dt \\ \text{subject to} \quad & \dot{x} = f(x,t) + g(x,t)u. \end{aligned}$$

This problem can be reduced to a simple quadratic regulator by setting $R_2 = \underline{0}$ and $Q_2 = \underline{0}$, where $\underline{0}$ is the zero matrix of appropriate size. It represents ICMAR problem when $R_1 = \underline{0}$ and $Q_2 = \underline{0}$.

The cost function of the general ICMAR problem does not present the general structure of a standard quadratic regulator corresponding to (4.3). Hence, the problem representation needs to be reconstructed.

An augmented state variable can be defined as

$$z = \begin{bmatrix} x \\ \dot{x} \end{bmatrix}$$

which gives

$$\dot{z} = \begin{bmatrix} \dot{x} \\ \ddot{x} \end{bmatrix} = F(z,t) + G(z,t)v \tag{4.6}$$

where

$$F(z,t) = \begin{bmatrix} z_2 \\ \dot{f}(x,t) \end{bmatrix} = \begin{bmatrix} z_2 \\ \dot{f}(z,t) \end{bmatrix} \tag{4.7}$$

where $z_2$ refers to the second component of $z$, $\dot{x}$, and $G(z,t)$ depends on how the input vector $v$ is selected. If $v$ is selected such that

$$v = v_1 = \begin{bmatrix} u \\ \dot{u} \end{bmatrix}, \tag{4.8}$$

it gives

$$G(z,t) = \begin{bmatrix} \underline{0} & \underline{0} \\ \dot{g}(x,t) & g(x,t) \end{bmatrix} = \begin{bmatrix} \underline{0} & \underline{0} \\ \dot{g}(z,t) & g(z,t) \end{bmatrix} \tag{4.9}$$

and the cost function can be presented as

$$J = \frac{1}{2}\int_0^\infty (v_1^T R v_1 + z^T Q z)dt \tag{4.10}$$

where

$$R = \begin{bmatrix} R_1 & \underline{0} \\ \underline{0} & R_2 \end{bmatrix}$$

$$Q = \begin{bmatrix} Q_1 & \underline{0} \\ \underline{0} & Q_2 \end{bmatrix}.$$

This cost function holds the standard quadratic regulator design which can be solved with the constraint of (4.6). However, for the ICMAR problem, since

$R_1 = \underline{0}$, $det(R) = 0$. Therefore, the problem can not be dealt with by conventional algorithms. To reconfigure the system dynamics a new state variable and input vector can be defined as

$$z = \begin{bmatrix} x \\ \dot{x} \\ u \end{bmatrix} \tag{4.11}$$

$$v = v_2 = \dot{u}. \tag{4.12}$$

which introduces a new system representation as

$$\dot{z} = \begin{bmatrix} z_2 \\ \dot{f}(z,t) + \dot{g}(z,t)z_3 \\ \underline{0} \end{bmatrix} + \begin{bmatrix} \underline{0} \\ g(z,t) \\ I \end{bmatrix} v_2 \tag{4.13}$$

where $I$ is an identical matrix of appropriate size.

The new cost function for this system is as follows.

$$J = \frac{1}{2} \int_0^\infty (v_2^T R v_2 + z^T Q z) dt \tag{4.14}$$

where

$$R = R_2$$

$$Q = \begin{bmatrix} Q_1 & \underline{0} & \underline{0} \\ \underline{0} & Q_2 & \underline{0} \\ \underline{0} & \underline{0} & R_1 \end{bmatrix}$$

The ICMAR problem can, therefore, be restated for the new system with appended states as following.

**Problem Statement 3** (Well-posed ICMAR)**.**

$$\underset{\dot{u}}{\text{Minimize}} \qquad J = \frac{1}{2} \int_0^\infty (v_2^T R v_2 + z^T Q z) dt,$$

$$\text{subject to} \qquad \dot{z} = F(z,t) + G(z,t) v_2$$

*where*

$$F(z,t) = \begin{bmatrix} z_2 \\ \dot{f}(z,t) + \dot{g}(z,t)z_3 \\ \underline{0} \end{bmatrix}$$

$$G(z,t) = \begin{bmatrix} \underline{0} \\ g(z,t) \\ I \end{bmatrix}$$

This problem can be solved by conventional optimization methods such as Hamiltonian optimization or nonlinear quadratic regulator optimization methods [130, 131, 132, 133, 134]

Due to the structure of governing equations in mechanical systems, the complexity of ICMAR problem can be reduced. The Euler-Lagrange equation of a mechanical system can be written as

$$H(q)\ddot{q} + \{\frac{1}{2}\dot{H}(q) + S(q,\dot{q})\}\dot{q} + g(q) = \tau \tag{4.15}$$

where, $q = (q_1, ..., q_n)^T$ is the vector of system's states, $H(q)$ is the $n \times n$ inertia matrix, $S(q,\dot{q})$ is a skew-symmetric matrix, $g(q)$ corresponds for the gravity terms, and $\tau$ is the vector of generalized forces applied to the system. Defining $u = \tau + g(q)$, the state-space representation of this system becomes

$$\frac{d}{dt}\begin{bmatrix} q \\ \dot{q} \end{bmatrix} = \begin{bmatrix} \underline{0} & I \\ \underline{0} & -H^{-1}(q)C(q,\dot{q}) \end{bmatrix}\begin{bmatrix} q \\ \dot{q} \end{bmatrix} + \begin{bmatrix} \underline{0} \\ H^{-1}(q) \end{bmatrix} u \tag{4.16}$$

where $C = \frac{1}{2}\dot{H}(q) + S(q,\dot{q})$.

Defining the augmented state as

$$z = \begin{bmatrix} q \\ \dot{q} \\ \ddot{q} \end{bmatrix},$$

new equations for the appended state vector can be written as

$$\dot{z} = Az + B\dot{u} \tag{4.17}$$

with

$$A = \begin{bmatrix} \underline{0} & I & \underline{0} \\ \underline{0} & \underline{0} & I \\ \underline{0} & -H^{-1}(z)\dot{C}(z) & -H^{-1}(z)(\dot{H}(z) + C(z)) \end{bmatrix}$$

and

$$B = \begin{bmatrix} \underline{0} \\ \underline{0} \\ H^{-1}(z) \end{bmatrix}$$

If we define $v = \dot{u}$, the system representation of (4.17) can be used for IC-MAR optimization. Considering the system as a linear time-varying system, IC-MAR problem translates into an LQR problem which can be solved using standard methods.

All the cost functions introduced so far are quadratic with respect to the state variable. However, we can consider a more general form of cost function as

$$J = \frac{1}{2} \int_0^\infty (\dot{u}^T R \dot{u} + h(z)) dt \tag{4.18}$$

where $h(z)$ is any function of the state vector. An example of this is regulation to a point in the task space of robot manipulators. Considering a quadratic potential function in the task space of manipulators, we have

$$h(z) = h(x(z)) = (x(z) - x_d)^T K (x(z) - x_d) \tag{4.19}$$

where $x(z)$ is the position coordinates of the end-effector in the work space, $x_d$ is the target point in the work space, and $K$ is a positive definite matrix. $x(z)$ is a function of joint angles, $z_1$; and the translation from $h(x(z))$ to $h(z)$ is not linear. Therefore, it does not yield a quadratic cost function with respect to joint angles.

For solving this optimization problem, $h(z)$ can be linearised about an operating point to yield a quadratic function of joint angles. Hamiltonian optimization with Lagrange multipliers can also be recruited, in the nonlinear case, to solve for the optimizing control signals [132, 133].

Minimum-attention controller reduces the attention to control. Attention to control, however, is adaptive to the relative position of the system with respect to the desired position. It is low in the beginning and it increases near the target point. Hence, in lieu of minimizing the attention, an adaptive function should adjust the amount of attention during the control of the system.

The attention to control can be set by adjusting the weighting matrices $R$ and $Q$ with respect to each other during the task. The attention should increase as the robot approaches its final configuration to enhance the accuracy of the reaching task. $R$ can be designed as an adaptive function of time and distance to the final configuration. As matrix $R$ is a milestone of how much attention is reduced, increasing attention can be accomplished by reducing the weighting of $R$ with respect to $Q$. A set of potential adaptive functions can be designed as follows.

$$R = \ e^{-\alpha t}\ e_m^{\beta diag(q-q_d)} R^*$$

$$Q = e^{\alpha t} Q^*$$

where $\alpha$ and $\beta$ are positive scalars, $e_m$ is the matrix exponential, and $R^*$ and $Q^*$ are constant weighting matrices.

### 4.1.2 Discrete-time Case

For computer implementation minimally-attended regulator needs to be presented in the discrete-time domain. Minimally-attended regulator in the discrete time domain is defined as following.

**Definition 4.1.2.** *Infinite-horizon Discrete-time Minimally-attended Regulator (ID-MAR)*

*For the dynamic system defined as*

$$x_{k+1} = f_k(x_k) + g_k(x_k)u_k \tag{4.20}$$

*define the cost function as*

$$J = \frac{1}{2}\sum_{j=1}^{\infty}((u_j - u_{j-1})^T R_j (u_j - u_{j-1}) + x_j^T Q_j x_j) \tag{4.21}$$

*with $Q_j \geq 0$ and $R_j > 0$. Solution to the following optimization problem yields the controller that optimizes the attention to the control process.*

**Problem Statement 4** (IDMAR)**.**

$$\begin{aligned} \underset{u_j}{\text{Minimize}} \quad & J = \frac{1}{2}\sum_{j=1}^{\infty}((u_j - u_{j-1})^T R_j (u_j - u_{j-1}) + x_j^T Q_j x_j) \\ \text{subject to} \quad & x_{k+1} = f_k(x_k) + g_k(x_k)u_k \end{aligned}$$

Similar to the continuous-time case, the problem in the discrete-time domain also requires manipulation on the cost function and system dynamics. A more general cost function in this case, can be constructed as follows.

$$\begin{aligned} J = \frac{1}{2}\sum_{j=1}^{\infty}(u_j^T R_{1j} u_j + (u_j - u_{j-1})^T R_{2j}(u_j - u_{j-1}) \\ + x_j^T Q_{1j} x_j + (x_j - x_{j-1})^T Q_{2j}(x_j - x_{j-1})) \end{aligned} \tag{4.22}$$

where $R_{1j} = \underline{0}$ and $Q_{2j} = \underline{0}$ correspond to the IDMAR problem.

To represent it in a standard form of quadratic cost function, the new state variable is defined as

$$z_k = \begin{bmatrix} x_{k-1} \\ x_k \end{bmatrix}$$

Dynamic equations of the system can be rewritten for the new augmented system. We have

$$z_{k+1} = \begin{bmatrix} x_k \\ x_{k+1} \end{bmatrix} = F_k(z_k) + G_k(z_k)U_k \tag{4.23}$$

with

$$F_k = \begin{bmatrix} f_{k-1} \\ f_k \end{bmatrix},$$

$$G_k = \begin{bmatrix} g_{k-1} & \underline{0} \\ \underline{0} & g_k \end{bmatrix},$$

and

$$U_k = \begin{bmatrix} u_{k-1} \\ u_k \end{bmatrix}$$

The cost function, correspondingly, can be reconstructed as

$$\begin{aligned} J = \frac{1}{2}\sum_{j=1}^{\infty}(U_j^T \begin{bmatrix} \underline{0} & I_n \end{bmatrix} R_{1j} \begin{bmatrix} \underline{0} \\ I_n \end{bmatrix} U_j + U_j^T \begin{bmatrix} -I_n & I_n \end{bmatrix} R_{2j} \begin{bmatrix} -I_n \\ I_n \end{bmatrix} U_j \\ + z_j^T \begin{bmatrix} \underline{0} & I_n \end{bmatrix} Q_{1j} \begin{bmatrix} \underline{0} \\ I_n \end{bmatrix} z_j + z_j^T \begin{bmatrix} -I_n & I_n \end{bmatrix} Q_{2j} \begin{bmatrix} -I_n \\ I_n \end{bmatrix} z_j) \\ = \frac{1}{2}\sum_{j=1}^{\infty}(U_j^T R_j U_j + z_j^T Q_j z_j) \end{aligned} \tag{4.24}$$

with

$$R_j = \begin{bmatrix} \underline{0} & I_n \end{bmatrix} R_{1j} \begin{bmatrix} \underline{0} \\ I_n \end{bmatrix} + \begin{bmatrix} -I_n & I_n \end{bmatrix} R_{2j} \begin{bmatrix} -I_n \\ I_n \end{bmatrix}$$

$$Q_j = \begin{bmatrix} \underline{0} & I_n \end{bmatrix} Q_{1j} \begin{bmatrix} \underline{0} \\ I_n \end{bmatrix} + \begin{bmatrix} -I_n & I_n \end{bmatrix} Q_{2j} \begin{bmatrix} -I_n \\ I_n \end{bmatrix}$$

The problem statement can be thereby presented in a standard form as follows.

**Problem Statement 5.**

$$\begin{aligned} \underset{U_j}{\text{Minimize}} \quad & J = \frac{1}{2}\sum_{j=1}^{\infty}(U_j^T R_j U_j + z_j^T Q_j z_j) \\ \text{subject to} \quad & z_{k+1} = F_k(z_k) + G_k(z_k)U_k \end{aligned}$$

The IDMAR problem as posed in problem statement 5 can be solved using conventional optimization methods such as Hamiltonian optimization. Also, if the system dynamics is considered a linear time-varying dynamics, recursive LQR algorithms can be used for finding the optimum control inputs.

## 4.2 Simulation Results and Discussions

To demonstrate the effectiveness of minimizing attention to control process, a minimally-attended controller is applied to a four-link planar robot manipulator. As the main concern in this chapter is to investigate the effects of attention optimization, the results presented in this chapter are for the joint-space regulation of the system. The problem is solved in continuous-time domain and the simulation

results for ICMAR optimization are compared with the corresponding joint-space PD controller.

The work space of the manipulator is horizontal. Therefore, the gravitational forces do not affect the motion. Hence, (4.15) reduces to

$$H(q)\ddot{q} + \{\frac{1}{2}\dot{H}(q) + S(q,\dot{q})\}\dot{q} = u. \tag{4.25}$$

For the PD control, we can write

$$u = -K(q - q_d) - C\dot{q} \tag{4.26}$$

where $K$ and $C$ are positive definite matrices, and $q_d$ is the desired joint-space configuration of the manipulator. The corresponding $Q^*$ matrix inside the cost function of ICAMAR problem can then be designed as

$$Q^* = \begin{bmatrix} K & \underline{0} & \underline{0} \\ \underline{0} & C & \underline{0} \\ \underline{0} & \underline{0} & \underline{0} \end{bmatrix} \tag{4.27}$$

Here to realize the damping coefficients of the joints, $C$ is taken from the $Q^*$ matrix and appended to the dynamic equation as follows.

$$H(q)\ddot{q} + \{\frac{1}{2}\dot{H}(q) + S(q,\dot{q}) + C\}\dot{q} = u. \tag{4.28}$$

The new $Q^*$ matrix is selected as

$$Q^* = \begin{bmatrix} K & \underline{0} & \underline{0} \\ \underline{0} & \underline{0} & \underline{0} \\ \underline{0} & \underline{0} & \underline{0} \end{bmatrix}, \tag{4.29}$$

and $R$ matrix can be designed for adjusting the attention during the task as described before.

The parameters of the system are chosen identical to those used in the previous chapter and listed in Table 2.3. Regulation is from the initial point $q_0 =$

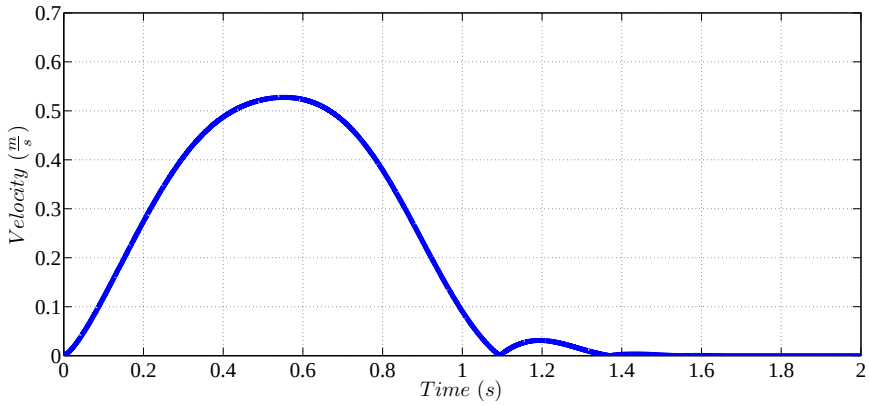


Fig. 4.1: End-effector velocity for ICMAR application

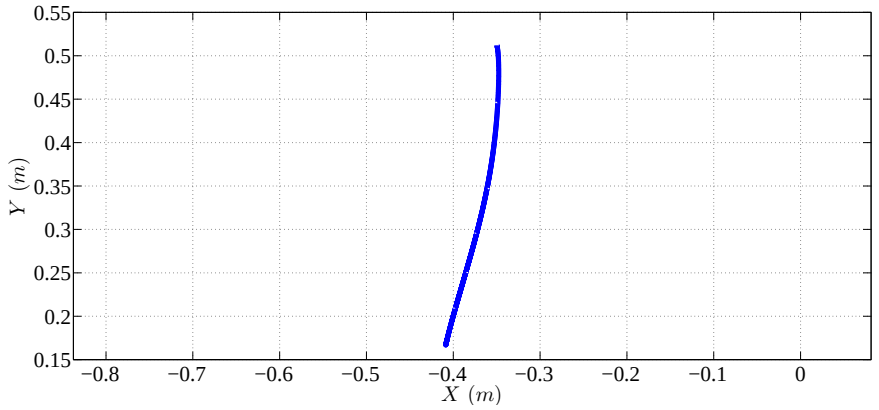


Fig. 4.2: End-effector trajectories for ICMAR application

$(80°, 40°, 50°, 70°)$ to the final point $q_d = (100°, 60°, 70°, 80°)$. The controller parameters are chosen as

$$\alpha = 5,\ \beta = 5$$

$$K = diag(8, 7, 6, 5),\ C = diag(1, 0.9, 0.8, 0.7)$$

$$Q^* = diag(K, \underline{0}, \underline{0}, \underline{0}),\ \ R^* = diag(7, 6, 5, 4)$$

Figure 4.1 shows the velocity of the end-effector upon by application of ICMAR. The velocity profile is bell-shaped and symmetric and converges to zero in about 1.1 $s$. The end-effector trajectory for the same simulation is plotted in figure 4.2. Although the problem is a joint-space regulation, the rectilinear trajectory of the end-effector is achieved by ICMAR.

Figure 4.3 compares the velocity profiles and end-effector trajectories of a simple

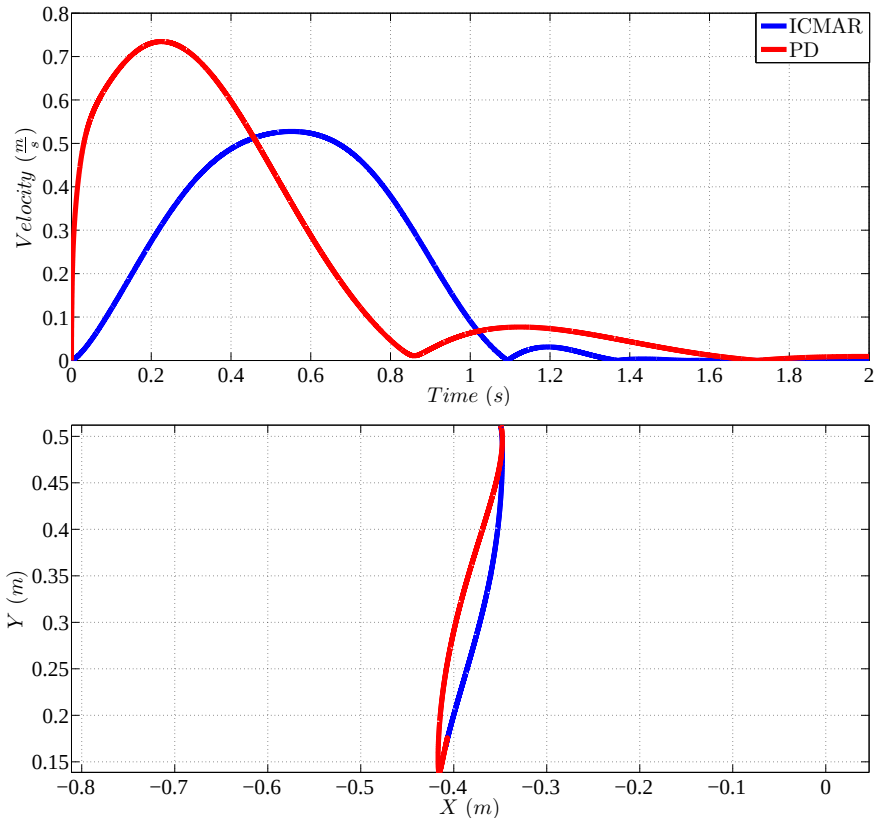


Fig. 4.3: Comparison between velocity profiles and end-effector trajectories generated through ICMAR and simple PD control

joint-space PD controller with ICMAR. In the velocity profile corresponding to ICMAR controller, the peak point moved to the centre of the profile and produced a symmetric profile. Also, the large gradient of the change at the beginning of the profile is reduced in ICMAR compared with PD control. The end-effector trajectory generated by ICMAR becomes more linear than that generated by PD controller.

Figure 4.4 illustrates a duality property that is observed in ICMAR control between the expected profiles of end-effector trajectory and velocity. This figure shows that convergence to a linear trajectory results in the convergence to a bell-shaped velocity profile. The profiles correspond to different values of $C$ matrix which are listed in Table 4.1. In fact, ICMAR enforces the occurrence of both profiles at the same time. Therefore, satisfying a rectilinear end-effector trajectory

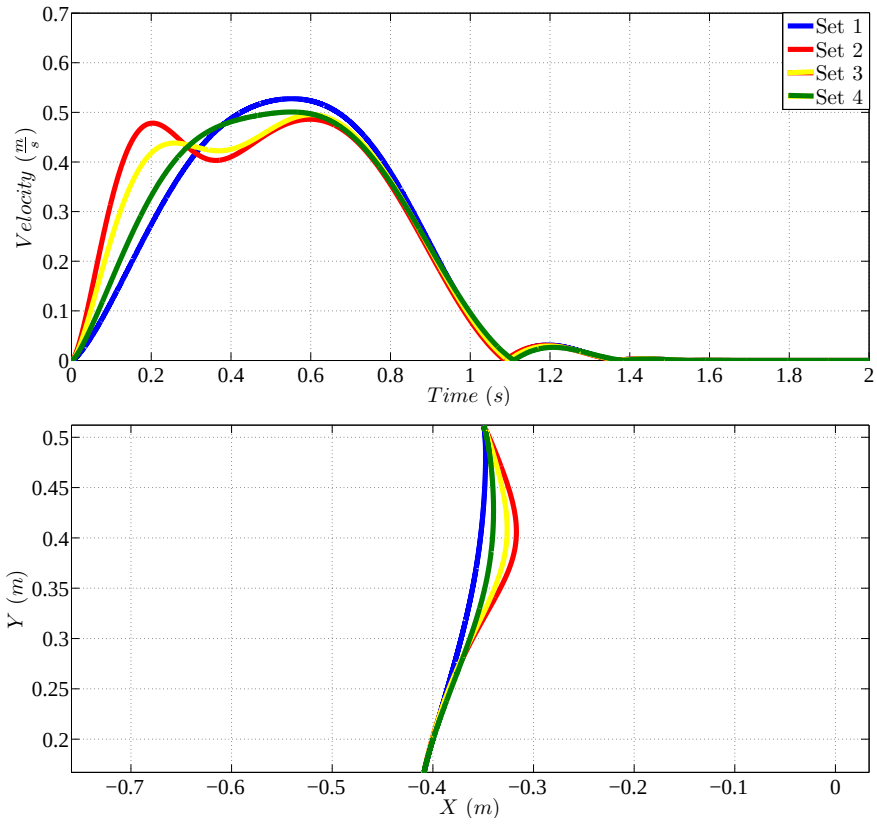


Fig. 4.4: Duality property between bell-shaped profile and rectilinear trajectory

is equivalent to the generation of a bell-shaped velocity profile and vice versa.

Table 4.1: Damping coefficients for duality assessment.

| Parameter | Set one | Set two | Set three | Set four |
|---|---|---|---|---|
| $c_1$ | 1.0 | 1.2 | 1.5 | 2.0 |
| $c_2$ | 0.9 | 0.5 | 0.8 | 0.8 |
| $c_3$ | 0.8 | 0.1 | 0.2 | 0.5 |
| $c_4$ | 0.7 | 0.1 | 0.2 | 0.3 |

## 4.3 Conclusions and Future Works

In this chapter, the effects of optimizing attention to control was investigated by introducing the application of minimally-attended controller for motion control of robot manipulators. The simulation results for joint-space regulation approved

that a bell-shaped velocity profile is achieved through the optimization of the attention to control. Although a joint-space control was considered in computer simulations, a rectilinear trajectory of the end-effector in the task space of manipulator was still observed. A correlation between this trajectory and the bell-shaped velocity profile was also detected which strengthens the hypothesis that attention optimization is an integral part of the control process adopted by human brain.

Here, minimum attention is introduced as an inherent part of the control law in human brain for body movements. It is shown that this type of control results in the emergence of natural characteristics of body limb motions. Minimizing attention in human brain decreases the amount of computation for each specific task. However, the implementation of this control method requires a more intensive computational process compared with a controller which does not attend to how much attention is paid to the control. To present this hypothesis as an explicit control law of human brain for body limb motions, the optimization problem which is solved in real time is required to be replaced by an optimizing formula instead. This can be considered for future modifications on this method.

Future development of the analyses presented in this part of the thesis may include combining minimally-attended regulation for abridged control of the system. This controller would be defined for task-space regulation while the input signals contain the friction forces for the passive joints and control inputs for the active joints. Based on the analyses presented so far, the performance of one such controller is expected to generate the following characteristics.

1. The rectilinear trajectory of the end-effector should be retained as Jacobian transpose and minimally-attended regulator as well as active-Jacobian controller produce such trajectories.

2. It is expected that optimizing attention to control would modify the velocity profile of the reaching tasks. This hypothesis was proven through computer simulations for joint-space regulations in this chapter.

3. The controller would require less computation compared to minimally-attended regulator as the involved DOFs are fewer for under-actuated systems.

Regulating the number of DOFs involved in the control process can be another alternative as a representative of the brain-like control law. The potential controller would consider fewer DOFs in the first stages of reaching and as the end-effector approaches the target point, the active-Jacobian transpose controller converges to the simple Jacobian transpose controller by involving more and more joint-space DOFs. Although human-like motion characteristics can be expected from these two hypotheses, their satisfactory performance cannot be justified without conducting computer simulations.

# Part II

# Self-sensing Exploitation for Energy Conservation in Electromagnetic Devices

# Chapter 5

# Inductive Self-sensing Strategy for Energy-efficient Operation of Electromagnetic Locks

To be energy efficient, electromagnetic (EM) locks should draw a low current in normal working conditions and the current should increase as needed. This introduces different performance phases for the system. *Stand-by* mode is the normal working mode of the system. When the system is turned on, it starts working in the stand-by mode. In this mode, the current flowing through the magnetic coil does not provide a comparable magnetic force to its ultimate strength. The current is kept in a minimum level required for sensing purposes. All the energy conservation occurs during this working mode because the redundant energy consumption of the system is minimized during this phase and the energy consumption retains its minimum value.

A *detection* algorithm needs to observe for any changes in the system and take required measures to guarantee the safety of the low-cost performance of the system. This mechanism performs during the stand-by mode and detects any eminent change in the position of the armature plate due to potential external forces. After detecting a change, an *activation* mechanism needs to recover the position of the armature and ensure its secure attachment to the pole face.

In this chapter, dynamic equations of an EM system are derived and the self-sensing capability of DC EM systems is evaluated. A sophisticated detection algorithm is also presented which considers stochastic properties of the sensing signal to optimize the detection delay. This chapter ends by presenting the performance of different potential activation mechanisms.

## 5.1 System Dynamics

Figure 5.1 shows a schematic of an E-shaped core and its equivalent magnetic circuit. In the magnetic circuit, $R_i$ is the reluctance of different sections of the conducting material and air gap, $N$ is the coil number of turns, $i$ is the current flowing through the coil, and $\phi_1$ and $\phi_2$ are the magnetic fluxes inside the conductors. Figure 5.2 also shows the electronic circuit which supplies the coil. In this figure, $x$ is the relative position of the armature plate from the pole face, $R_c$ is the electrical resistance of the coil, $Z_x$ is the impedance of other components of the electronic circuit other than the coil, $L_c$ is the inductance of the coil, $f_m$ is the magnetic force, $m$ is the mass of the armature, $F_{ex}$ is an external force which represents external disturbances to the system, $V_{sup}$ is the supply voltage, and $V_{sens}$ is the voltage across the coil.

Due to the symmetry in the system, assuming no flux leakage and no eddy-current generation, we can write down the magnetic flux through the coil as follows.

$$\phi = \phi_1 + \phi_2 = 2\phi_1 = \frac{2Ni}{2R_2 + R_4 + R_3 + R_6 + R_1 + 2R_5} \tag{5.1}$$

where

$$R_5 = \frac{x}{\mu_0 A_5} \tag{5.2}$$

and

$$R_6 = \frac{x}{\mu_0 A_6} \tag{5.3}$$

are the reluctances of the air gaps with $\mu_0 = 4\pi \times 10^{-7} H.m^{-1}$ being the permeability of the air, and $A_5$ and $A_6$ the corresponding cross-section areas.

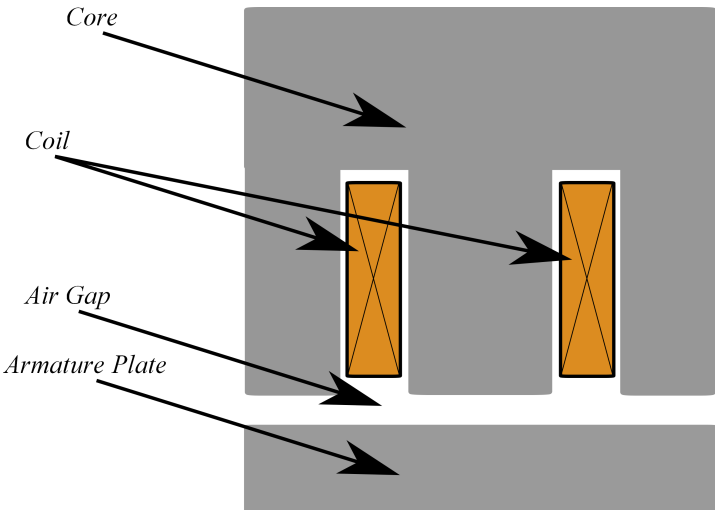


(a) Cross section of the EM system with an E-shaped core

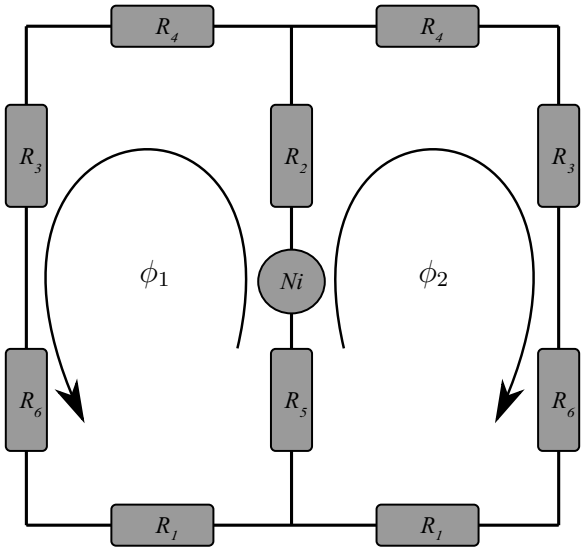


(b) Equivalent magnetic circuit

Fig. 5.1: Schematics of an E-shaped core and its equivalent magnetic circuit

Defining

$$R_{eq} = R_2 + (\frac{1}{2}R_4 + R_3 + R_1) \tag{5.4}$$

as the reluctance of the core material, we can write

$$\phi = \frac{Ni}{R_{eq} + \frac{1}{2}R_6 + R_5}. \tag{5.5}$$

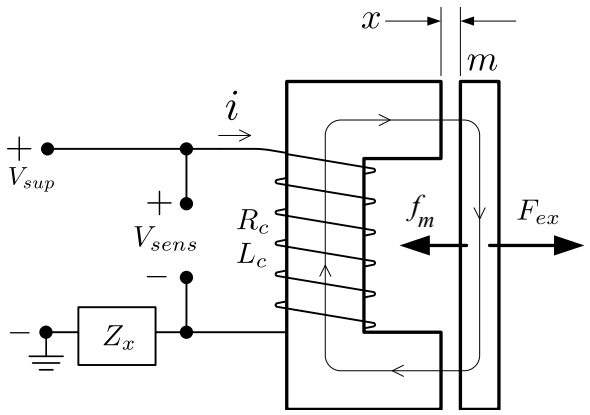


Fig. 5.2: EM system and its electronic circuit

Substituting (5.2) and (5.3) into (5.5), we get

$$\phi = \frac{Ni}{R_{eq} + \frac{(\frac{1}{2A_6} + \frac{1}{A_5})x}{\mu_0}}. \tag{5.6}$$

Defining $A_{eq}$ and $l$ as

$$\frac{1}{A_{eq}} = \frac{1}{2A_6} + \frac{1}{A_5} \tag{5.7}$$

and

$$l = \mu_0 R_{eq} A_{eq}, \tag{5.8}$$

we have

$$\phi = \frac{Ni}{\frac{l+x}{\mu_0 A_{eq}}} = \frac{\mu_0 N A_{eq}}{l+x} i. \tag{5.9}$$

Correspondingly, the flux linkage of the system can be written as

$$\psi = N\phi = \frac{\mu_0 N^2 A_{eq}}{l+x} i \tag{5.10}$$

and the inductance of the system can be computed as

$$L_c = \frac{\psi}{i} = \frac{\mu_0 N^2 A_{eq}}{l+x}. \tag{5.11}$$

Furthermore, applying the Kirchhoff's voltage law to the electronic circuit leads to

$$V_{sup} = (Z_x + R_c)i - emf \tag{5.12}$$

where $emf$ represents the electromotive force (EMF) which is generated due to any changes in the magnetic flux passing through the coil. Based on Faraday's

law of induction, EMF is induced due to a time varying $\psi$ which, in EM systems, manifests as a voltage potential across the coil producing a counter magnetic field opposing the change in the existing magnetic field. Application of Faraday's law to the circuit gives

$$emf = -\frac{d}{dt}\psi. \tag{5.13}$$

Incorporating (5.10) into (5.13), we get

$$emf = -\frac{\mu_0 N^2 A_{eq}}{l+x}\frac{di}{dt} + \frac{\mu_0 N^2 A_{eq}}{(l+x)^2}\dot{x}i. \tag{5.14}$$

In derivation of (5.14), eddy-current effects were neglected. A complete analysis of the behaviour of eddy currents is presented in section 5.2.

Substituting (5.14) into (5.12), the first governing equation of the system can be found as

$$\frac{di}{dt} = \frac{l+x}{\mu_0 N^2 A_{eq}}(V_{sup} - (R_c + Z_x)i + \frac{\mu_0 N^2 A_{eq}}{(l+x)^2}\dot{x}i). \tag{5.15}$$

This equation shows the coupling between the EM and mechanical subsystems. Furthermore, second Newton's law gives

$$m\ddot{x} = F_{ex} + f_m. \tag{5.16}$$

The magnetic force can be calculated as

$$f_m = \frac{d}{dx}(\frac{1}{2}L_c i^2) = -\frac{1}{2}\frac{\mu_0 N^2 A_{eq}}{(l+x)^2}i^2. \tag{5.17}$$

Therefore the position of the armature will change according to

$$m\ddot{x} = F_{ex} - \frac{1}{2}\frac{\mu_0 N^2 A_{eq}}{(l+x)^2}i^2 \tag{5.18}$$

Equations (5.15) and (5.18) constitute the governing equations of the system. Upon application of external forces, armature plate leaves the pole face. The kinematics of separation plays an important role in the practicality of the cost-effective performance of the system and introduces some criteria about the allowable cumulative delay times for different stages of system's performance. Here we assume that the external force is much larger than the stand-by magnetic force so that

the armature plate separates the pole face. Also, the separating force justifies the supposition of neglecting the produced magnetic force in the stand-by mode.

After the application of external force and before the activation of the system for recovery, the distance between the armature and the core can be calculated as

$$x(t) = \int_0^t \int_0^t a_d dt dt \tag{5.19}$$

where $a_d$ is the acceleration of the armature for which we can write

$$a_d = \frac{F_{ex}}{m}. \tag{5.20}$$

After activating the system, the magnetic force increases. Therefore, the cumulative force applied to the armature will be the interaction of the external force and the magnetic force. The acceleration in this phase can be computed as

$$a_a = \frac{F_{ex} - f_m}{m}. \tag{5.21}$$

The distance of the armature after activation can be calculated as

$$x(t) = \int_0^{t_a} \int_0^{t_a} a_d dt dt + \int_{t_a}^{t} (\int_0^{t_a} a_d dt + \int_{t_a}^{t} a_a dt) dt \tag{5.22}$$

where $t_a$ is the activation time, and the first term on the right hand side is the distance at the moment of activation.

Since for recovery we must provide $a_a < 0$, the profile of the distance after activation has a maximum that occurs at $t_{peak}$ when

$$\int_0^{t_a} a_d dt + \int_{t_a}^{t_{peak}} a_a dt = 0. \tag{5.23}$$

The value of the acceleration of the armature after recovery must be negative and it requires $|f_m| > |F_{ex}|$ for $t \geq t_a$. However, the magnitude of the magnetic force decreases with the second power of the distance as armature leaves the core. So, the activation mechanism is required to be robust enough to compensate for the velocity of the armature at $t = t_a$ and the convergence of coil current must be fast enough to compensate for the deteriorated value of the magnetic force.

## 5.2 Analysis of Eddy-current Effect

So far, it was assumed that the energy dissipation is negligible in the magnetic section of the system. However, the generation of eddy currents in time-varying magnetic fields which are the main source of energy loss in such systems is inevitable. Therefore, eddy-current effects can alter the self-sensing capabilities of EM systems.

In this section, the self-sensing capability of DC EM systems is assessed through sophisticated FEM analysis which solves for coupled electromagnetic and structural mechanics modelling of the EM systems. The effects of eddy current generation inside the conductor material is evaluated based on simulation results and new concepts of *eddy-displacement* and *equivalent eddy current*.

The induced voltage in (5.14) was derived by neglecting the effects of eddy currents. Eddy currents inside the conductor material change magnetic properties of the core material by introducing a varying permeability for the conductor. By considering the effects of eddy currents and lumping their effects in the effective length of the magnetic field inside the conductor, (5.14) can be rewritten as

$$emf = V_{ind} = -\frac{\mu_0 N^2 A_{eq}}{(l+x)^2}(\dot{l}+\dot{x})i + L_c\frac{di}{dt} \tag{5.24}$$

where $V_{ind}$ is the induced voltage, and $\dot{l}$ and $\dot{x}$ are the gradients of $l$ and $x$ with respect to time, respectively. On the right hand side of this equation, $\dot{x}$ is due to mechanical movements in the system and $\dot{l}$ and $L_c\frac{di}{dt}$ show the dependency of the induced voltage on the time-varying currents/fields.

Furthermore, the equation governing on the dynamics of the current through the coil can be modified as

$$\frac{di}{dt} = \frac{l+x}{\mu_0 N^2 A_{eq}}(V_{sup} - (R_c + Z_x)i + \frac{\mu_0 N^2 A_{eq}}{(l+x)^2}(\dot{l}+\dot{x})i). \tag{5.25}$$

The voltage over the coil in the electronic circuit is the sensing signal and can be calculated as

$$V_{sens} = R_c i - \frac{\mu_0 N^2 A_{eq}}{(l+x)^2}(\dot{l}+\dot{x})i + L_c\frac{di}{dt} \tag{5.26}$$

where the last two terms on the right hand side, which represent the EMF, depend on $l$, $\dot{x}$, $\dot{l}$, and $\frac{di}{dt}$. Therefore, the magnitude and profile of the external force as well as the dynamics of eddy currents affect the EMF. To study the feasibility of self-sensing method, we need to investigate whether the amount of energy dissipation inside the conductor prevents the induction of a discernible EMF that can be detected within an allowable time duration.

The equivalent length of the magnetic flux can be written as

$$l \equiv \frac{\ell}{\mu_r} + \ell_t \tag{5.27}$$

where $\ell$ is the length of the magnetic flux inside the conductor material for which we have

$$\dot{\ell} = 0,$$

$\mu_r$ is the relative permeability of the conductor material, and $\ell_t$ is a time-varying parameter which represents the nonlinear effects of eddy currents on the effective length of the magnetic path inside the conductor.

For a fully-laminated conductor, eddy-current generation can be neglected. Therefore,

$$\ell_t = \dot{\ell}_t = \dot{l} = 0$$

Hence, (5.24) gives

$$V_{ind}^{fl} = -\frac{\mu_0 N^2 A_{eq}}{(l+x)^2}\dot{x}i + L_c\frac{di}{dt} \tag{5.28}$$

where

$$l = \frac{\ell}{\mu_r}, \tag{5.29}$$

and $V_{ind}^{fl}$ is the induced voltage for a fully-laminated conductor. Equation (5.28) is the same as (5.14) as derived before.

Unlike the straightforward analysis for the fully laminated conductors, due to the nonlinear behaviour of eddy currents, transient behaviour of non-laminated materials requires more intensive analyses. Eddy currents are induced due to the changes in the magnetic field inside the conductors and apply a counter magnetic

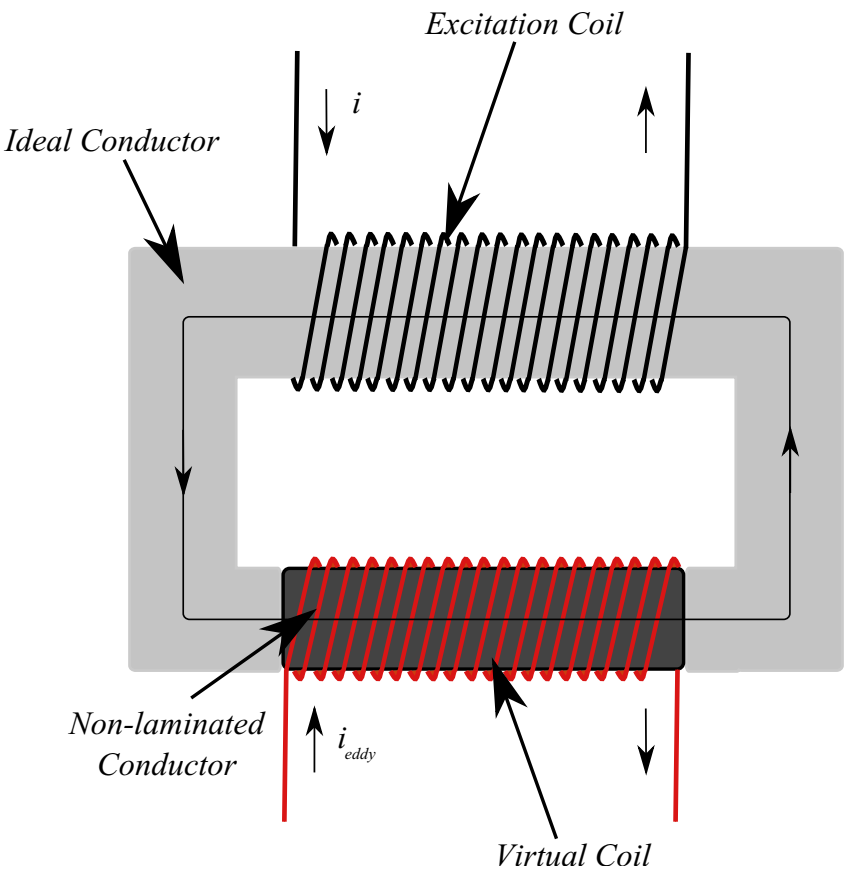


Fig. 5.3: Eddy-current modelling and the virtual coil

field that opposes the variations of the field. Therefore, their magnitude is a function of $\frac{dB}{dt}$ where $B$ is the magnetic flux density inside the conductor. To model the effect of eddy currents, we first consider a system where all sections of the core are ideal conductors without loss of any type except one section. The section is not laminated and thus eddy currents are produced if the magnetic field changes. We consider a solenoid with current $i$ creates the magnetic field in the conductor. In this system, system structure is first assumed to be fixed so $\dot{x} = 0$. Figure 5.3 depicts the corresponding system.

The eddy currents are modelled as a virtual solenoid with the same size and number of coil turns as the main solenoid coil. The current of the virtual coil produces the expected counter magnetic field to count for the eddy-current effects.

The definition of the reluctance yields:

$$R = \frac{Ni}{\phi_{eddy}} \tag{5.30}$$

where $\phi_{eddy}$ is the total magnetic flux flowing through the conductor for which we have

$$\phi_{eddy} = \iint_S BdA = BA_{eq} \tag{5.31}$$

where $\iint_S$ denotes the integral over the cross-section area of the conductor, $A_{eq}$ is an equivalent area, and

$$B = \frac{\mu_0 N(i - i_{eddy})}{l} \tag{5.32}$$

where $i_{eddy}$ is the current through the virtual coil, and $l$ is the length of the coils. In these equations, we used $l$ as the length of the non-laminated section, as well; without loss of generality, the effects of possible differences are lumped into $i_{eddy}$.

Incorporating (5.32) into (5.31) gives

$$\phi_{eddy} = \frac{\mu_0 N A_{eq}}{l}(i - i_{eddy}) \tag{5.33}$$

Therefore, (5.30) is simplified to

$$R = \frac{l}{\mu_0 A_{eq}}(\frac{i}{i - i_{eddy}}) = \frac{l}{\mu_0 A_{eq}}\frac{\phi_{fl}}{\phi_{eddy}} \tag{5.34}$$

Equation (5.34) presents the equivalent reluctance of the system where $\phi_{fl}$ is the magnetic flux for the fully-laminated system which can be computed using (5.33) where $i_{eddy} = 0$. In this case, since the laminated parts of the conductor are assumed to be ideal materials, the reluctance of the system corresponds to that of the non-laminated section; however, in a general case, since different sections of the system contribute to the cumulative reluctance, we have:

$$R = R_{eq}(R_{nl}, R_{others}) \tag{5.35}$$

where $R_{eq}$ is the equivalent inductance of the magnetic system which is a function of $R_{nl}$ (the reluctance of the non-laminated sections) and $R_{others}$ (the equivalent

reluctance of other elements in the system), i.e. laminated conductor sections and air gaps. By adding the motion to the system structure, we can write

$$\phi_{eddy} = \mu_0 N A_{eq}(\frac{i}{l+x} - \frac{i_{eddy}}{l'}) \tag{5.36}$$

where $l$ is defined in (5.29), $x$ is as depicted in Fig 5.2, and

$$l' = \frac{\ell^{nl}}{\mu_r} \tag{5.37}$$

where $\ell^{nl}$ is the length of the non-laminated part of the conductor.

Defining an auxiliary eddy current variable as

$$i'_{eddy} = i_{eddy}(\frac{l+x}{l'}), \tag{5.38}$$

we can simplify (5.36) as following

$$\phi_{eddy} = \frac{\mu_0 N A_{eq}}{l+x}(i - i'_{eddy}). \tag{5.39}$$

Similarly, we can define the cumulative reluctance of the system as

$$R = \frac{l+x}{\mu_0 A_{eq}} \frac{\phi_{fl}}{\phi_{eddy}}. \tag{5.40}$$

Therefore, eddy currents reduce the magnetic field by increasing the equivalent reluctance of the system by

$$R_{eddy} = R - R_{fl} = \frac{l+x}{\mu_0 A_{eq}}(\frac{\phi_{fl} - \phi_{eddy}}{\phi_{eddy}}) \tag{5.41}$$

where

$$R_{fl} = \frac{l+x}{\mu_0 A_{eq}}. \tag{5.42}$$

Equation (5.41) offers a general formula for the eddy reluctance. Depending on the gradient of the magnetic flux, $R_{eddy}$ may adopt positive or negative values. To further simplify the mathematical representation of the eddy-current effects, we introduce a new parameter, namely, "eddy-displacement". Eddy-displacement is a virtual movement that resembles $x$ and is originated from the effects of the produced eddy currents seen by the coil. Eddy-displacement is defined as

$$x_{eddy} = R_{eddy}\mu_0 A_{eq} = (l+x)(\frac{\phi_{fl} - \phi_{eddy}}{\phi_{eddy}}). \tag{5.43}$$

Correspondingly, the total reluctance of the system can be simplified as

$$R = \frac{l + x + x_{eddy}}{\mu_0 A_{eq}}. \tag{5.44}$$

Equation (5.44) presents the reluctance of the system under the effect of the eddy currents. In this equation, $l$, $\mu_0$, and $A_{eq}$ are constant, $x$ is a function of time that depends on external forces and their interactions with the magnetic force, and $x_{eddy}$ is a function of the time-varying magnetic field and is the representative of eddy currents in the formulations. Similar to the auxiliary eddy current, we introduce an auxiliary eddy-displacement as

$$x^{'}_{eddy} = \frac{l^{'}}{l + x} x_{eddy} \tag{5.45}$$

which is a touchstone of energy losses in the system. Eddy-displacement in fact lumps the effects of energy losses, comprising eddy currents and flux leakage, into one variable.

To calculate the induced voltage, we can write

$$L_{eddy} = \frac{\mu_0 N^2 A_{eq}}{l + x + x_{eddy}} \tag{5.46}$$

where $L_{eddy}$ is the inductance of the system under the effect of eddy currents. Therefore, the flux linkage becomes

$$\psi_{eddy} = L_{eddy} i = \frac{\mu_0 N^2 A_{eq}}{l + x + x_{eddy}} i. \tag{5.47}$$

Hence, the induced voltage in the most general case can be computed as

$$V_{ind}^{eddy} = \frac{d\psi}{dt} = -\frac{\mu_0 N^2 A_{eq}}{(l + x + x_{eddy})^2} (\dot{x} + \dot{x}_{eddy}) i + L_{eddy} \frac{di}{dt}. \tag{5.48}$$

## 5.3 Self Sensing

Figure 5.4 shows the current convergence profile for an EM system. The parameters of the system are listed in Table 5.1. System is assumed to be at rest with $x = 0\ m$ and $F_{ex} = 0\ N$. Eddy-current effects are not considered in this simulation. Therefore, the inductance of the system can be computed using (5.46) where

Table 5.1: System parameters for simulation studies.

| Parameter | Value |
|---|---|
| $R_c$ | 100 $\Omega$ |
| $Z_x$ | 500 $\Omega$ |
| $V_{sup}$ | 12 $V$ |
| $N$ | 500 |
| $A_{eq}$ | 0.002 $m^2$ |
| $l$ | $10^{-4}$ |

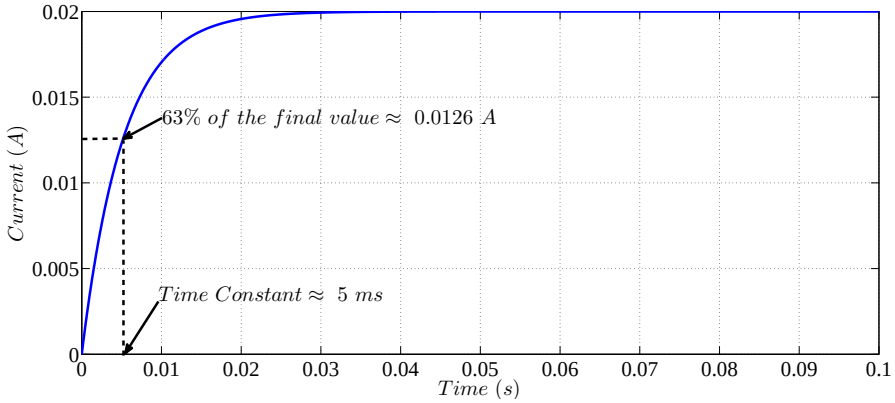


Fig. 5.4: Current Convergence

$x_{eddy} = 0$ which results in $L = 3.14\ H$. The time constant of this system can be calculated as $\tau = \frac{L}{R_c + Z_{ex}} \approx 5\ ms$.

Figure 5.5 plots the magnetic force convergence as a function of supply voltage. This figure shows that the process of reaching a specified force can be expedited considerably by increasing the supply voltage as the gradient of the magnetic force is enhanced twice as fast as the gradient of current.

Figure 5.6 compares the sensing voltages for different values of the external force. The external force is applied as step input to its final value. This figure shows that a comparatively-large induced voltage is produced by armature detachment which can be used for sensing purposes.

Figure 5.7 compares the effect of inductance on the sensing voltage. The re-

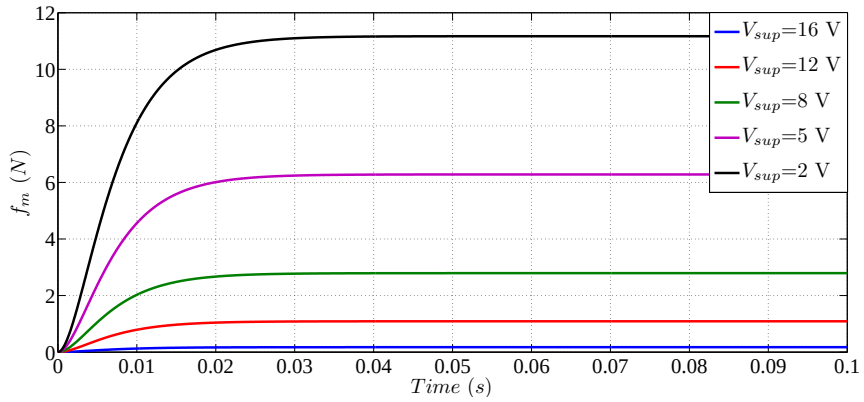


Fig. 5.5: Magnetic force enhancement by increasing the supply voltage

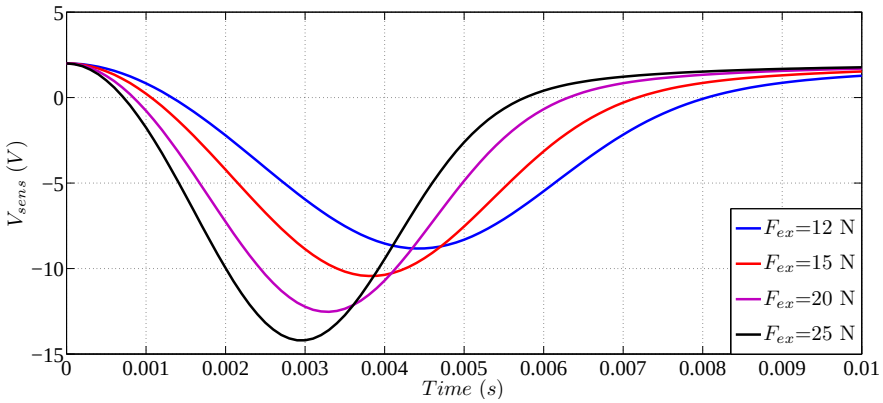


Fig. 5.6: Sensing voltage for different external forces

sistances are set to the values in Table 5.1, the external force is $F_{ex} = 15\ N$, and the inductance is changed by adjusting the number of coil turns $N$. The change of inductance eventuates to the change of the stand-by magnetic force. This figure shows that a higher inductance results in a larger voltage drop.

Figure 5.8 compares the sensing voltage for different stand-by currents. The stand-by current is adjusted by changing the value of the external resistance $Z_x$. A higher stand-by current induces a larger voltage upon armature detachment. Thus, to help the detection mechanism, a larger stand-by current can be chosen. However, the stand-by current is a milestone of the energy consumption of the system, as well. Therefore, selecting this current is a trade-off between a lower energy consumption and a fast detection.

The simulation results approve the emergence of a large induced voltage upon

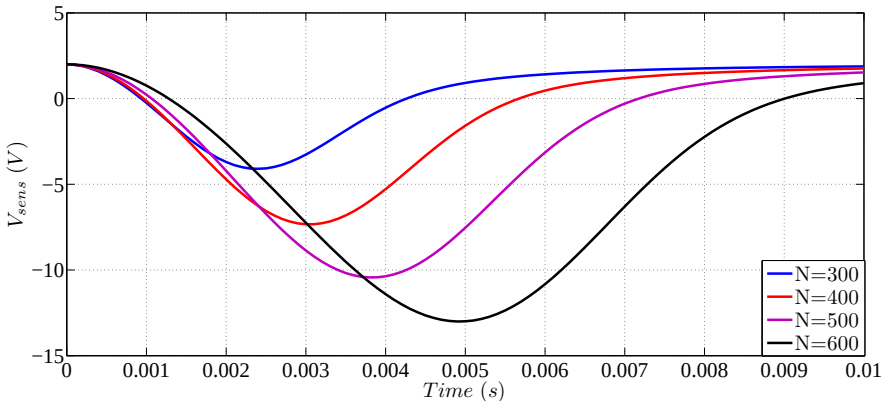


Fig. 5.7: Sensing voltage for different inductance values

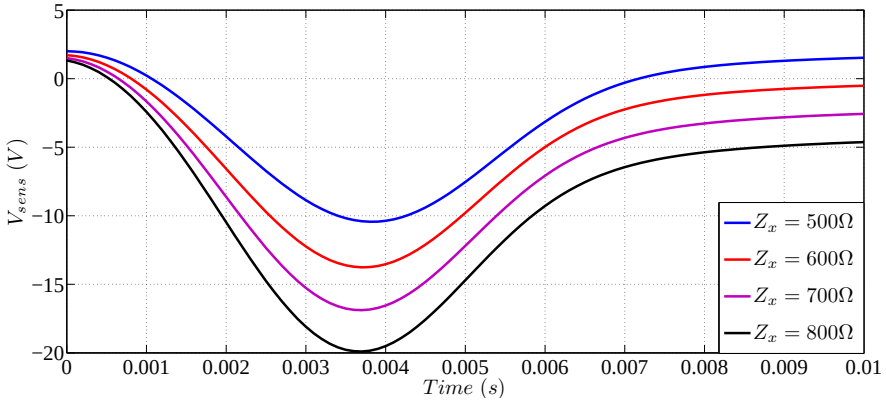


Fig. 5.8: Sensing voltage for different stand-by currents

the application of external force that results in the separation of armature plate. However, the effects of eddy currents were neglected in these simulations. To evaluate such effects, FEM analysis is performed on an EM system with parameters listed in Table 5.2.

The FEM simulations are conducted for a system with different conductors: fully-laminated, partially-laminated, and solid (non-laminated). Different conductor structures are introduced to the software by their electric conductivity matrix. For modelling lamination, the value of conductivity in the direction of lamination was reduced. This value was not set to zero for fully-laminated conductor due to simulation limitations. That is, in the modelled fully-laminated conductor eddy currents are produced; but their density is reduced compared to non-laminated

Table 5.2: System parameters for FEM simulation studies.

| Parameter | Value |
|---|---|
| $R_c$ | 54.5 $\Omega$ |
| $Z_x$ | 500 $\Omega$ |
| $V_{sup}$ | 12 $V$ |
| $N$ | 870 |
| $A_{eq}$ | 0.0016 $m^2$ |
| $l$ | $6.11 \times 10^{-5}$ |
| $m$ | 1.6 $kg$ |
| $F_{ex}$ | 16 $N$ |

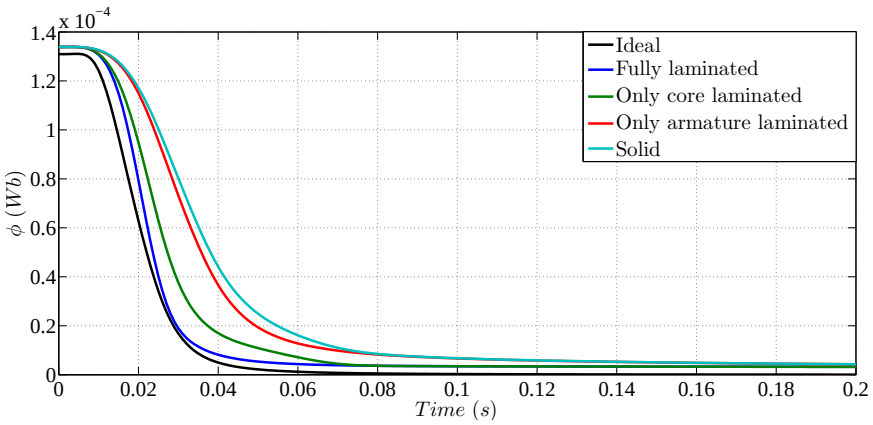


Fig. 5.9: Magnetic flux for different conductor structures

conductors.

Figure 5.9 compares the magnetic flux for each system. The magnetic flux in systems with less lamination converges to zero faster. The ideal magnetic flux is calculated by using the current and position data and applying (5.36) where $i_{eddy} = 0$. Figure 5.10 plots the corresponding auxiliary eddy currents $i'_{eddy}$. As expected, the eddy currents for laminated conductors are produced less than those in the non-laminated conductors.

Figure 5.11(a) shows the position of the armature and figure 5.11(b) plots the corresponding auxiliary eddy-displacements. The eddy-displacement gets larger

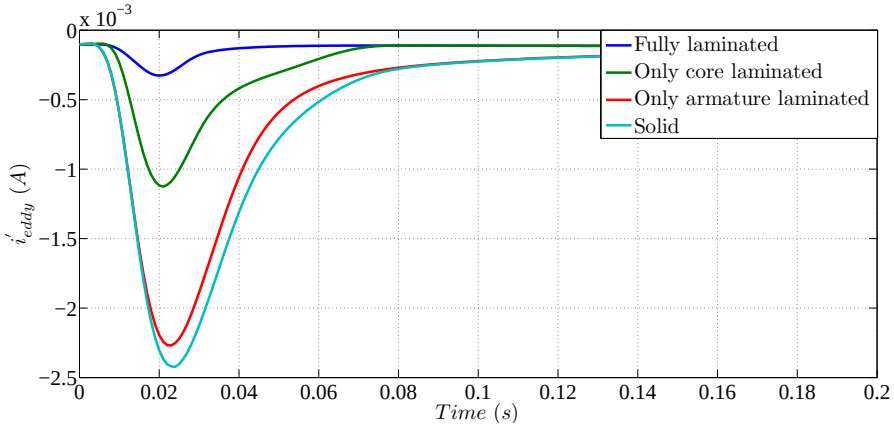


Fig. 5.10: Equivalent auxiliary eddy current for different conductor structures

and larger as the lamination is eliminated from the conductor structure. The position which is seen by the system is $x + x_{eddy}$ which is presented in figure 5.12. This figure shows that system senses a slower change in the position of the armature compared with the actual position which will result in a smaller induced voltage. Due to the structure of the system, at the beginning of the separation, eddy currents contribute mostly in the energy dissipation; and as the armature moves, the flux leakage contribution increases.

The sensing voltage is plotted in figure 5.13. This figure approves the detrimental effects of eddy currents on the sensing voltage. The maximum change in the sensing voltage for a solid conductor is almost half of that in the fully-laminated conductor. Also, the gradient of change at the beginning of the motion is smaller for the solid conductor which results in a slower detection process. This, in turn, can result in an unsatisfactory performance of an energy-efficient EM system. Therefore, the structure of the EM system should be taken into consideration for self-sensing realization purposes.

## 5.4 Detection Algorithm

In this section, a reliable detection algorithm is presented which gives an optimized detection time by considering the stochastic properties of the sensing signal. It was discussed in the previous section that changes in system dynamics introduce

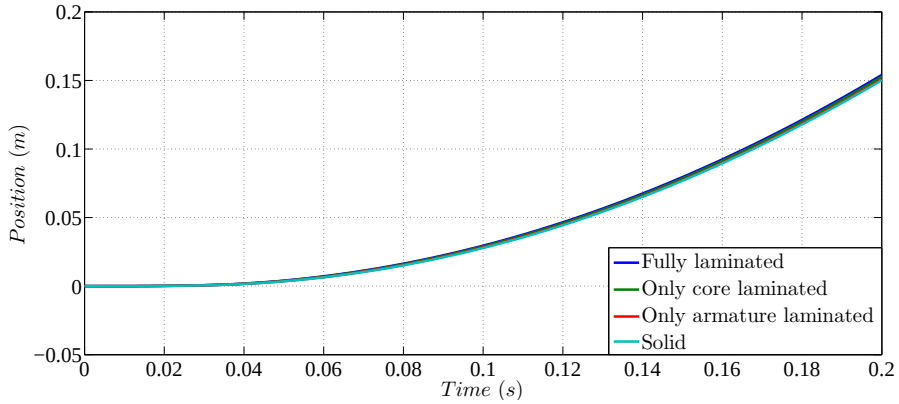


(a) Armature Position

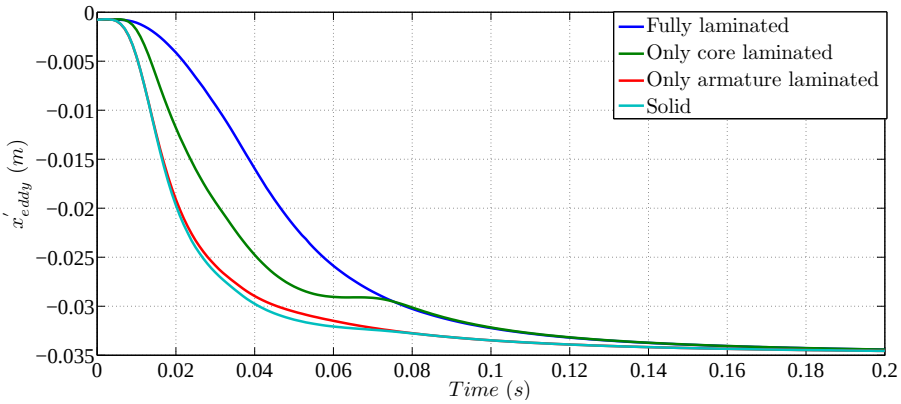


(b) Auxiliary eddy-displacement

Fig. 5.11: Armature position and auxiliary eddy-displacement for different conductor structures

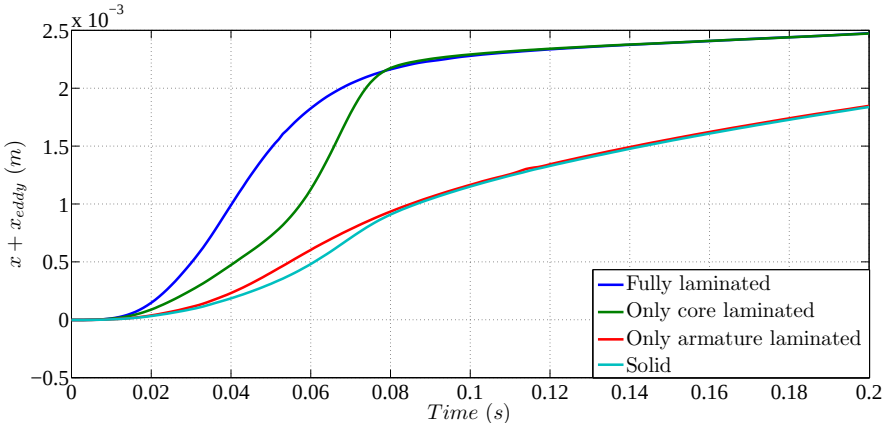


Fig. 5.12: Equivalent movement of the armature

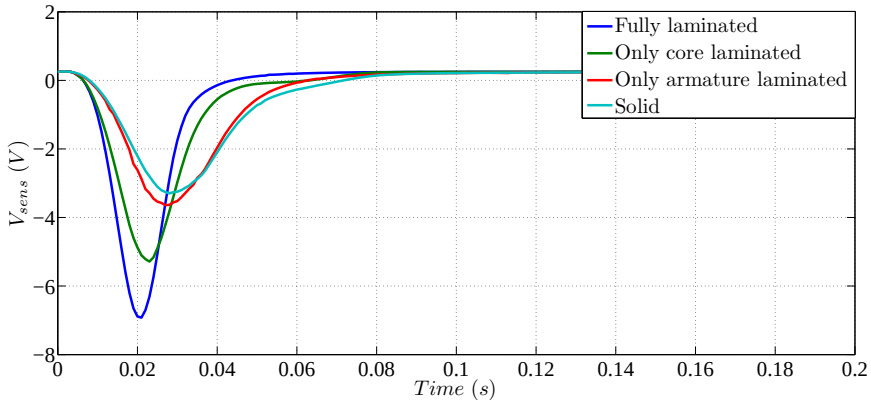


Fig. 5.13: Sensing voltage for different conductor structures

an induced voltage across the solenoid coil which can be recruited for detection purposes. The voltage across the coil, therefore, can be tracked to inspect for any unexpected change which is due to the separation of the armature plate. This voltage can be computed as in (5.48).

The induced voltage emerges and vanished in a very short period of time. Hence, a successful detection mechanism needs to observe for any changes, with minimum delay and false-alarm rate. Due to the existence of many nuisance signals, simple conventional detection algorithms such as threshold check may not be practical. Thus, a more sophisticated detection mechanism that takes into account the stochastic behaviour of the sensing signal should be recruited.

The change detection problem from a mathematical statistics point of view can be posed as to detect the occurrence of a change at an unknown change time based on a sequence of observations with known conditional densities. Considering the change problem in the current application, the final value of the change in the voltage depends on many parameters such as the magnitude and profile of the external force, the stand-by current, and mechanical and electromagnetic properties of the system. The *a priori* information about the signal is the initial value and the standard deviation of the signal. Thus the detection problem deals with known initial and unknown final values of the signals. Generalized likelihood ratio (GLR) algorithm can be recruited in such cases [99]. Such detection problem is based on

a double maximization of a family of functions of observations. In general, the GLR decision function is defined as

$$g_k = \max_{1 \le j \le k} \sup_{\theta_1} S_j^k(\theta_1) \tag{5.49}$$

where

$$S_j^k(\theta_1) = \sum_{i=j}^{k} s_i \tag{5.50}$$

is the log-likelihood ratio for the observations from time step $j$ up to time step $k$ with $s_i$, sufficient statistics, defined as

$$s_i = ln \frac{p_{\theta_1}(y_i)}{p_{\theta_0}(y_i)}. \tag{5.51}$$

where $\theta_0$ is the initial value of the signal, $\theta_1$ is the final value of the signal, $y_i$ is the $i^{th}$ observation, and $p_{\theta_0}$ and $p_{\theta_1}$ are two density functions with respect to the initial and final values of the signal.

For the case when the final value of the change is unknown, the change detection problem statement is to detect the change in

$$\theta(k) \begin{cases} = \theta_0 & \text{when } k < t_0 \\ \neq \theta_0 & \text{when } k \ge t_0 \end{cases}$$

where $t_0$ is an unknown change time.

The decision function for this problem can be designed as [90]

$$g_k = \max_{1 \le j \le k} ln \frac{\sup_\theta \prod_{i=j}^{k} p_\theta(Y_i)}{\prod_{i=j}^{k} p_{\theta_0}(Y_i)} \tag{5.52}$$

where $Y_i$ is the sequence of observations. The decision function can be further simplified as

$$\begin{aligned} g_k &= \max_{1 \le j \le k} \frac{k-j+1}{2} (\bar{Y}_j^k - \theta_0)^T \Sigma^{-1} (\bar{Y}_j^k - \theta_0) \\ &= \max_{1 \le j \le k} \frac{k-j+1}{2} (\chi_j^k)^2 \end{aligned} \tag{5.53}$$

where

$$\bar{Y}_j^k = \frac{1}{k-j+1} \sum_{i=j}^{k} y_i, \tag{5.54}$$

$\Sigma$ is the covariance of the observed signal ($\Sigma = E_\theta(y_i y_i^T)$), and $(\chi_j^k)^2 = (\bar{Y}_j^k - \theta_0)^T \Sigma^{-1} (\bar{Y}_j^k - \theta_0)$ is called the chi-squared distribution of $\bar{Y}$ [90].

### 5.4.1 GLR with Fixed-size Sliding Window

The GLR algorithm as presented here records the observation data from the beginning until the current observation. This may not be efficient as it increases the memory requirements, exponentially. Also, as time advances, the amount of effective information that past observations present reduces. Hence, to increase the efficiency of the algorithm and to reduce the cost of computations, a fixed-size sliding window is introduced which computes the decision function only based on the last $M$ data samples where $M$ is the window size. Correspondingly, the detection function can be modified as

$$g_k = \max_{k-M+1 \leq j \leq k} \frac{k-j+1}{2} (\chi_j^k)^2 \tag{5.55}$$

for $k \geq M$. Equation (5.53) still holds for $k < M$.

The change in the sensing signal can then be detected by comparing the value of the detection function with a threshold $h$. Hence, the control law can be designed as follows.

$$d_k = \begin{cases} 0 & g_k < h \\ 1 & g_k \geq h \end{cases}$$

where $d_k = 1$ is the indicator of a change.

The problem that arises for fixed-size sliding window GLR is the proper selection of the window size $M$ along with the selection of the threshold value $h$. For a fixed window size $M$ a convenient threshold value $h$ can be derived [135]. However, finding a satisfactory pair of window size and threshold value can be very difficult [100].

### 5.4.2 Estimation of the Change Time

The change time can be estimated off-line. The problem is to estimate the change time while all the parameters of the signal such as $\theta_0$, $\theta_1$, and $t_0$ can be assumed

to be unknown. To find these parameters, their maximum likelihood estimate (M.L.E.) is used for which we have [90]

$$(\hat{t}_0, \hat{\theta}_0, \hat{\theta}_1) = \arg \max_{1 \le k \le S} \sup_{\theta_0} \sup_{\theta_1} ln\Big[ \prod_{i=1}^{k-1} p_{\theta_0}(y_i) \prod_{i=k}^{S} p_{\theta_1}(y_i) \Big] \tag{5.56}$$

which can be reduced into

$$\hat{t}_0 = \arg \max_{1 \le k \le S} ln\Big[ \prod_{i=1}^{k-1} p_{\hat{\theta}_0}(y_i) \prod_{i=k}^{S} p_{\hat{\theta}_1}(y_i) \Big] \tag{5.57}$$

where $S$ is the size of the data set, $\hat{\theta}_0$ is the M.L.E. of $\theta_0$ based upon the first $k-1$ observations and $\hat{\theta}_1$ is the M.L.E of $\theta_1$ based on the last $S-k+1$ observations.

For a scalar Gaussian independent random variable with a known constant covariance $\sigma^2$ and unknown mean values before and after the change, M.L.E formula (5.57) can be simplified as

$$\hat{t}_0 = \arg \max_{1 \le k \le S} \Big\{ \sum_{i=1}^{k-1} (y_i - \hat{\mu}_0)^2 + \sum_{i=k}^{S} (y_i - \hat{\mu}_1)^2 \Big\} \tag{5.58}$$

where $\hat{\mu}_0 = \frac{1}{k-1} \sum_{i=1}^{k-1} y_i$ and $\hat{\mu}_1 = \frac{1}{S-k+1} \sum_{i=k}^{S} y_i$. To derive this formula the equation of probability density function for normal distribution was substituted in (5.57).

Equation (5.55) can be used for detection of any discernible induced voltage under the effects of nuisance signals. Equation (5.58) can be applied for off-line estimation of the detection time.

Figure 5.14 shows the delay time versus the logarithmic scale of the threshold values $h$ for $M = 20$. Large values of the threshold introduce larger detection delays while small values increase the probability of false alarms. To compute the detection time, (5.58) is applied to the induced voltage of an EM system with the properties and external force listed in Table 5.3. The sensing signal is plotted in figure 5.15 and the corresponding noise signal is shown in figure 5.16.

Figure 5.17 shows the delay time as a function of the window size for $h = 50$. This profile can be approximated as a line. This figure shows that large window sizes delay the detection process. However, small windows increase false-alarm rates. When $M = 1$, the stochastic detection problem becomes a simple threshold check which only considers the last observation.

Table 5.3: Parameter values for delay time calculations.

| Parameter | Symbol | Value |
|---|---|---|
| Supply voltage | $V_{sup}$ | 12 $V$ |
| External resistor | $Z_x$ | 700 $\Omega$ |
| Internal resistor | $R_c$ | 54.5 $\Omega$ |
| Inductance at steady state | $L_c$ | 20 $H$ |
| External force | $F_{ex}$ | 60 $N$ |

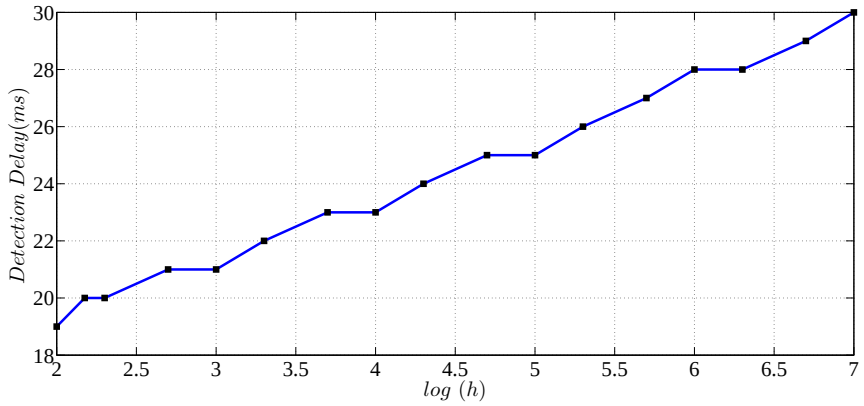


Fig. 5.14: Detection time for different threshold values

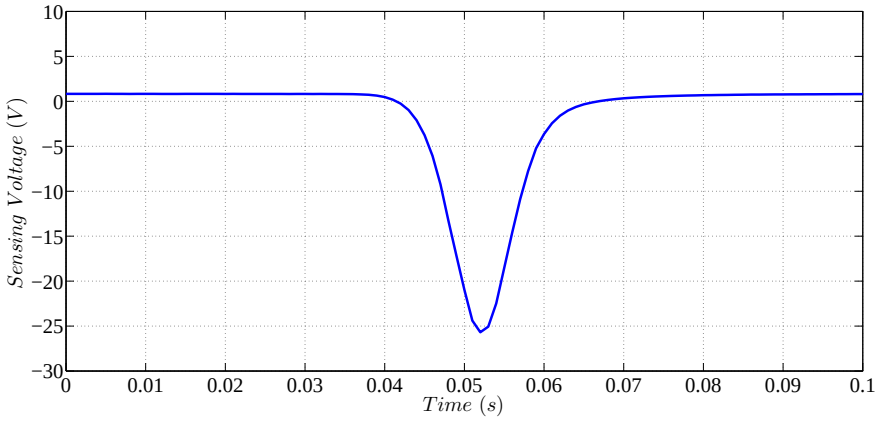


Fig. 5.15: Sensing signal

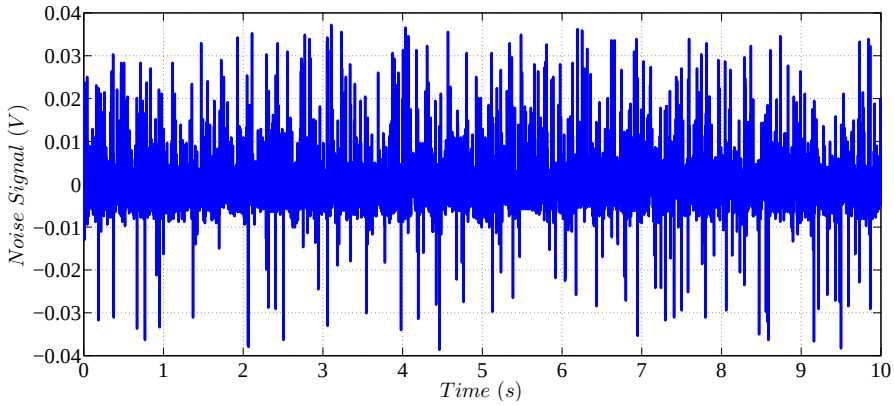


Fig. 5.16: Noise signals

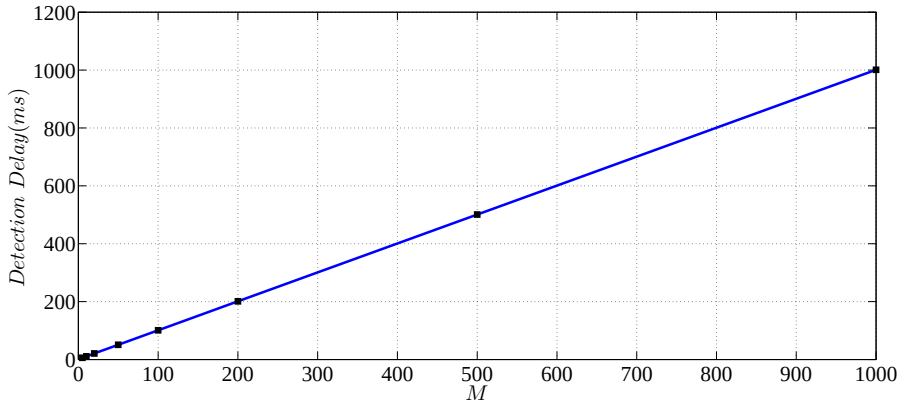


Fig. 5.17: Detection time for different window sizes

## 5.5 Activation Mechanisms

The next stage in the control process after detecting disturbances is activating the system to its full power. The main criterion that potential activation mechanisms need to satisfy is the compensation for the time constant of the system. The activation process deals with the inductive behaviour of the EM system and reduces the time that current takes to converge to its nominal value. Two types of activation circuits are introduced in this section and computer simulations for the performance of the closed-loop system for each activation method are presented.

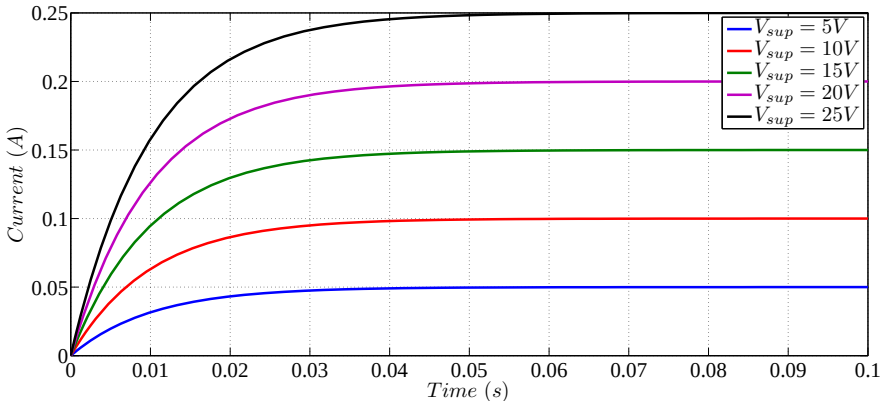


Fig. 5.18: Enhancing current values by high supply voltages

### 5.5.1 Direct Activation

The simplest way to increase the magnetic force is to ramp-up the current by connecting a high voltage across the coil. For an electronic circuit with a resistance and an inductance (RL circuit), the current converges to its final value with a gradient proportional to the supply voltage. Therefore, increasing the supply voltage will enhance the convergence speed. Figure 5.18 shows the current profile for different supply voltages in an RL circuit with $R = 100\ \Omega$ and $L = 1\ H$. This figure shows that although the time constant of the system remains the same($\tau = \frac{L}{R} = constant$), the time that current takes to reach a predetermined value decreases by increasing the supply. This fact is the basis of direct activation circuit designs.

Figure 5.19 demonstrates a candidate circuit for current/voltage amplification. This circuit regulates the voltage across $R_3$ which, in turn, regulates the current flowing through the magnetic coil. The input voltage $V_{in}$ is given to a voltage-divider ($R_1$ and $R_2$) and the operational amplifier sets the voltage across $R_3$. This voltage can be computed as

$$V_3 = \frac{R_2}{R_1 + R_2} V_{in}. \tag{5.59}$$

Therefore, the current passing through $R_3$ becomes

$$i_3 = \frac{V_3}{R_3} = \frac{R_2}{R_3(R_1 + R_2)} V_{in} \tag{5.60}$$

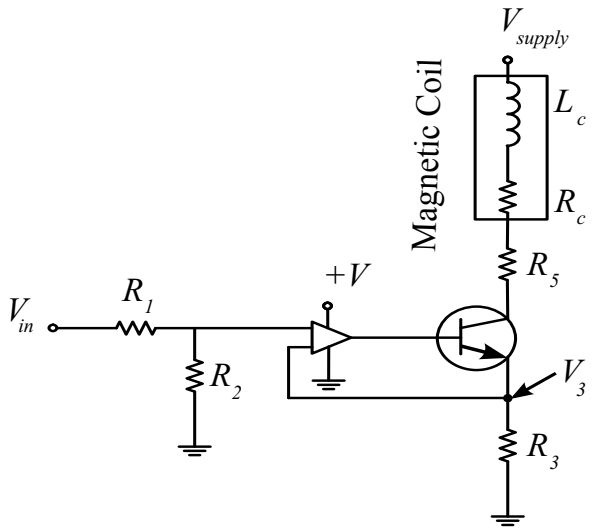


Fig. 5.19: Schematic of a current amplifier circuit

which is proportional to the input voltage. This current is provided by the main supply voltage and flows through the transistor. The current flowing through the magnetic coil is almost the same as this current (its exact value is $i_{coil} = \frac{\beta}{\beta+1} i_3$ with $\beta$ being the common-emitter current gain of the transistor.) Therefore, the activation of the EM system can be achieved by setting the value of the input voltage $V_{in}$.

This circuit needs a continuous supplication of the high voltage. Electronic devices such as DC-DC or AC-DC converters which provide high voltages have their own energy consumption which is added to the total energy consumption of the system. Therefore, isolation of this high voltage from the circuit saves some portion of energy consumption. This isolation also reduces the risk of electric shocks for the operators. Therefore, the activation circuit should be separately designed and appended to the system. Figure 5.20 shows how different sections of a closed-loop system can correlate with each other.

The main components of the circuit are the stand-by mode circuit, the activation circuit, and the switching elements. Switching elements connect the EM system to either the stand-by mode or the activation mode circuitries. It receives control signals from a processing unit that monitors the voltage across the coil and

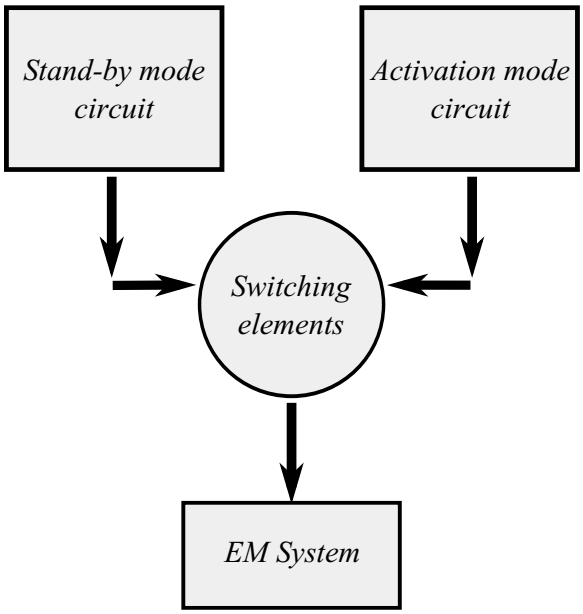


Fig. 5.20: Main components of a candidate circuit

analyses it to detect any changes in the system.

To isolate the high voltage from the circuit during the stand-by mode, a set of fast switching elements are needed. The performance delay of power transistors and solid-state relays is within a few milliseconds. Therefore, they can be used as reliable switches for connecting activation circuit to the EM system. The stand-by circuit is connected to the system and, after detection, the switches toggle the connection from stand-by to activation.

In the stand-by mode, the current should be reduced to remove the redundant power consumption. Increasing the total resistance of the circuit will decrease the current. Thus, a resistor is used in series combination with the system to increase the cumulative resistance which reduces the stand-by current. This resistor can be removed during the activation phase to improve the convergence profile of the current. Figure 5.21 compares the current profile of an RL circuit for different values of the external resistance. In these simulations, $L = 1H$, $R = 100\Omega$, $V_{sup} = 12VDC$, and the external resistor is denoted by $R'$.

Adding a resistance reduces the time constant of the system based on

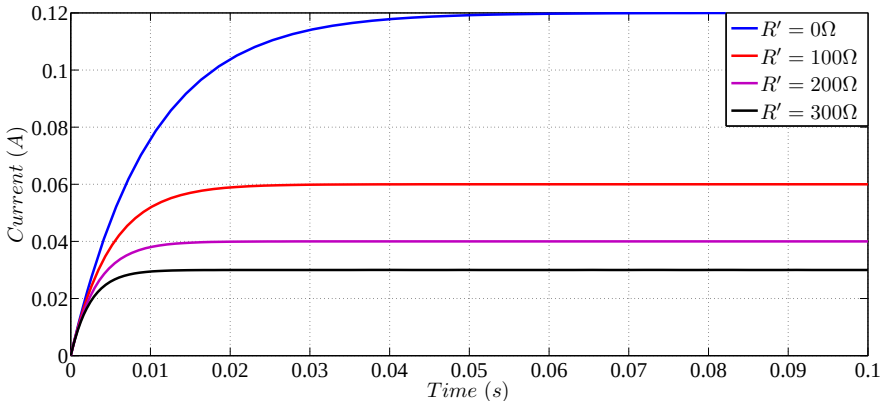


Fig. 5.21: Comparison between the time constant and current profile by adding an external resistor

$$\tau = \frac{L}{R + R'}. \tag{5.61}$$

But the gradient of the current profile is the same for different resistances. The current profile of an RL circuit for a step input is

$$i = \frac{V_{sup}}{R + R'}(1 - e^{-\frac{t}{\tau}}). \tag{5.62}$$

Therefore, we can write

$$\frac{di}{dt} = \frac{V_{sup}}{R + R'}\frac{1}{\tau}e^{-\frac{t}{\tau}}. \tag{5.63}$$

Incorporating (5.61) into (5.63) gives

$$\frac{di}{dt} = \frac{V_{sup}}{L}e^{-\frac{t}{\tau}}. \tag{5.64}$$

So, the maximum value of the gradient occurs at $t = 0$ and is the same for all values of $R'$. Hence, changing the resistance of the circuit does not reduce the time that current takes to reach a predefined value. Therefore, the high voltage should be directly connected to the EM block. Figure 5.22 shows a schematic of the direct-activation circuit with an isolated high-voltage supply. The high-voltage supply can be provided by using a DC-DC boost converter as an external device or by designing a voltage booster to increase the nominal supply voltage. Figure

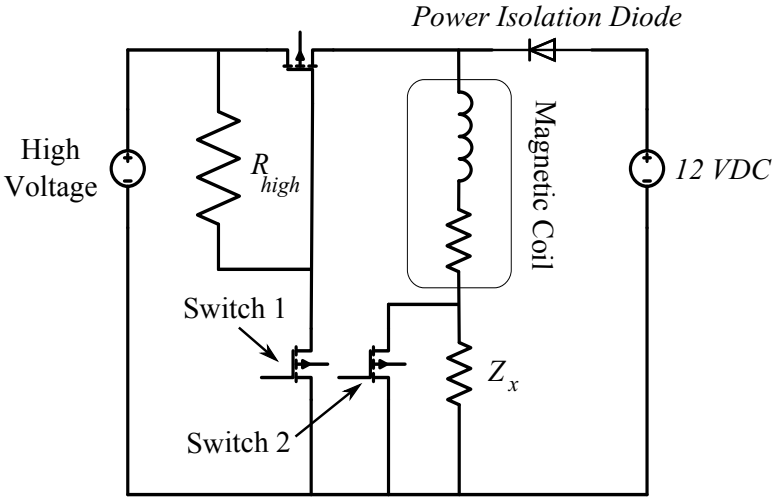


Fig. 5.22: Schematic of the high-voltage direct-activation circuit

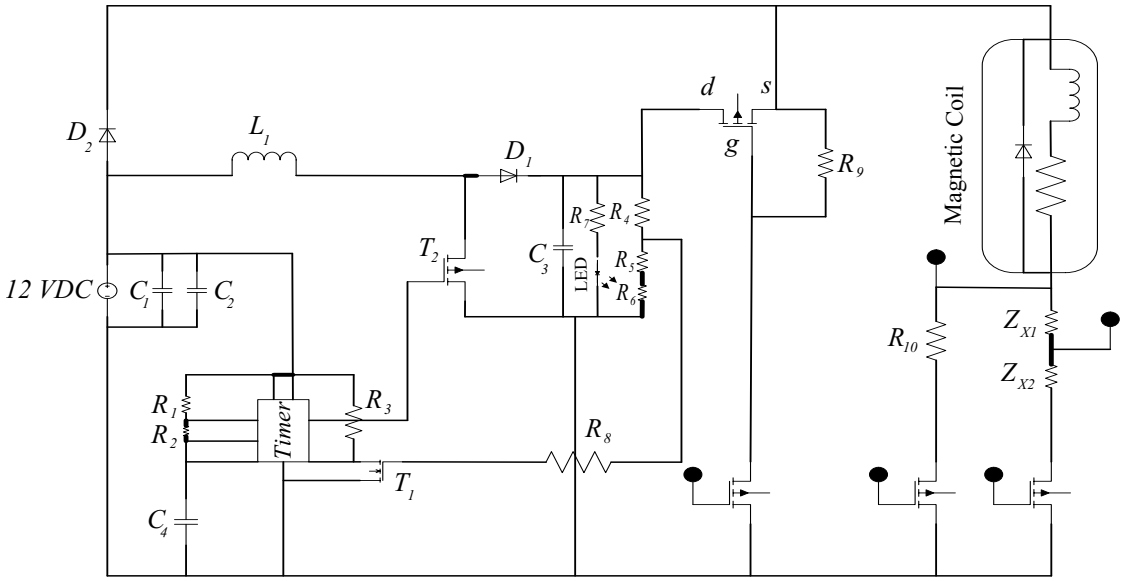


Fig. 5.23: Schematic of the control circuit with a voltage booster

Table 5.4: Parameter values for high-voltage activation simulations.

| Parameter | Symbol | Value |
|---|---|---|
| Supply voltage | $V_{sup}$ | 12 $V$ |
| Stand-by resistor | $Z_x$ | 500 $\Omega$ |
| Coil number of turns | $N$ | 500 |
| Equivalent length of the conductor | $l$ | $10^{-4}$ $m$ |
| Equivalent cross-section area of the conductor | $A_{eq}$ | 0.001 $m^2$ |
| Resistance of the coil | $R_c$ | 100 $\Omega$ |
| Mass of the armature | $m$ | 200 $g$ |
| High-voltage supply | $V_{up}$ | 40 $V$ |
| External force | $F_{ex}$ | 80 $N$ |

5.23 shows the schematic of a voltage booster which uses conventional electronic elements to enhance the supply voltage to high values.

The high-voltage supply is connected to the EM system after detection and is disconnected after the current reaches a safe level producing a secure magnetic force. Therefore, the auxiliary supply voltage is used only in a short period of time; hence it does not affect the energy consumption of the system, noticeably. The transient behaviour of the EM system during the operation of the current ramp-up is illustrated in figure 5.24. Figures 5.25 and 5.26 compare the position profiles for different high voltages and external forces, respectively. The simulation parameters are listed in Table 5.4. Both switches are ON after detection. To prevent unnecessary energy consumption, after current reaches a safe value $i_{safe}$, the high-voltage supply is disconnected and the nominal supply voltage is connected to the EM system. The state of the system after activation phase is called restoration mode.

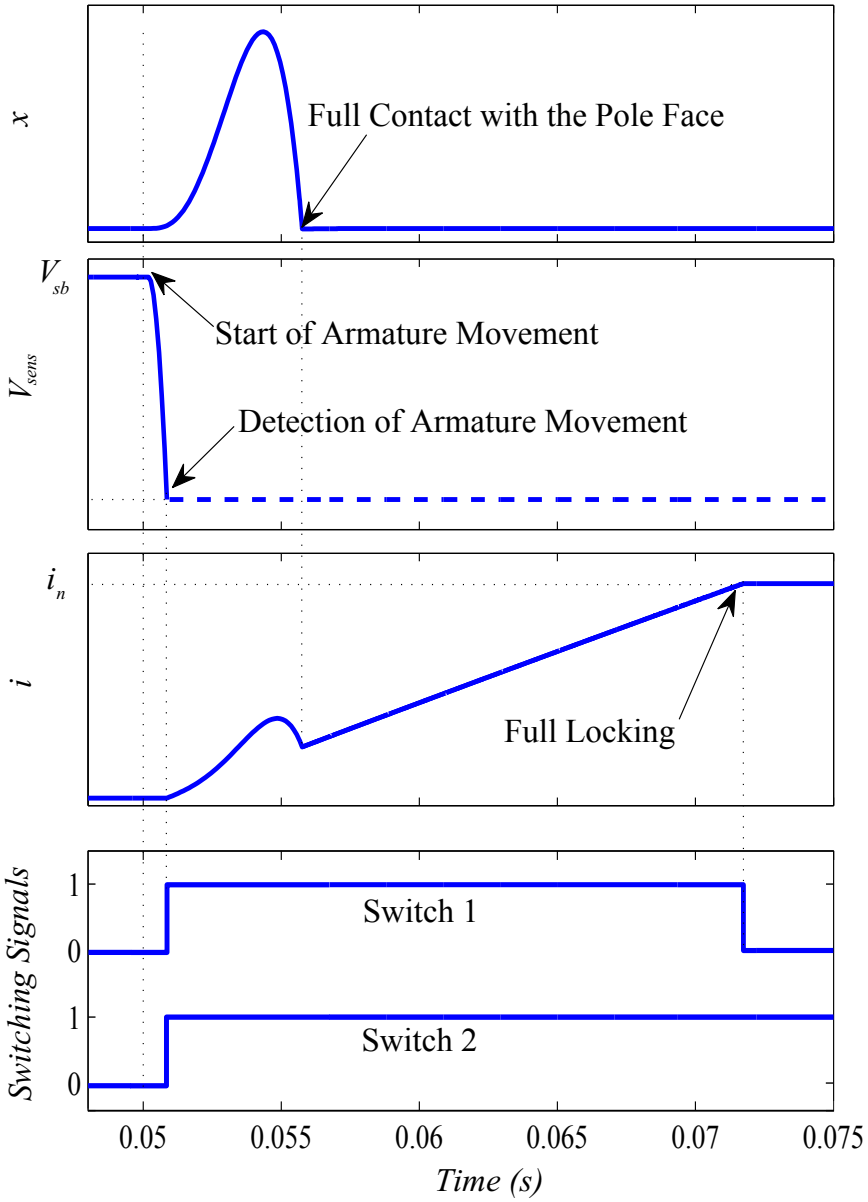


Fig. 5.24: Typical response of variables of the EM system with respect to the operation of switching elements during the current ramp-up

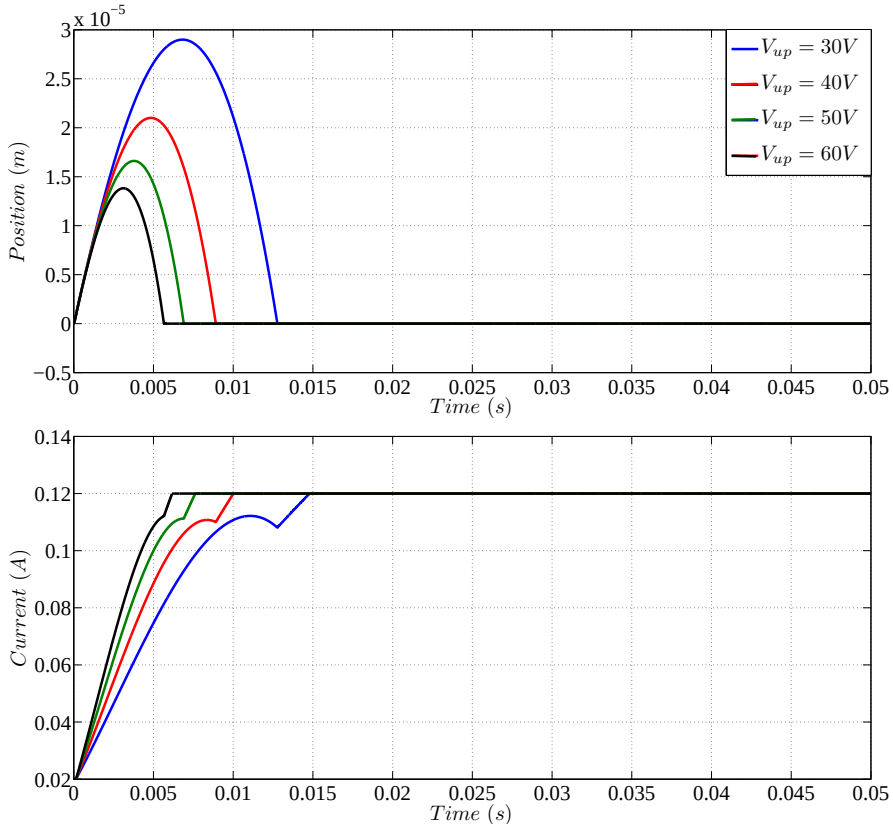


Fig. 5.25: Performance of EM system upon the application of high-voltage activation circuit for different high-voltage supplies

### 5.5.2 Indirect Activation

Indirect activation circuits use the dynamic characteristics of electronic circuits for the design of activation circuitry. Two types of indirect activation circuits are introduced and discussed in this section: capacitor-based circuit and inductor-based circuit.

#### 5.5.2.1 Capacitor-based Activation

Capacitors can be used to reduce the inductive behaviour of the system. In the activation stage, by placing a capacitor in series combination with the EM unit, the time constant of the system will decrease. This property is used in the design of capacitor-based activation circuits.

Some benefits of capacitor-based circuit design are

1. Reducing energy consumption by preventing any excess energy consumption

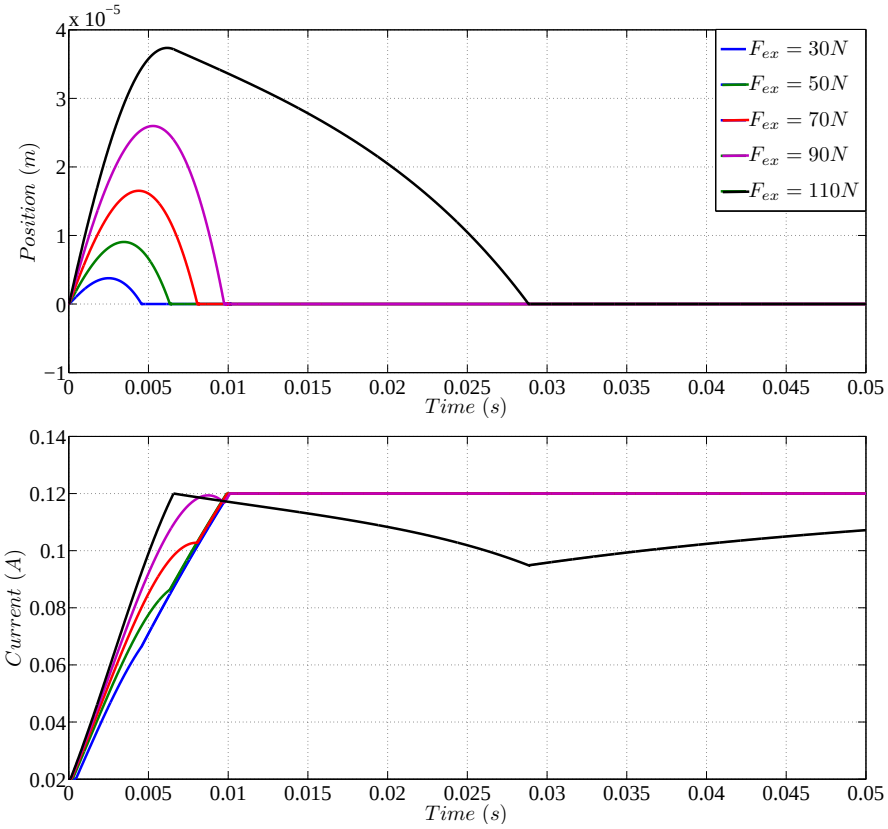


Fig. 5.26: Performance of EM system upon the application of high-voltage activation circuit for different external forces

by properly selecting the capacitance.

2. Reducing the required supply voltage which will also reduce the risk of potential electric shocks.

3. Simplicity and cost: capacitors are cheaper and simpler than voltage converters.

By introducing a capacitive element that modifies the current ramp-up profile, the overall time constant of the system can be improved. Stand-by and restoration modes are the same as those in the previous design. In the activation mode, the solenoid coil is connected to a capacitor in series to decrease the overall inductance of the system. Figure 5.27 shows the schematic of the capacitor-based control circuit for time-constant reduction. $R_{high}$ is a large resistor which is embedded to

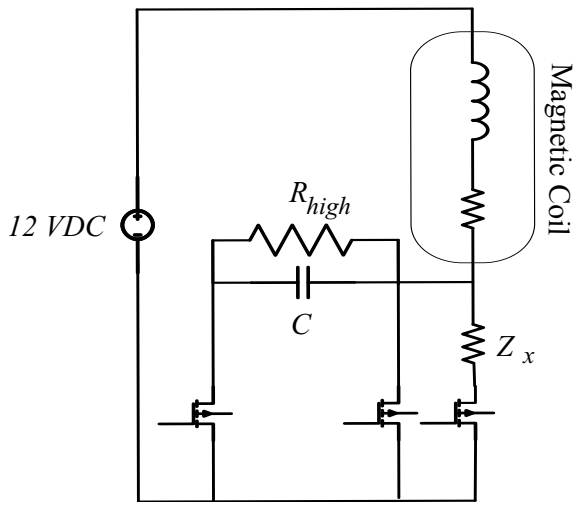


Fig. 5.27: Schematic of the capacitor-based activation circuit for time-constant reduction

the design to discharge the capacitor during the stand-by mode.

The performance of this activation circuit is shown in figures 5.28 and 5.29 for different activation capacitors and external forces, respectively. The activation capacitor is $C = 500\mu F$ and the external force is $F_{ex} = 25N$ and system parameters are as those is Table 5.4.

#### 5.5.2.2 Inductor-based Activation

The activation circuits introduced so far provide the EM block with either a high voltage or a modified circuit design during activation stage to enhance the current ramp-up profile. For inductive elements, the induced voltage produced across the element inhibits abrupt changes in the current. Therefore, a sudden change in the value of the current is impossible for inductors. This sudden change can be approached, however, by increasing the supply voltage in the high-voltage activation control. The limit is an extremely high voltage (e.g., a spark voltage) to ramp-up the current in an instant. This is the basic idea in the inductor-based circuit design.

This method recruits a supplementary inductor for the control process. This inductor carries a high current during the stand-by mode. Connecting this inductor to the EM coil constitute the activation process. Since both elements have

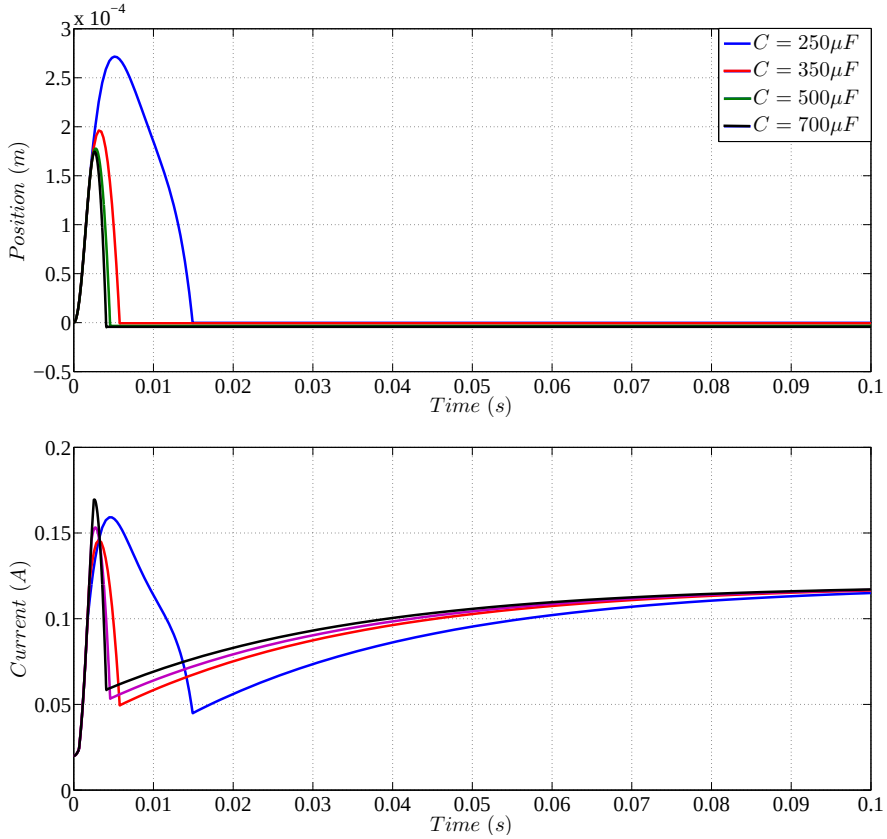


Fig. 5.28: Performance of the capacitor-based activation circuit for different capacitor values

inductive behaviour, neither of them can accept an immediate change in the current. However, connecting them in series imposes an identical current flowing through both of them. Therefore, they automatically produce a spark voltage for a short period of time. This spark voltage increases the current in the EM coil and decreases the current in the supplementary inductor.

Assuming there is no energy dissipation during this course of action, we can use the energy conservation principle to compute the current after connection. Denoting the stored energy of the system before the connection by $E_1$ and after the connection by $E_2$, we can write

$$E_1 = E_2 \tag{5.65}$$

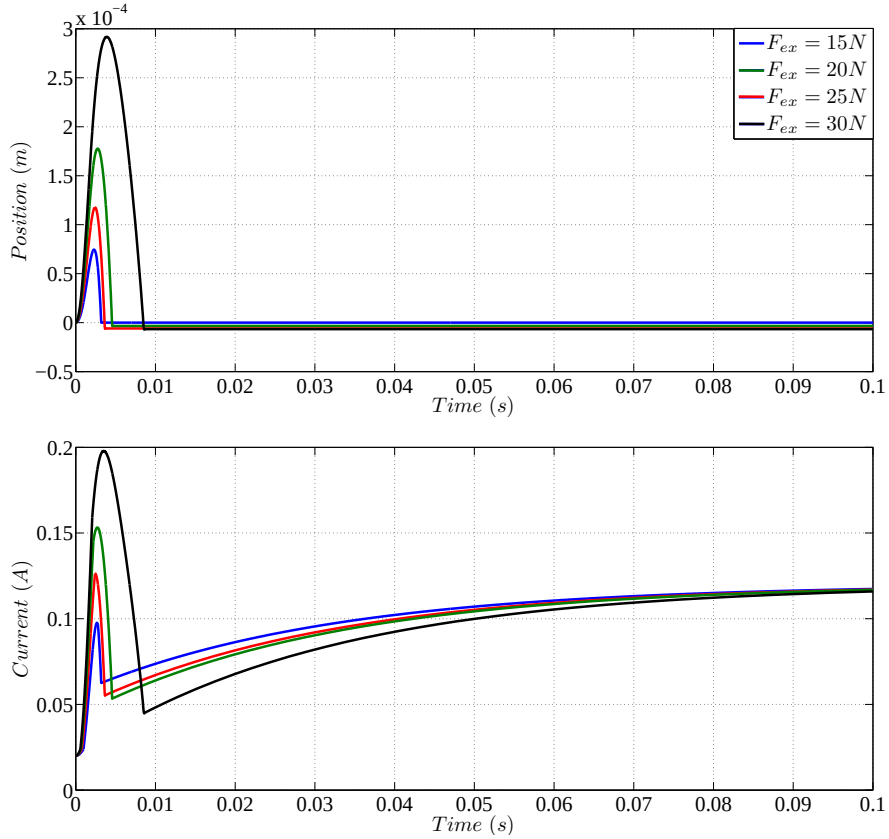


Fig. 5.29: Performance of the capacitor-based activation circuit for different external forces

where

$$E_1 = \frac{1}{2}L_c i_1^2 + \frac{1}{2}L^s i_2^2, \tag{5.66}$$

and

$$E_2 = \frac{1}{2}(L_c + L^s) i_a^2 \tag{5.67}$$

where $L_c$ is the inductance of the EM coil, $i_1$ is the stand-by current of the EM coil, $L^s$ is the supplementary inductor, $i_2$ is its stand-by current, and $i_a$ is the activation current after connection.

Incorporating (5.66) and (5.67) into (5.65) gives

$$i_a = (\frac{L_c i_1^2 + L^s i_2^2}{L_c + L^s})^{0.5}. \tag{5.68}$$

Assuming that the stand-by current of the EM coil is much smaller than that

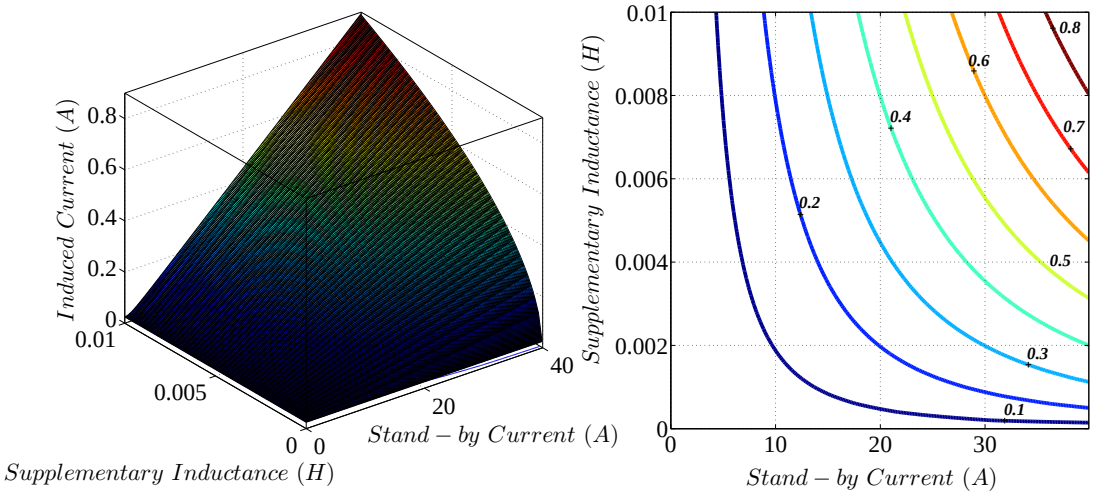


Fig. 5.30: Initial value of the activation current after connection

of the supplementary inductor, i.e. $i_1 << i_2$, (5.68) can be simplified as

$$i_a = (\frac{L^s}{L + L^s})^{0.5} i_2. \tag{5.69}$$

This equation shows that the initial value of the activation current is proportional to the stand-by current of the supplementary coil in the stand-by mode. Figure 5.30 shows how $L_s$ and $i_2$ affect the value of the activation current. In these simulations $L_c = 20\ H$ and (5.69) was modelled.

Figure 5.31 shows the schematic of the inductor-based closed-loop system. Figure 5.32 demonstrates the performance of such activation circuit for different external forces. The auxiliary inductor is $L^s = 0.1H$ and its stand-by current is $i_2 = 0.5A$ and the system parameters are as those is Table 5.4.

In inductor-based activation circuit, by connecting two inductors that carry different currents, an abrupt change in the current value occurs. This abrupt change is an idealistic hypothesis as it requires perfect switching from stand-by mode to activation mode and accurate synchronization of all switches. An ideal current ramp-up may not be achieved upon the application of inductor-based circuits. But this suggests that repetitive applications of this circuit for sequential current ramp-up can introduce a faster convergence to the nominal value. The process can be modelled by consecutively connecting different inductors with high currents to the

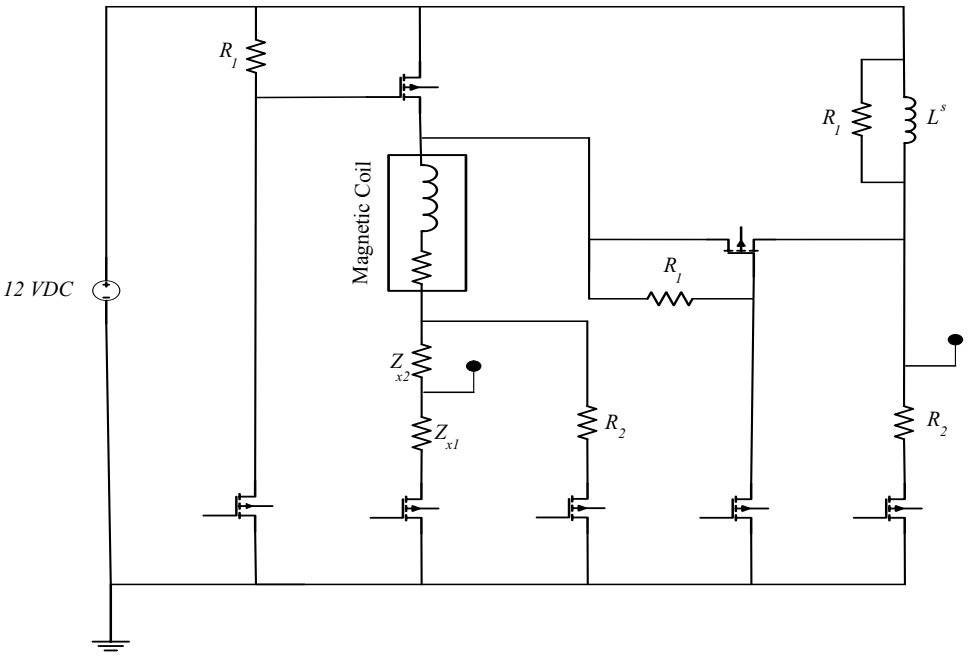


Fig. 5.31: Schematic of the inductor-based activation circuit

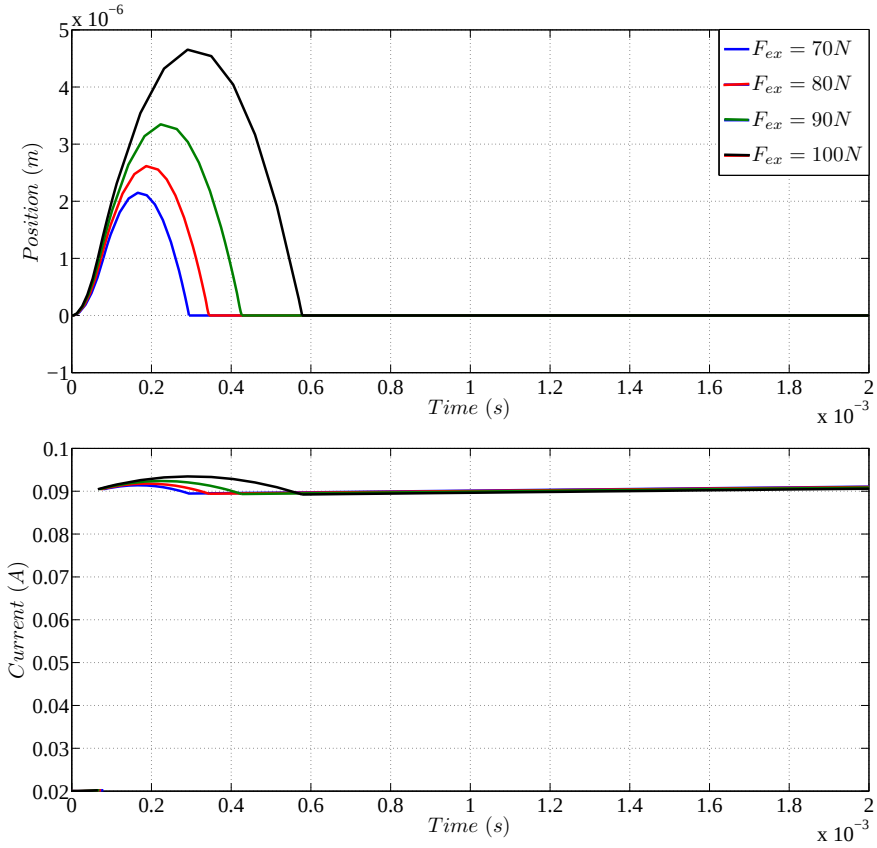


Fig. 5.32: Performance of the inductor-based activation circuit

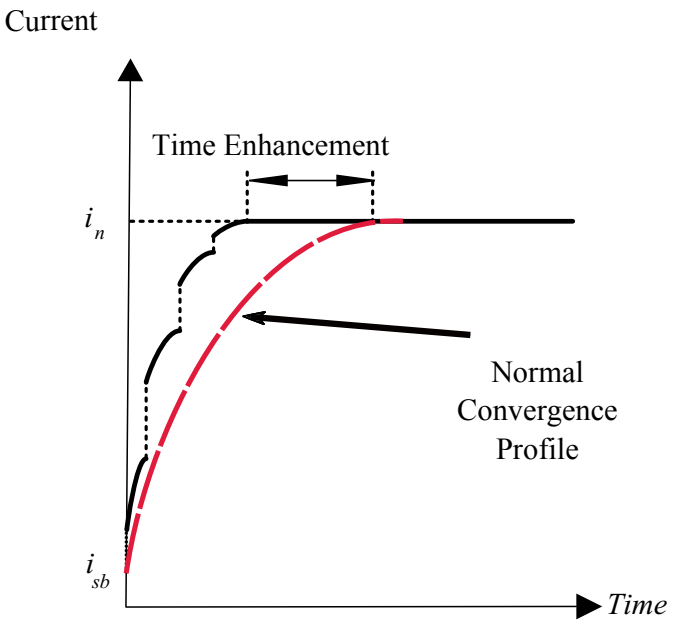


Fig. 5.33: Current ramp-up enhancement through sequential application of inductor-based circuit

coil. This increases the current through different steps. Therefore, the current convergence profile is constituted by a series of disconnected exponentially-increasing segments. Figure 5.33 illustrates a schematic of the corresponding current profile. By increasing the frequency of this process, the activation approaches the ideal case of abrupt current increase which minimizes the settling time of the system. This, in fact, is the basis of the design for DC-DC boost converters which is a modified version of the simple inductor-based circuit.

## 5.6 Conclusion

In this chapter, the dynamics of an EM system was analysed and the self-sensing capability of DC EM systems was assessed. The sensing signal was chosen as the voltage across the EM coil which experiences an abrupt reduction due to the induced voltage across the solenoid.

An optimized detection algorithm was also introduced which minimises the detection delay time. The corresponding formulation for generalized likelihood ratio method with a fixed-size sliding window was discussed and the effects of involving

parameters were investigated. Different activation circuits were also presented and their performance was discussed. Circuit layouts of the proposed control circuits and the pictures of the implemented circuits can be found in Appendix D.

# Chapter 6

# Experimental Validation

EM door locks are a relatively new DC device that have been used in recent years as a replacement for conventional locks in applications such as hospitals, laboratories, airport facilities, and large scale commercial or education buildings where complex security management and traffic control are often required [63]. Despite their increasing popularity, there is a potential issue in the operation of EM locks that gets recognized more and more recently [136]. When they operate in the fail-safe more (i.e. power is on for locking and off for releasing), they require continuous supply of electric power to remain locked. Although their power consumption is typically far less than that of conventional light bulbs, the power loss may not be negligible in long-term use if we leave them locked all the time. Keeping them activated continually with full power can be especially inefficient in doors that anyone hardly attempts to enter or exit. This chapter introduces energy-efficient EM locks by realizing the algorithms discussed in chapters 5 for a commercial lock produced by Rutherford Controls Int'l Corporation.

## 6.1 Operation and Control of Energy-efficient EM Locks

To approve the practicality of the discussed algorithms, the application of self-sensing to DC EM locking mechanisms is introduced here. An energy-efficient EM locking mechanism originates from the idea that cost-effective EM locks can

be realized by directly monitoring the change of inductance of the coil to detect any force initiated to open the door. The EM lock can then be operated in such a way that the full power is applied only when an attempt is made to gain an entry through the door; thereby allowing us to run the EM lock with a very low effective holding strength (and thus drawing very little current) most of the time. For this idea to work, two consecutive tasks must be completed within allowable time duration: the detection of an attempted entry and the activation of the EM to its full power. The allowable time duration for this system can be considered as the period short enough to pass the standard tests authorized by the Underwriters Laboratories (UL) [137] to be qualified as a burglary-resistant electric locking mechanism.

The self-sensing technique is recruited to use the existing EM coil and the armature plate not only as an actuator, but also as a sensing apparatus. Applications of self-sensing have been focused on measuring the position of the target (or the rotor) accurately [79, 81, 82]. This application is more concerned about the speed or the short-time behaviour of the inductance sensing during initiation of the armature movement. Timely-detection of the attempted entry through inductive sensing can be directly used to trigger the activation process that ramps the current up to the rated value as quickly as possible.

Figure 6.1 shows the EM block used for the experiments. The nominal current in the normal working condition for the uncontrolled system is $i_n = 220\ mA$ which rates the EM lock for $f_m = 1200\ lbf$ of holding force (system is rated for this value; but the actual force can be higher than 1200 $lbd$). Practically, the produced nominal magnetic force is significantly larger than $F_{ex}$ even for the most aggressive attempt to break in (i.e. $f_m >> F_{ex}$). The self-sensing mechanism is based on the idea of keeping the energy consumption of the system very low just enough to generate magnetic field for inductive sensing so that, most of the time, $f_m$ remains at much lower value than $F_{ex}$ (i.e. $f_m << F_{ex}$). The status of the EM lock running as an inductive sensor with $x = \dot{x} = 0$ is called the stand-by mode.

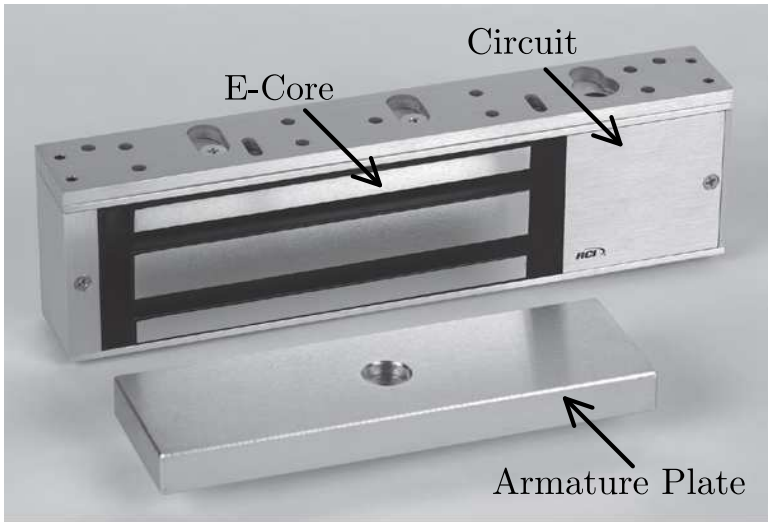


Fig. 6.1: A standard-size EM lock (Courtesy of *Rutherford Controls Int'l Corp.*)

The corresponding stationary value of the current across the coil will be called the stand-by current with its denotation $i_{sb}$. Likewise, the corresponding voltage across the coil will be called the stand-by voltage denoted by $V_{sb}$, i.e. $V_{sb} = R_c i_{sb}$.

## 6.2 Finite Element Analysis

Because in normal operation of DC EM locks the magnetic field is stationary, lamination of the conductor material is not needed. Also, for the simple manufacturing and production, the armature plate is usually a solid piece which is built by machining processes. This does not affect the normal operation of the system as eddy currents do not emerge in constant magnetic fields.

In energy-efficient EM locks, on the other hand, dynamics of the system produces eddy currents inside the conductor material. Therefore, equation (5.48) should be used for calculating the induced voltage. Calculating the nonlinear terms in this equation which are related to the eddy-current dynamics requires a sophisticated solution method that can couple the interaction of the structural movement of the system and the electromagnetic environment and their effects on the electronic variables such as sensing signal. Finite element method (FEM) in COMSOL Multiphysics modelling platform is used here to solve the problem of

electromagnetism on the macroscopic level. The basic electromagnetic problem on the macroscopic level is solving very well-known Maxwell's equations subject to appropriate boundary conditions.

### 6.2.1 Electromagnetic Model

The electromagnetic part of the model is governed by the following equations.

$$\nabla \times H = J \tag{6.1}$$

$$\nabla \times E = -\frac{\partial B}{\partial t} \tag{6.2}$$

$$\nabla . B = 0 \tag{6.3}$$

$$\nabla . J = 0 \tag{6.4}$$

where $H$ is the magnetic field density, $J$ is the current density, $E$ is the electric field intensity, and $B$ is the magnetic flux density. Equation (6.1) is the Maxwell-Ampére's law, (6.2) and (6.3) represent the Faraday's law and the Gauss's law, respectively, and (6.4) is the equation of continuity which is the field equivalent of Kirchhoff's current law. Maxwell's equations are solved along with the constitutive equations as follows.

$$B = \mu H \tag{6.5}$$

$$J = \sigma E \tag{6.6}$$

where $\mu$ is the permeability and $\sigma$ is the electric conductivity of the material. Incorporating (6.5) into (6.2), we get

$$\nabla \times E = -\mu \frac{\partial H}{\partial t}. \tag{6.7}$$

Multiplying both sides of this equation by $\sigma$ and using (6.6), we get

$$\nabla \times J = -\sigma\mu \frac{\partial H}{\partial t}. \tag{6.8}$$

Incorporating (6.1) into (6.8) yields

$$\nabla \times J = \nabla \times (\nabla \times H) = \nabla(\nabla . H) - \nabla^2 H = -\nabla^2 H, \tag{6.9}$$

since $\nabla.H = \frac{1}{\mu}\nabla.B = 0$.

Therefore (6.8) can be rewritten as

$$\nabla^2 H = \sigma\mu\frac{\partial H}{\partial t} \tag{6.10}$$

which is the diffusion equation and based on (6.5) is equivalent to

$$\nabla^2 B = \sigma\mu\frac{\partial B}{\partial t} \tag{6.11}$$

Also, for the magnetic flux inside the conductor material, (5.31) holds. Therefore, the solution to the diffusion equation yields $\phi_{eddy}$. Thus, to calculate the induced voltage, Maxwell's equations need to be solved first. In this paper, we use FEM to solve the equations. However, depending on the simplicity of the system, analytical solutions may be used to compute $\phi_{eddy}$, as well [138].

### 6.2.2 Structural Mechanics Model

The armature plate is the only part of the system which is modelled in the structural mechanics environment as it is the only moving part of the system. The magnetic force and the external force are the only effective forces which are applied to the armature during simulations.

Figure 6.2 shows the model and the mesh distribution, only half of which is considered in the simulation due to its symmetry.

Figure 6.3 shows some snapshots of the magnetic flux density streamlines for an open-loop performance of the system. In this simulation, the armature plate is solid (un-laminated) while the E-shaped core is laminated. Hence, the eddy-current effects affect the magnetic field inside the armature plate. Figure 6.3 illustrates how the magnetic field changes as the armature leaves the pole face. The transient behaviour of the EM and the armature can be seen more clearly from figures 6.3(b) and 6.3(c). The magnetic field in the EM gets weaker as the armature moves down. On the other hand, the induced magnetic field of the armature created by eddy currents gets stronger, especially, on the surface of the armature. The quantitative data resulting from this FEM analysis will be shown in the next section when they are compared with the experimental results.

## 6.3 Experimental Setups

Two sets of tests were conducted to evaluate the performance of the energy-efficient locking mechanism: lab tests and standard dynamic strength tests. The lab tests were performed to assess the self-sensing capability of the system and to approve the control strategy. The standard dynamic strength tests were performed to validate the safety of the proposed strategy against aggressive forces determined in standards [137].

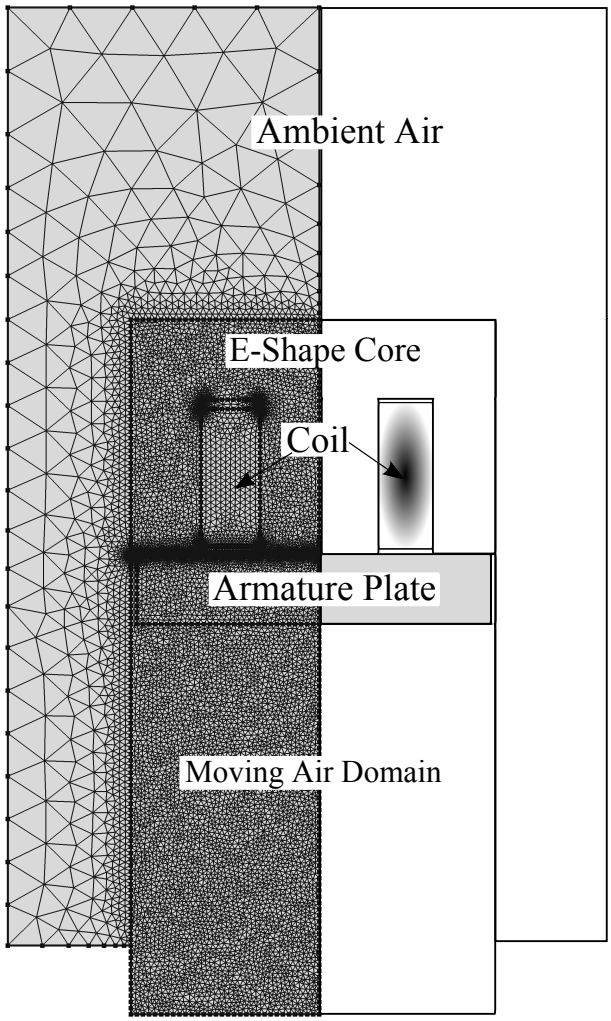


Fig. 6.2: Mesh distribution for the FEM analysis.

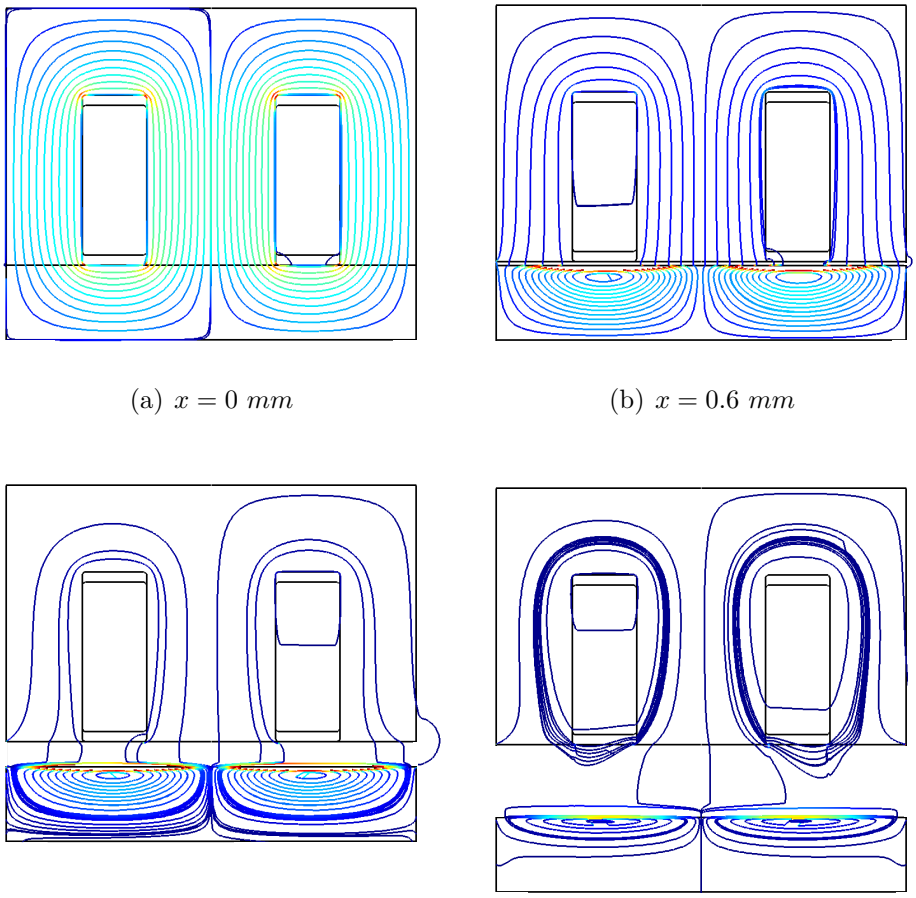

(a) $x = 0\ mm$ (b) $x = 0.6\ mm$

(c) $x = 3.8\ mm$ (d) $x = 10.8\ mm$

Fig. 6.3: Snapshots of magnetic field shape as the armature plate moves (uncontrolled system)

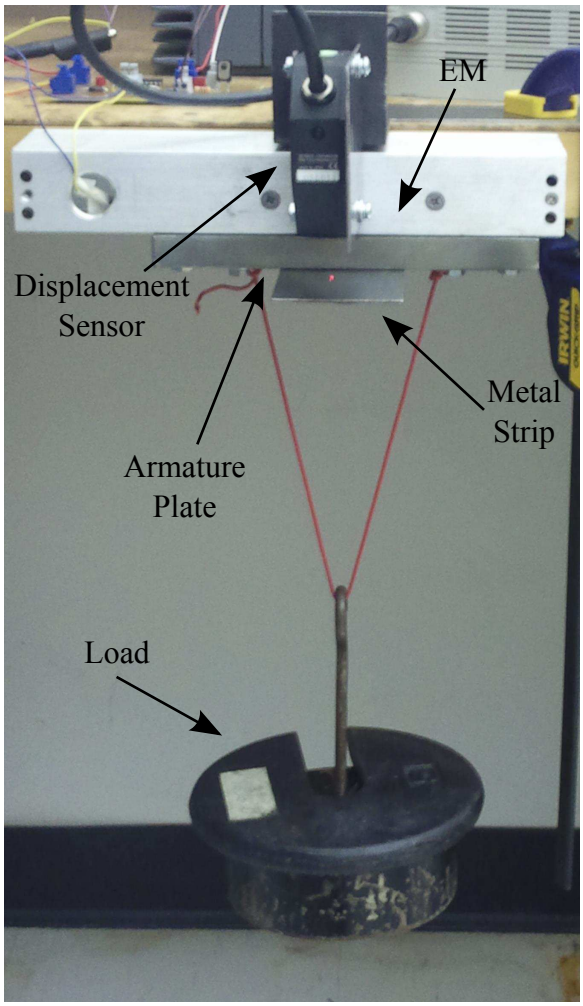


Fig. 6.4: The experimental setup for lab test

### 6.3.1 Lab Tests

Figure 6.4 shows the experimental setup for lab tests. A position sensor is used to measure the position of the armature plate as it leaves the pole face. A metal strip is attached to the armature as the target of the position sensor. The sensor used in the experiments is a laser sensor with $1\mu m$ repeatability. The experiment has been conducted by applying a force through putting weights on a platform connected to the armature (see figure 6.4).

Table 6.1 lists the parameter values of the system. The equivalent length of the magnetic flux within the core is obtained experimentally by setting $f_m = F_{ex}$ for some known $F_{ex}$ and then using (5.18) when $\ddot{x} = 0$. The supply voltage of $12.2V$

Table 6.1: Parameter values of a standard EM unit.

| Quantity | Symbol | Value |
|---|---|---|
| Supply Voltage | $V_{sup}$ | 12.2 $V$ |
| Mass of the armature | $m$ | 1.58 $kg$ |
| Number of winding turns | $N$ | 870 |
| Equivalent cross-section area | $A_{eq}$ | 0.0016 $m^2$ |
| Electrical resistance of the coil | $R_c$ | 54.5 $\Omega$ |
| Nominal current | $i_n$ | 220 $mA$ |
| Equivalent length of the core | $l$ | $6.11 \times 10^{-5}$ $m$ |

includes the voltage drop across the diode. The effective supply voltage after the diode is $11.6V$.

#### 6.3.1.1 Self-sensing Capability of EM Locks

Figure 6.5 compares the experimental data on the self-sensing capability of the EM lock with the corresponding simulation results. Upper plot shows the position of the armature $x$ as it falls down and the lower plot shows the sensing voltage $V_{sens}$. The sensing range of the position sensor was $10mm$. In both plots, the thick solid line represents the experimental results. For valid comparison of simulation data to the experimental results, we need to use the same profile for $F_{ex}$ in the simulations and experiments. Such $F_{ex}$ has been identified by comparing the simulated armature position with that from the experiment. The simulation results are obtained in two ways: the thin solid line is from the FEM analysis and the dotted line is from the mathematical analysis with $\dot{l} = 0$, i.e. no eddy current. The lower plot shows that the sensing voltage from the FEM matches closely to that of the experiments. The transient behaviour of $V_{sens}$ from the mathematical analysis is quite different from that of the experiment due to neglecting the effects of elec-

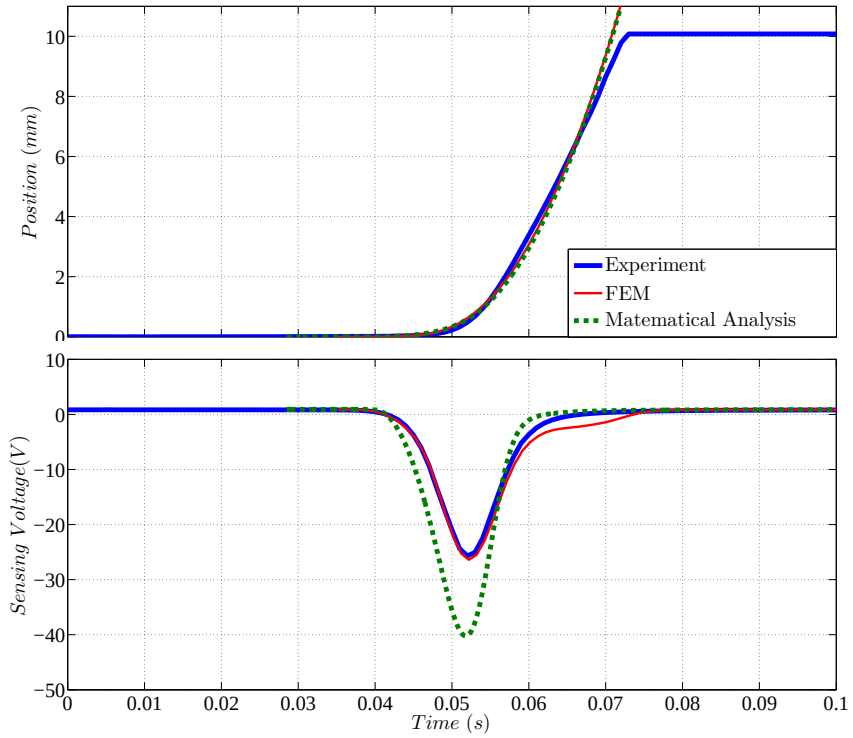


Fig. 6.5: Comparison of inductive sensing between simulations and experiment.

tromagnetic loss and leakage. This figure shows that the impending detachment of the armature can be recognized by detecting changes in the sensing voltage. Hence, self-sensing is feasible for this family of EM systems.

#### 6.3.1.2 Control Strategy Approval

As soon as a change is detected in the sensing voltage, we need to raise the magnetic force to recover the position of the armature as quickly as possible. Different activation circuits were introduced in chapter 5. As EM locks are designed to produce high values of magnetic force, their inductance is very large. Because of the high inductance of the system, the high-voltage activation is adopted for the experiments. Figure 6.6 demonstrates The schematic of the control circuit which is used in the experiments. A high-voltage source supplies the coil in the activation phase. A series of fast relays are used to connect/disconnect supply voltages to/from the system. The relays are operated through a real-time controller running on a PC at 1 $ms$ of sampling rate. The high voltage is connected to the

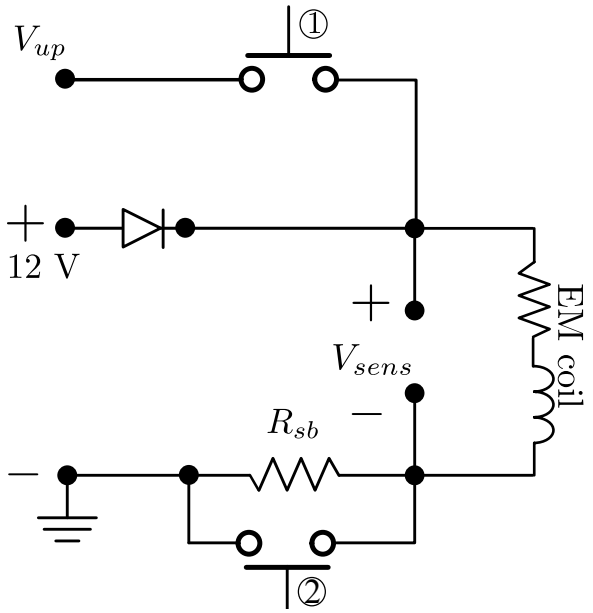


Fig. 6.6: Circuit schematic for high-voltage activation experiments

coil after detection and is disconnected after the current through the coil reaches a safe value. Therefore, the auxiliary high voltage supply is used only in a short period of time; hence, it does not affect the energy consumption of the system, noticeably. The reactive locking with current ramp-up has been tested with the experimental setup shown in figure 6.4. The high voltage during the experiments is a 95 $VDC$ produced by a DC-DC converter which is supplied by the nominal supply voltage of the system, $V_{sup} = 12.2\ V$. The stand-by current is $i_{sb} = 15\ mA$ and the safe value for current is selected to be $i_{safe} = 180\ mA$.

Figure 6.7 demonstrates the signals for a closed loop control of the system. For this experiment, the values of detection threshold is selected as $h = 50$ and the window size is $M = 20$. The noisy signals as well as the vibrations of the metal strip attached to the armature plate deteriorates the position profile. A smooth profile is fitted on the raw signal to estimate the actual position. Also, deflection of the testbed structure due to loading introduces a non-zero final value in the position profile. The position profile in figure 6.7 is compensated for the deflection of the testbed structure due to the loading. Due to the high magnetic force after activation, armature is pressed to the pole face; thereby, introducing

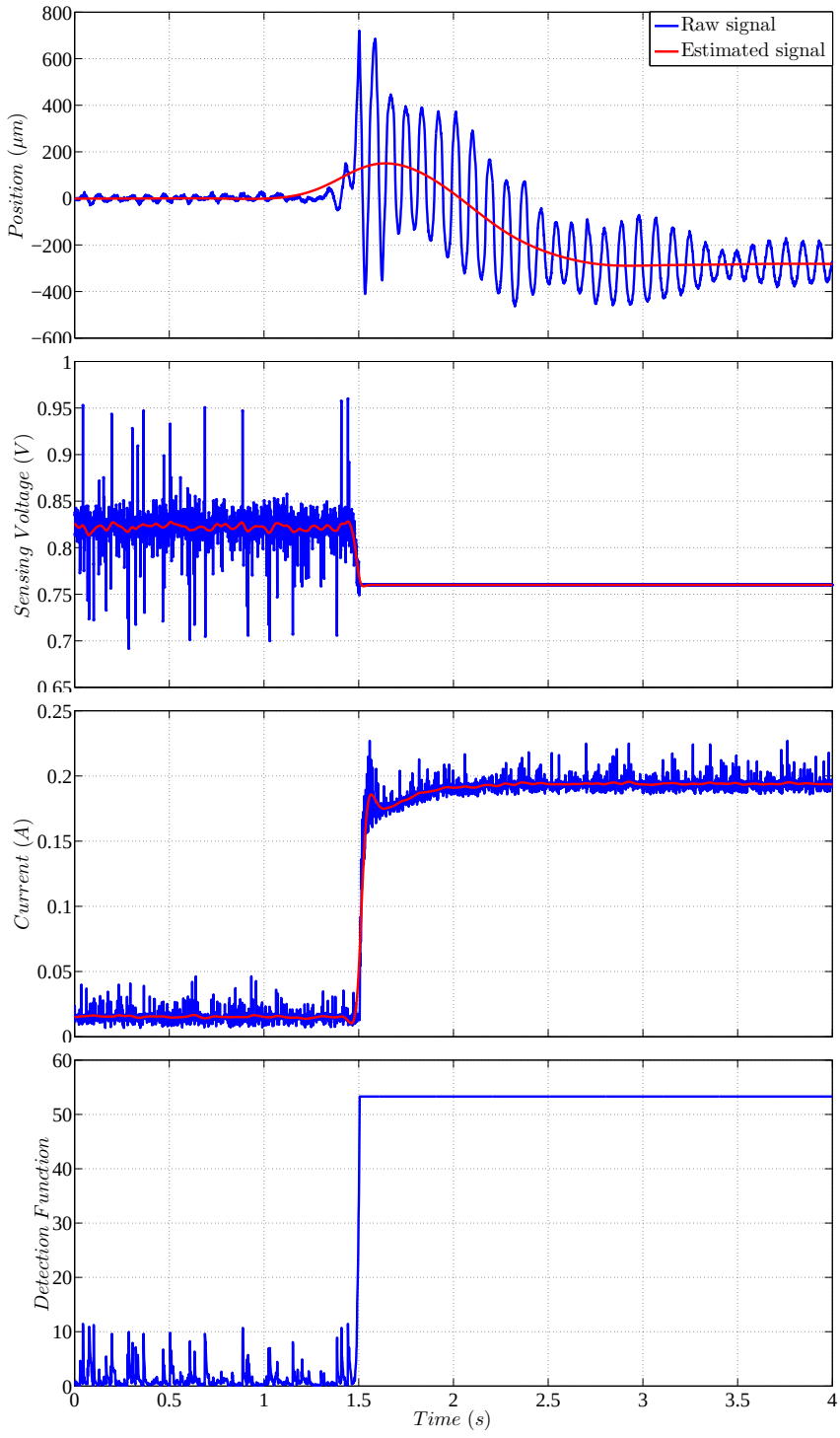


Fig. 6.7: Control strategy approval

negative values for the position of the armature.

A detailed view of the sensing voltage plot around the detection point is shown

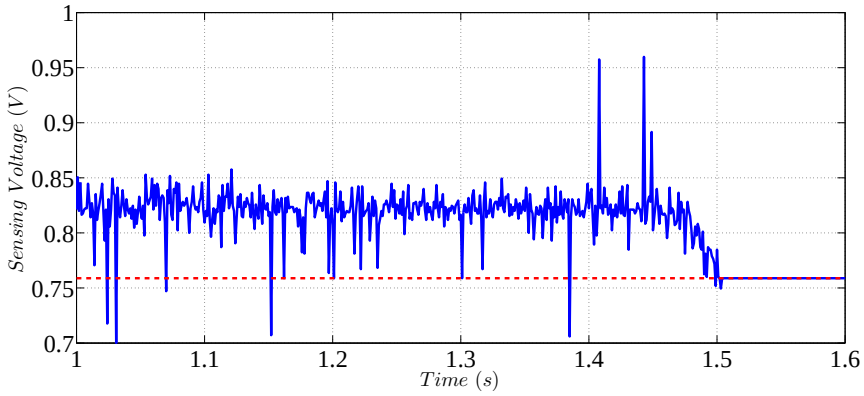


Fig. 6.8: Performance of detection mechanism

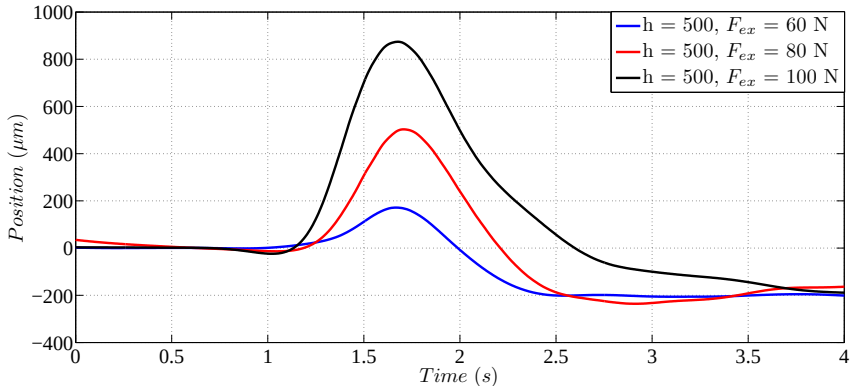


Fig. 6.9: Armature position for different external forces

in figure 6.8. The superior performance of the stochastic change detection mechanism compared with a threshold check can be observed in this figure. The sensing voltage experiences large drops due to the noise; but the adopted detection mechanism avoids false alarms by taking into account the stochastic nature of the signal at those times.

Figure 6.9 shows the recovery of the armature position for different external forces. This plot shows the estimated position by passing a smooth profile through the noisy raw signals as demonstrated in figure 6.7. This plot demonstrates how larger forces pull the armature further which increase the risk of a full detachment upon dull detection/activation. For satisfactory performance of the control process under the application of high external forces, larger stand-by currents are required. An example is provided in discussion of the dynamic tests.

### 6.3.2 Standard Dynamic Strength Tests

UL 1034 [137], entitled "Burglary-Resistant Electronic Locking Mechanisms," defines two standard procedures to certify an EM lock as a valid locking device against any burglary attempt: dynamic test and static test. The latter assesses the ultimate continuous holding strength of the system while the former tests the strength of the system to impact forces. The performance of the energy-efficient EM lock during static tests is the same as a fully-activated EM lock. However, dynamic tests require fast detection and activation of the system. The performance of cost-effective EM locks during standard dynamic strength tests is investigated in this section.

Figure 6.10 shows the UL 1034 testbed built by Rutherford Controls International Corporation. The ram with a spherical head which weighs 100 lb (45.4 kg) is to be suspended from four steel cables, with two attached to the front and the other two to the rear. The cables are attached in parallel to a fixed overhead beam, about 1.8 m above the centre line of the ram. A foamed polystyrene impact buffer (152 mm diameter by 51 mm thick) is to be secured to the test door at the impact point. The dynamic strength test is performed by pulling the ram back from its initial position by a certain horizontal distance and suddenly releasing it to apply an impact force against the door. The maximum dynamic rating which is 70 ft-lbf (90 J) corresponds to 35 in (889 mm) of the pull-back distance. The force profile during impacts in dynamic testing is a bell-shaped profile. Figure 6.11 compares this force profile for different impact energies, schematically. Increasing the impact energy results in raising the maximum value of the force while reducing the time duration of the force profile. Hence, for higher values of the impact energy, quicker responses of the control circuit are required. Based on experiments, the maximum force applied to the door and transferred to the EM lock is about 1400 $N$ which is equal to the produced magnetic force corresponding to 100 $mA$ current flowing through the coil.

The parameters for the dynamic strength test are listed in Table 6.2. A DC-DC

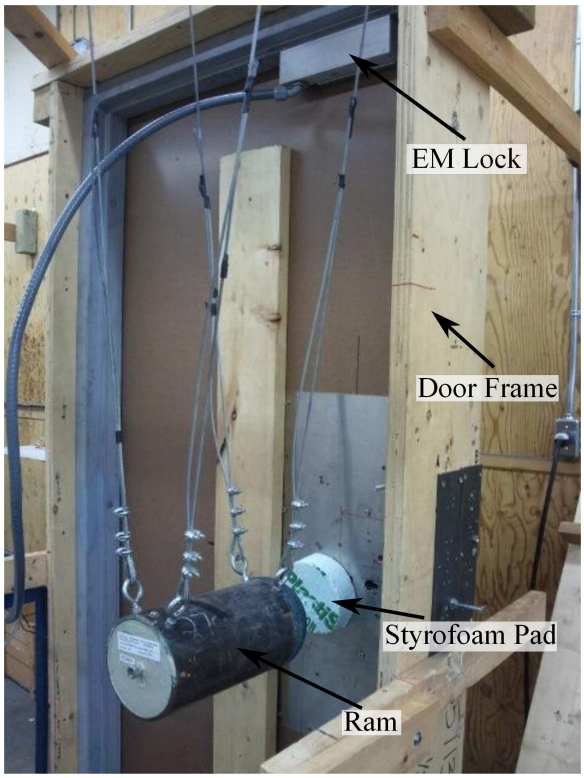


Fig. 6.10: Experimental setup for dynamic tests.

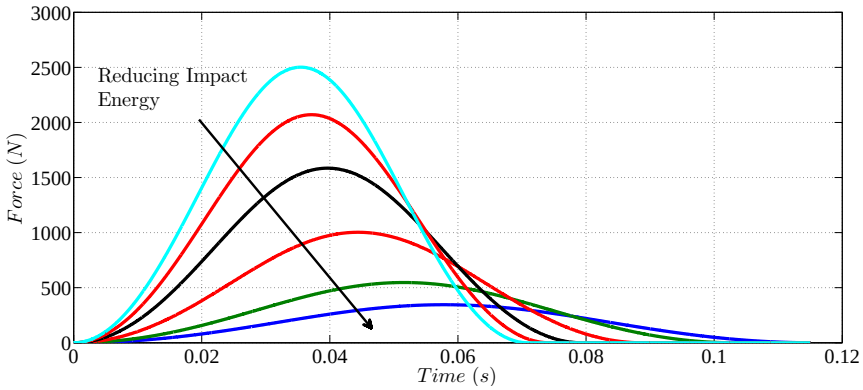


Fig. 6.11: Effect of reducing the impact energy on the force profile during dynamic strength tests.

Table 6.2: Parameter values for UL 1034 dynamic strength test.

| Quantity | Symbol | Value |
|---|---|---|
| Ramp-up voltage | $V_{up}$ | 95 $V$ |
| Stand-by voltage | $V_{sb}$ | $2.8 \sim 2.9$ $V$ |
| Stand-by current | $i_{sb}$ | $\cong 50$ $mA$ |
| Threshold voltage | $V_{th}$ | $\sim 120$ $mV$ below $V_{sb}$ |

converter is employed to create $V_{up} = 95V$. Different values of $i_{sb}$ have been tried to find the smallest stand-by current to achieve secure locking for the maximum dynamic strength rating. As a result, it has been found that about $i_{sb} = 50mA$ provides robust and secure locking for all the impact conditions. For implementation simplification as well as due to the low level of noise to signal ratio during the dynamic tests, a threshold check was used for detection.

The voltage threshold was chosen $V_{th} = 120$ $mV$ below the stand-by voltage. Figure 6.12 shows the experimental results with 35 in and 39 in pull-back distances which correspond to the impact forces beyond the maximum rating. Due to the limitations of dynamic tests, a position sensor was not installed on this testbed. The lower plot shows that it takes about $20ms$ for the current to reach the $i_n$ in case of the 35 in impact while it takes about $25ms$ for the 39 in impact. The difference between these two profiles is because higher impacts eventuate to larger gaps between armature plate and the pole face which correspond to further reduction in the inductance of the system (see (5.46)). Also, deflections of the testbed, vibrations in the system, and possible tilting angles in the armature plate which were due to its installation method might result in some discrepancies in the current profiles.

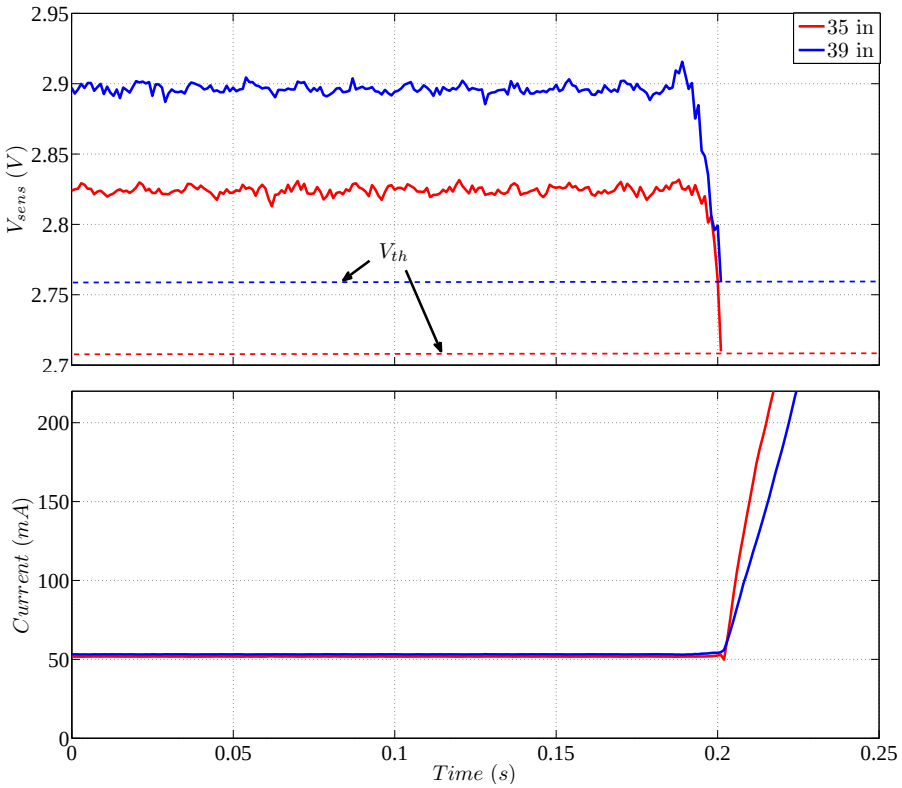


Fig. 6.12: Current ramp-up during dynamic strength tests.

## 6.4 Conclusion

This chapter introduced an application for realization of self-sensing capability of DC EM systems for energy conservation purposes. The method was applied to a family of EM locking mechanisms and could ensure the safe performance of the system during standard dynamic tests. The nominal current of the system $i_n = 220\ mA$ was reduced to a stand-by value of $i = 50\ mA$ which is about 23% of the nominal value. Therefore, more than 75% of the energy consumption of the system can be conserved through the application of the proposed method.

# Appendix A

# Proof of Theorem 2.1.3

Here, $H(q)$ is denoted briefly by $H$ and $S(q,\dot{q})$ is denoted by $S$. Regarding the closed-loop dynamic equation presented in (2.2) and calculating its inner product with $\{\dot{q}+C^{-1}KJ^T\Delta x\}^T$, we can get

$$\begin{aligned}&\{\dot{q}+C^{-1}KJ^T\Delta x\}^T H\ddot{q}+\frac{1}{2}\{\dot{q}+C^{-1}KJ^T\Delta x\}^T\dot{H}\dot{q}\\&+\{\dot{q}+C^{-1}KJ^T\Delta x\}^T S\dot{q}+\{\dot{q}+C^{-1}KJ^T\Delta x\}^T C\dot{q}\\&+\{\dot{q}+C^{-1}KJ^T\Delta x\}^T KJ^T\Delta x=0\end{aligned}\tag{A.1}$$

which can be rewritten as following

$$\begin{aligned}&\frac{d}{dt}[\{\frac{1}{2}(\dot{q}+KC^{-1}J^T\Delta x)^T H(\dot{q}+KC^{-1}J^T\Delta x)\}\\&+\frac{K}{2}\Delta x^T\{2I_m-KJC^{-1}HC^{-1}J^T\}\Delta x]\\&+\dot{q}^T C\dot{q}+K^2\Delta x^T JC^{-1}J^T\Delta x+Kh(\Delta x,\dot{q}(t))=0\end{aligned}\tag{A.2}$$

where $h(\Delta x,\dot{q})$ is defined as

$$h(\Delta x,\dot{q})=\Delta x^T JC^{-1}(-\frac{1}{2}\dot{H}-S)\dot{q}-\Delta x^T\dot{J}C^{-1}H\dot{q}-\dot{q}^T J^T JC^{-1}H\dot{q},\tag{A.3}$$

and $I_m$ is the $m\times m$ identity matrix.

By defining

$$\begin{aligned}W(K;\Delta x,\dot{q})=&\frac{1}{2}(\dot{q}+KC^{-1}J^T\Delta x)^T H(\dot{q}+KC^{-1}J^T\Delta x)\\&+\frac{K}{2}\Delta x^T\{2I_m-KJC^{-1}HC^{-1}J^T\}\Delta x,\end{aligned}\tag{A.4}$$

we can get the time derivative of $W(K;\Delta x,\dot{q})$ by using (A.2) as followed.

$$\begin{aligned}\frac{d}{dt}W(K;\Delta x,\dot{q}) &= -\dot{q}^T C\dot{q} - K^2\Delta x^T JC^{-1}J^T\Delta x - Kh(\Delta x,\dot{q}(t)) \\ &\leq -\gamma W(K;\Delta x,\dot{q}) - Kh(\Delta x,\dot{q}(t)) - f(K;\Delta x,\dot{q})\end{aligned} \tag{A.5}$$

where $\gamma$ is a positive parameter and

$$\begin{aligned}f(K;\Delta x,\dot{q}) &= \dot{q}^T(C - \frac{\gamma}{2}H - \frac{\gamma K}{4}H)\dot{q} \\ &\quad + K\Delta x^T(KJC^{-1}J^T - \gamma I_m - \gamma JC^{-1}HC^{-1}J^T)\Delta x.\end{aligned} \tag{A.6}$$

If we justify that

$$Kh(\Delta x,\dot{q}(t)) + f(K;\Delta x,\dot{q}) \geq 0,\ for\ all\ t \geq 0, \tag{A.7}$$

then, considering (A.5), we can write

$$\frac{d}{dt}W(K;\Delta x,\dot{q}) \leq -\gamma W(K;\Delta x,\dot{q}) \tag{A.8}$$

which gives

$$\begin{aligned}W(K;\Delta x,\dot{q}) &\leq e^{-\gamma t}W(K;\Delta x(0),\dot{q}(0)) \\ &\leq e^{-\gamma t}K||\Delta x(0)||^2.\end{aligned} \tag{A.9}$$

In (A.9), we supposed that the system starts from still conditions at the beginning of the movement, i.e. $\dot{q}_i(0) = 0\ for\ i = 1,2,...,n$. This hypothesis is reasonable in the case of human-skilled multi-joint reaching in a regulation problem. Furthermore, (A.4) gives

$$W(K;\Delta x,\dot{q}) \geq \frac{K}{2}\Delta x^T\{2I_m - KJC^{-1}HC^{-1}J^T\}\Delta x. \tag{A.10}$$

Now, if there exist $a,b > 0$ such that $bI_m \leq \{2I_m - KJC^{-1}HC^{-1}J^T\} \leq aI_m$, (A.10) gives

$$W(K;\Delta x,\dot{q}) \geq \frac{bK}{2}||\Delta x||^2. \tag{A.11}$$

Based on equations (A.9) and (A.11), we can write

$$\begin{aligned}\frac{bK}{2}||\Delta x||^2 \leq e^{-\gamma t}K||\Delta x(0)||^2 \Rightarrow \\ ||\Delta x||^2 \leq \frac{2}{b}e^{-\gamma t}||\Delta x(0)||^2.\end{aligned} \tag{A.12}$$

Equation (A.12) indicates the exponential convergence to the target point.

Afterwards, integrating the closed-loop dynamics of the system in (2.2) gives

$$C(q(t)-q(0)) = -H(q(t))\dot{q}(t) + H(q(0))\dot{q}(0) + \int_0^t (\frac{1}{2}\dot{H} - S)\dot{q}d\tau - K\int_0^t J^T \Delta x d\tau, \tag{A.13}$$

and taking the norm of both sides of (A.13) gives

$$\begin{aligned} ||C(q(t)-q(0))|| \leq & ||H(q(t))\dot{q}(t)|| + ||H(q(0))\dot{q}(0)|| + ||\int_0^t (\frac{1}{2}\dot{H} - S)\dot{q}d\tau|| \\ & + ||K\int_0^t J^T \Delta x d\tau||. \end{aligned} \tag{A.14}$$

Furthermore, considering the kinematic energy of the system we have

$$K(t) = \frac{1}{2}\dot{q}(t)^T H \dot{q}(t) \geq \frac{\lambda_1}{2}||\dot{q}(t)^T I_n \dot{q}(t)|| = \frac{\lambda_1}{2}||\dot{q}(t)||^2 \tag{A.15}$$

in which $\lambda_1$ is the smallest eigenvalue of the inertia matrix for all values of link angles, and $I_n$ is the $n \times n$ identity matrix. Therefore, we can write

$$\sqrt{K(t)} \geq \sqrt{\frac{\lambda_1}{2}}||\dot{q}(t)|| \Rightarrow \lambda_2\sqrt{\frac{2}{\lambda_1}}\sqrt{K(t)} \geq \lambda_2||\dot{q}(t)|| \tag{A.16}$$

where $\lambda_2$ is the largest eigenvalue of the inertia matrix for all values of link angles, i.e.

$$\lambda_1 I_n \leq H(q(t)) \leq \lambda_2 I_n. \tag{A.17}$$

Regarding (A.17), we can write

$$||H(q(t))\dot{q}(t)|| \leq \lambda_2||\dot{q}(t)||. \tag{A.18}$$

Equations (A.15) and (A.18) give

$$||H(q(t))\dot{q}(t)|| + ||H(q(0))\dot{q}(0)|| \leq \lambda_2\sqrt{\frac{2}{\lambda_1}}(\sqrt{K(t)} + \sqrt{K(0)}) \tag{A.19}$$

In the third term, the expressions inside the integral are of order of two with respect to $\dot{q}(t)$ as $(\frac{1}{2}\dot{H} - S)$ has terms containing $\dot{q}(t)$. Therefore, we can find a positive scalar, $\beta$, for which

$$||\frac{1}{2}\dot{H} - S|| \leq \beta||C\dot{q}(t)|| \tag{A.20}$$

where $C$ is the damping matrix. Hence,

$$||\int_0^t (\frac{1}{2}\dot{H} - S)\dot{q}(t)d\tau|| \leq ||\beta \int_0^t \dot{q}(t)^T C\dot{q}(t)d\tau|| = \beta \int_0^t \dot{q}(t)^T C\dot{q}(t)d\tau \tag{A.21}$$

Also, a positive constant, $\alpha$, can be found such that

$$-\alpha I_m \leq JJ^T \leq \alpha I_m. \tag{A.22}$$

Therefore, for the last term in (A.13), we can write

$$||K \int_0^t J^T \Delta x d\tau|| \leq K\sqrt{\alpha} \int_0^t ||\Delta x|| d\tau. \tag{A.23}$$

Finally, substituting (A.12) into (A.23) and calculating the integral, results in

$$||K \int_0^t J^T \Delta x d\tau|| \leq K\gamma\sqrt{\frac{\alpha}{2b}}||\Delta x(0)||. \tag{A.24}$$

Consequently, collaborating (A.19), (A.21) and (A.24) into (A.14), we can get

$$\begin{aligned} ||C(q(t) - q(0))|| \leq & \lambda_2\sqrt{\frac{2}{\lambda_1}}(\sqrt{K(t)} + \sqrt{K(0)}) + K\gamma\sqrt{\frac{\alpha}{2b}}||\Delta x(0)|| \\ & + \beta \int_0^t \dot{q}(t)^T C\dot{q}(t)d\tau. \end{aligned} \tag{A.25}$$

Furthermore, based on (2.4), we can say

$$\frac{d}{dt}E = -\dot{q}^T C\dot{q} \Rightarrow \int_0^t \dot{q}^T C\dot{q}d\tau = E(0) - E(t) \geq 0, \tag{A.26}$$

and based on definition of energy, it can be written that

$$\begin{aligned} K(t) \leq E(t) \leq E(0) \\ K(0) \leq E(0). \end{aligned} \tag{A.27}$$

Thus, (A.25) can be simplified as following

$$||C(q(t) - q(0))|| \leq 2\lambda_2\sqrt{\frac{2}{\lambda_1}}\sqrt{E(0)} + K\gamma\sqrt{\frac{\alpha}{2b}}||\Delta x(0)|| + \beta E(0). \tag{A.28}$$

Also, considering the definition of $E$, we can write

$$||\Delta x(0)|| \leq \sqrt{\frac{2}{K}E(0)}. \tag{A.29}$$

Thereby, (A.28) gives

$$||C(q(t) - q(0))|| \leq (2\lambda_2\sqrt{\frac{2}{\lambda_1}} + \gamma\sqrt{\frac{\alpha}{bK}})\sqrt{E(0)} + \beta E(0). \tag{A.30}$$

Furthermore, as defined before, we have

$$\begin{aligned} ||q(t) - q(0)||_k &= \sqrt{\frac{1}{2}(q(t) - q(0))^T H(q)(q(t) - q(0))} \\ &\leq \frac{\sqrt{\lambda_2}}{c_{min}}\sqrt{\frac{1}{2}(q(t) - q(0))^T C^T C(q(t) - q(0))} \\ &\leq \frac{\sqrt{\lambda_2}}{c_{min}\sqrt{2}}||C(q(t) - q(0))|| \end{aligned} \tag{A.31}$$

where, $c_{min} = min\{C(i,i)\}, i = 1, 2, ..., n$. Thus,

$$||q(t) - q(0)||_k \leq \frac{\sqrt{\lambda_2}}{c_{min}\sqrt{2}}[(2\lambda_2\sqrt{\frac{2}{\lambda_1}} + \gamma\sqrt{\frac{\alpha}{bK}})\sqrt{E(0)} + \beta E(0)]. \tag{A.32}$$

For an arbitrary given $\varepsilon > 0$ denote the solution $(q(t), \dot{q}(t))$ starting from $(q(0), \dot{q}(0))$ lying in $N^{2n}(\delta(\varepsilon), r_1)$, i.e. $E(0) \leq \delta^2$. Therefore, using (A.32), we can write

$$\begin{aligned} ||q(t) - q^0||_k &\leq ||q(0) - q^0||_k + ||q(t) - q(0)||_k \\ &\leq r_1 + \frac{\sqrt{\lambda_2}}{c_{min}\sqrt{2}}[(2\lambda_2\sqrt{\frac{2}{\lambda_1}} + \gamma\sqrt{\frac{\alpha}{bK}})\delta + \beta\delta^2]. \end{aligned} \tag{A.33}$$

If we choose

$$\delta = min\{\frac{\sqrt{B^2 - 4AC} - B}{2A}, \varepsilon, \delta_1\} \tag{A.34}$$

where, $A = \beta$, $B = 2\lambda_2\sqrt{\frac{2}{\lambda_1}} + \gamma\sqrt{\frac{\alpha}{bK}}$ and $C = c_{min}\sqrt{\frac{2}{\lambda_2}}(r_0 - r_1)$, we can get

$$||q(t) - q^0||_k \leq r_0.$$

Thus, the stability on the manifold is proven as the solution remains in $N^{2n}(\varepsilon, r_0)$ for all future time.

# Appendix B

# Parameter $\gamma$ in Convergence Conditions of Jacobian Transpose Controller

In this section, we analyse equation 2.8, briefly. For reference convenience, this equation is repeated here

$$Kh(\Delta x, \dot{q}(t)) + f(K; \Delta x, \dot{q}(t)) \geq 0. \tag{B.1}$$

where $K$ is the stiffness coefficient, and $h(\Delta x, \dot{q})$ and $f(K; \Delta x, \dot{q}(t))$ are as follows.

$$h(\Delta x, \dot{q}) = \Delta x^T J C^{-1}(-\frac{1}{2}\dot{H} - S)\dot{q} - \Delta x^T \dot{J} C^{-1} H \dot{q} - \dot{q}^T J^T J C^{-1} H \dot{q} \tag{B.2}$$

$$\begin{aligned} f(K; \Delta x, \dot{q}) = \dot{q}^T (C - \frac{\gamma}{2}H - \frac{\gamma K}{4}H)\dot{q} \\ + K\Delta x^T (K J C^{-1} J^T - \gamma I_m - \gamma J C^{-1} H C^{-1} J^T)\Delta x \end{aligned} \tag{B.3}$$

Considering equations A.17, A.22, and 2.9, by simplifying equation B.1, we can get:

$$\begin{aligned} Kh(\Delta x, \dot{q}(t)) + f(K; \Delta x, \dot{q}(t)) \geq K\Delta x^T \{J C^{-1}(-\frac{1}{2}\dot{H} - S) - \dot{J} C^{-1} H\}\dot{q} \\ + \dot{q}^T \{C - (\frac{\gamma}{2} + \frac{K\gamma}{4} + K\alpha c_{max})\lambda_2 I_n\}\dot{q} \\ + K\Delta x^T (K c_{min} J J^T + \gamma I_m)\Delta x \end{aligned} \tag{B.4}$$

As can be seen, the value of $\gamma$ affects on the value of the second and the third term. Thus, for a reasonable set of control parameters, this value can be calculated to assure the positivity of the left hand side of equation B.1.

Based on equation A.12, the value of $\gamma$ is a milestone of the speed of convergence to the target point. However, as long as it holds $\gamma \geq 0$ the convergence is guaranteed.

# Appendix C

# Distance of the End-effector to the Straight Line

Fig. C.1 shows the initial and an intermediate configuration of a robot manipulator during a reaching task. The initial position of the end-effector is denoted by $P_0$, the current position is $P$, and the desired position is $P_d$. The line connecting the initial and desired points is called $L_1$ and the perpendicular line to this line that passes through the end-effector is denoted by $L_2$ (see Fig. C.1). The position of the intersection of these two lines is denoted by $P_{dn}$.

The slope of $L_1$ can be computed as

$$m = \frac{P_d^2 - P_0^2}{P_d^1 - P_0^1} \tag{C.1}$$

where the super script 1 indicates the $x$ component and 2 indicates the $y$ component of the positions.

The line $L_1$ can be defined as

$$L_1 : \; Y = m(X - P_0^1) + P_0^2 \tag{C.2}$$

where $X$ and $Y$ are the $x$ and $y$ components of the position vector of the points lying on this line.

The slope of $L_2$ is

$$m' = -\frac{1}{m} \tag{C.3}$$

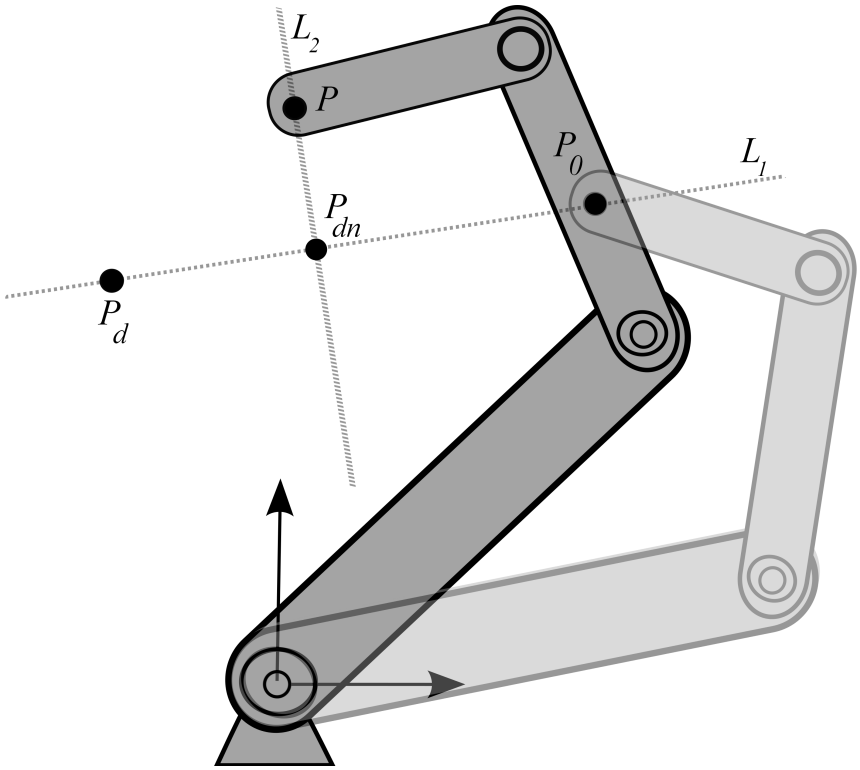


Fig. C.1: The straight line connecting the initial and target points

Therefore, the equation of $L_2$ becomes

$$L_2 : \; Y = m'(X - P_0^1) + P_0^2 \tag{C.4}$$

$P_{dn}$ is the intersection of $L_1$ and $L_2$. Equating (C.2) and (C.4) after some simplifications gives

$$\begin{aligned} P_{dn}^1 &= \frac{-m}{1+m^2}(P_0^2 - P^2 - mP_0^1 - \frac{1}{m}P^1) \\ P_{dn}^2 &= m(P_{dn}^1 - P_0^1) + P_0^2 \end{aligned} \tag{C.5}$$

The vector from the end-effector to the intersection point becomes

$$\Delta P = \begin{bmatrix} P_{dn}^1 - P^1 \\ P_{dn}^2 - P^2 \end{bmatrix} \tag{C.6}$$

and the distance from the end-effector to the straight line is the length of this vector, i.e. $||\Delta P||$.

# Appendix D

# Electronic Circuit Layouts

## D.1 High-voltage Activation Circuits

### D.1.1 Circuit With Dedicated Voltage Converter

#### D.1.1.1 Circuit 1

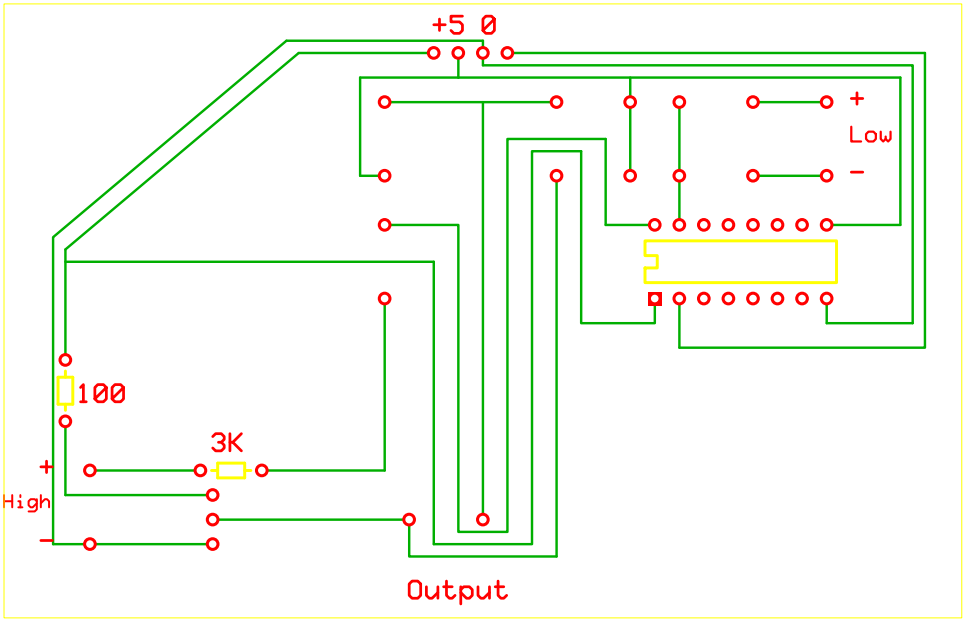

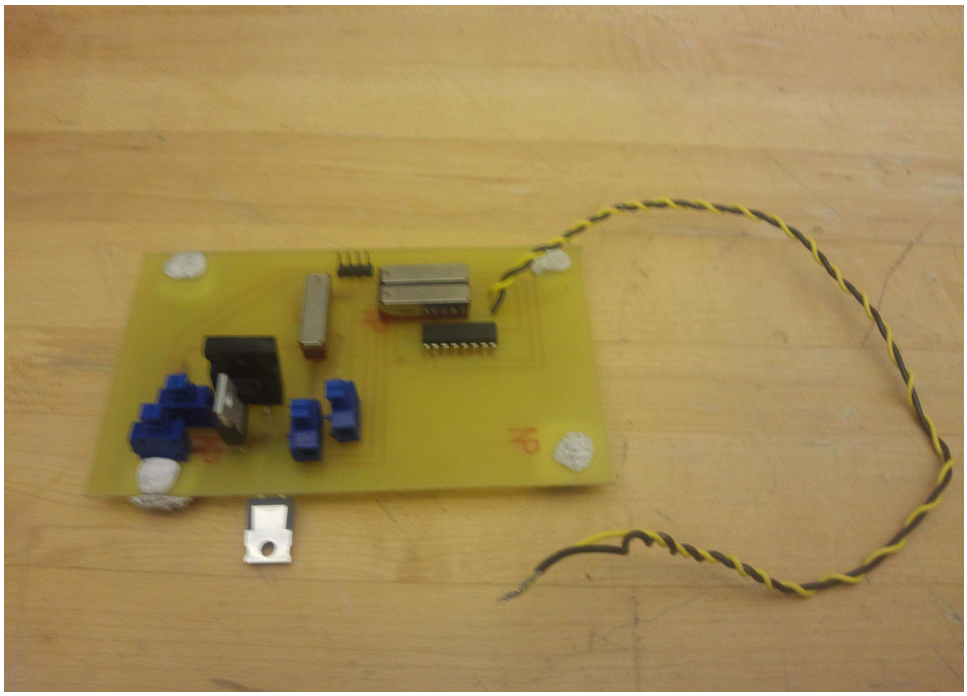

#### D.1.1.2 Circuit 2

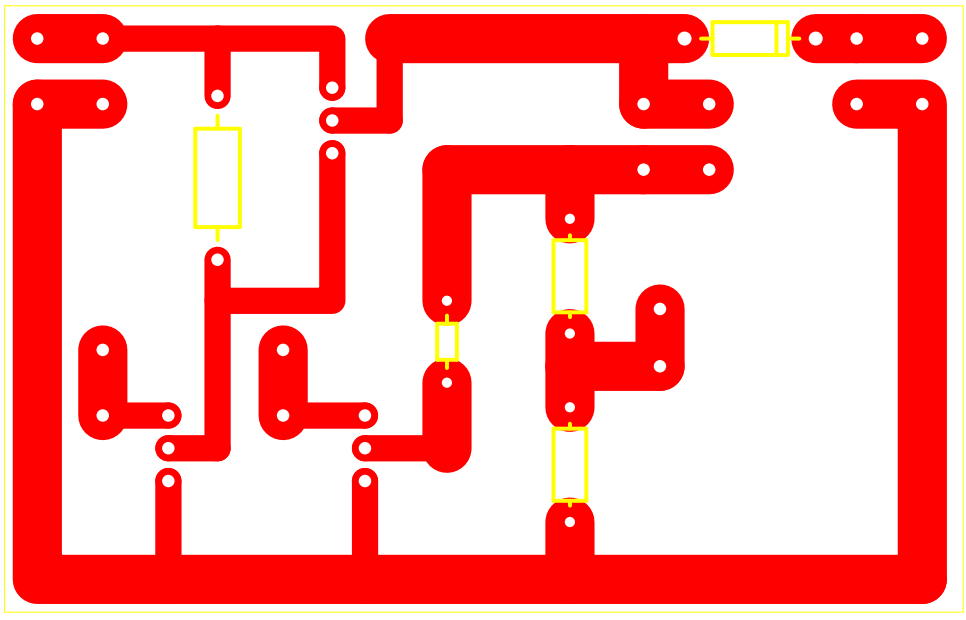

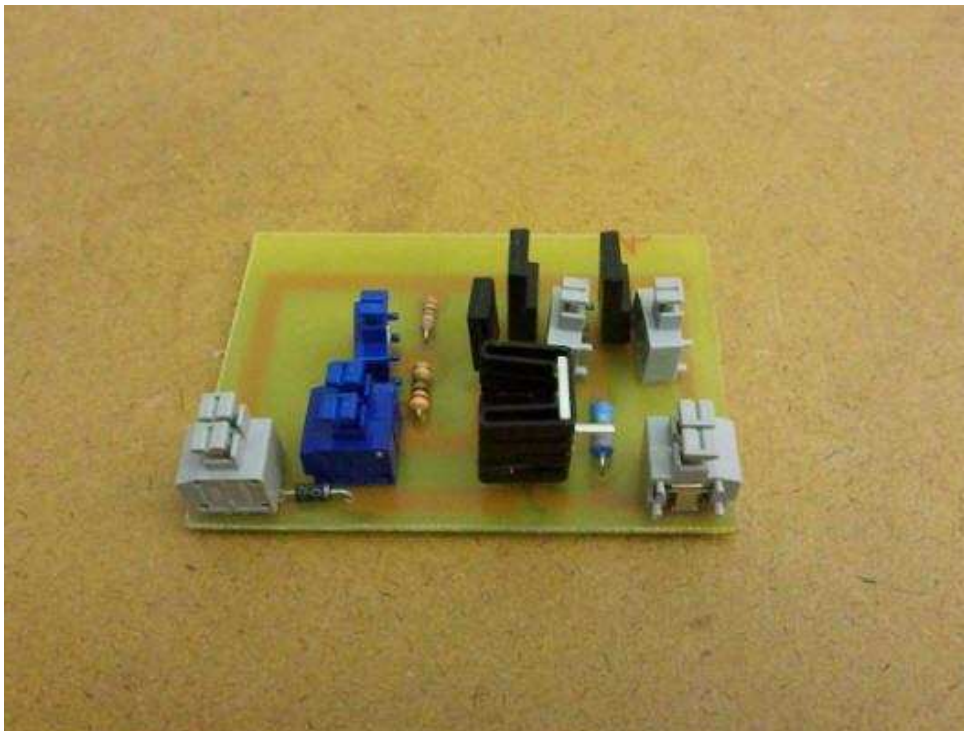

### D.1.1.3 Circuit 3

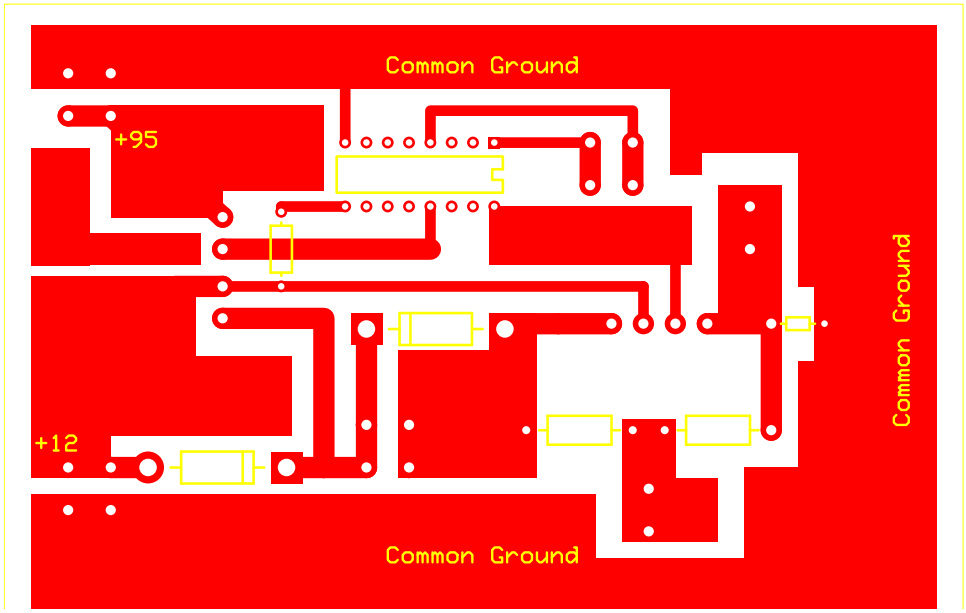

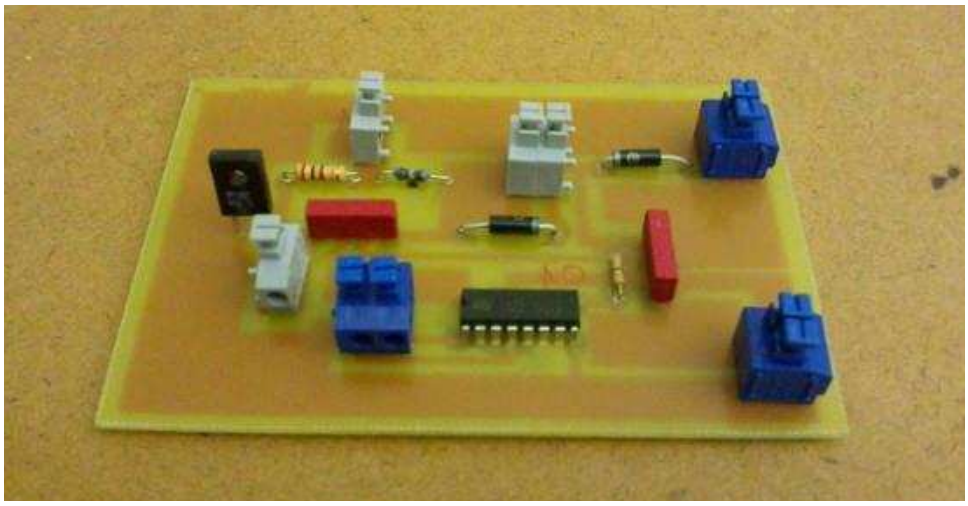

### D.1.2 Circuit With Integrated Voltage Converter

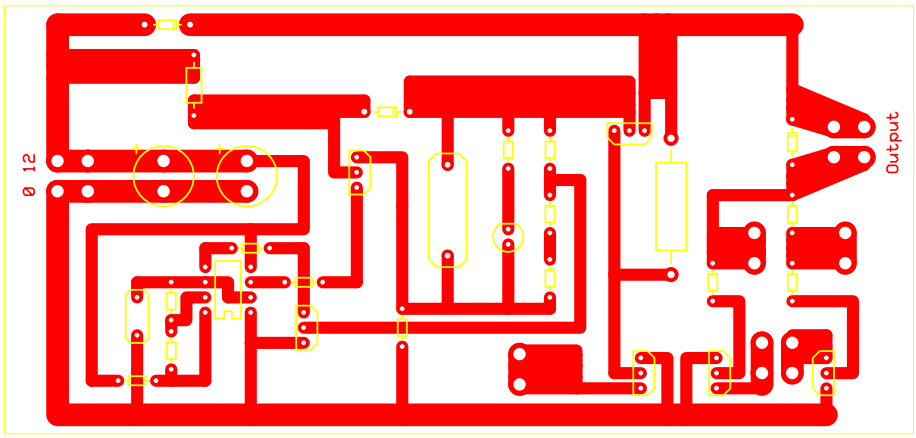


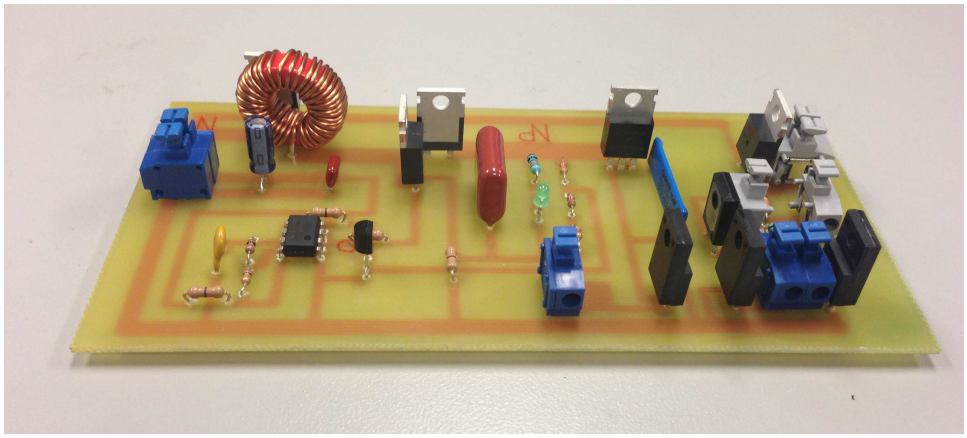

## D.2 Capacitor-based Activation Circuit

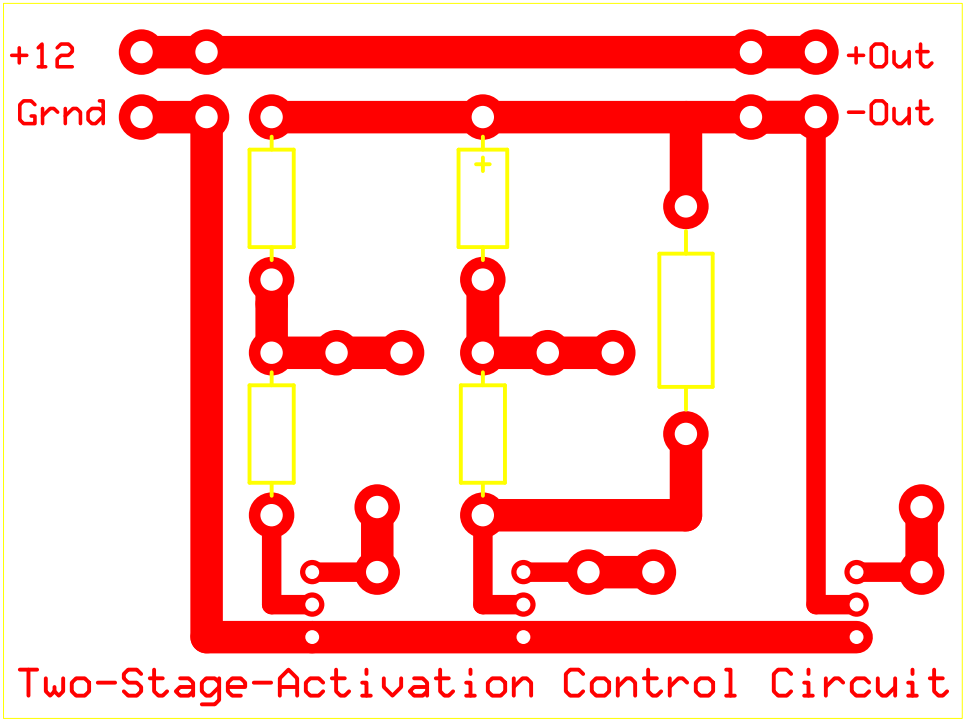


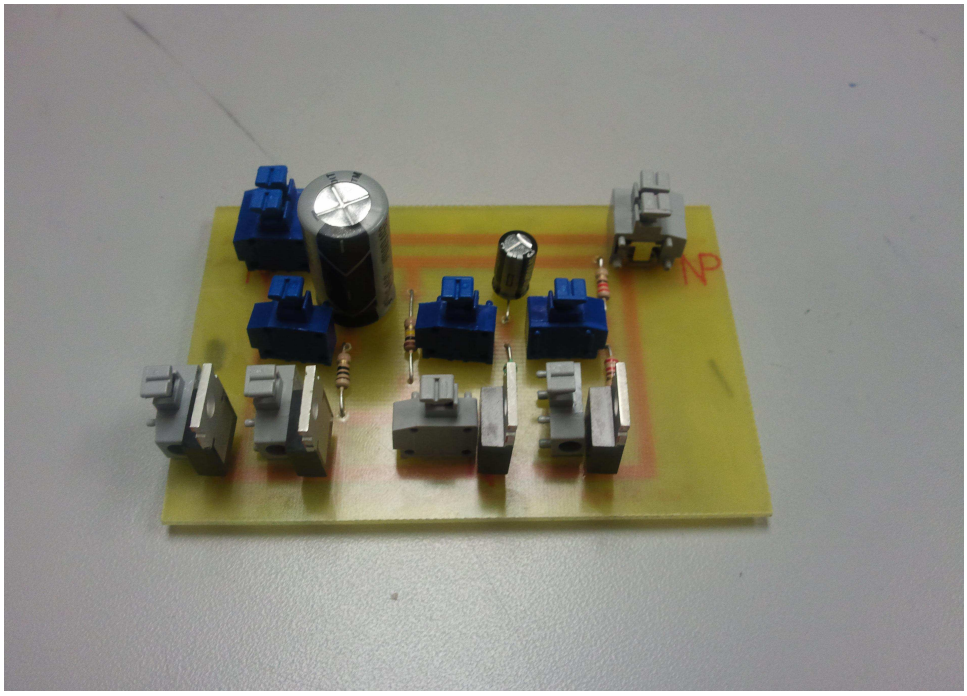

## D.3 Inductor-based Activation Circuit

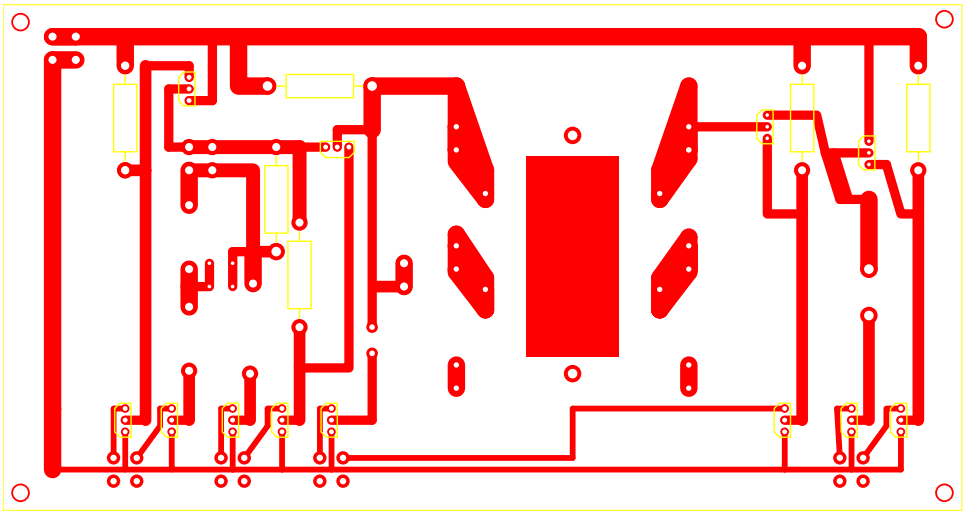

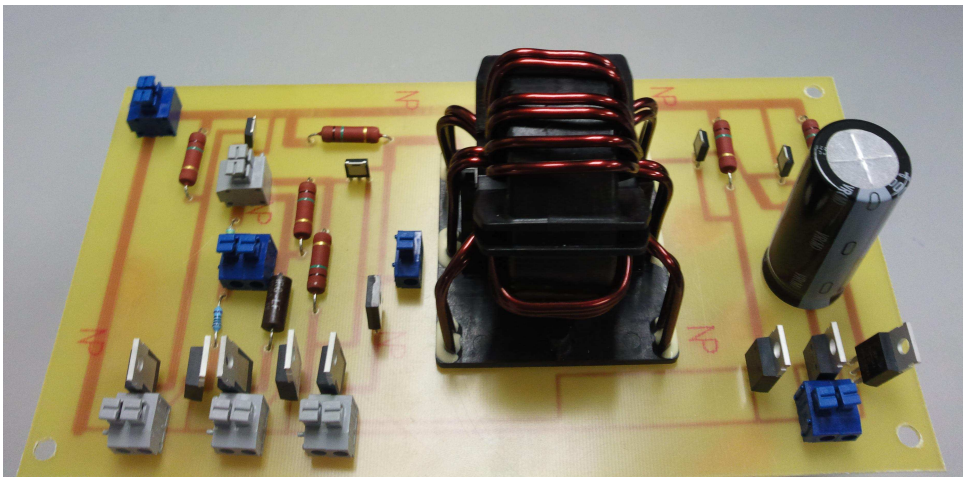

# Chapter 7

# References


[1] J. P. Scholz and G. Schöner, "The uncontrolled manifold concept: identifying control variables for a functional task," *Experimental brain research*, vol. 126, no. 3, pp. 289–306, 1999.

[2] M. L. Latash and J. G. Anson, "Synergies in health and disease: relations to adaptive changes in motor coordination," *Physical therapy*, vol. 86, no. 8, pp. 1151–1160, 2006.

[3] J. W. Burdick, "On the inverse kinematics of redundant manipulators: Characterization of the self-motion manifolds," in *Advanced Robotics: 1989*. Springer, 1989, pp. 25–34.

[4] D. DeMers and K. Kreutz-Delgado, "Canonical parameterization of excess motor degrees of freedom with self-organizing maps," *IEEE Transactions on Neural Networks*, vol. 7, no. 1, pp. 43–55, 1996.

[5] J. P. Cusumano and P. Cesari, "Body-goal variability mapping in an aiming task," *Biological cybernetics*, vol. 94, no. 5, pp. 367–379, 2006.

[6] M. Benzaoui, H. Chekireb, and M. Tadjine, "Redundant robot manipulator control with obstacle avoidance using extended jacobian method," in *18th Mediterranean Conference on Control & Automation (MED)*. IEEE, 2010, pp. 371–376.

[7] S. E. Khadem and R. Dubey, "A global redundant robot control scheme for obstacle avoidance," in *IEEE Conference Proceedings Southeastcon.* IEEE, 1988, pp. 397–402.

[8] J.-O. Kim and P. K. Khosla, "Real-time obstacle avoidance using harmonic potential functions," *IEEE Transactions on Robotics and Automation*, vol. 8, no. 3, pp. 338–349, 1992.

[9] A. A. Maciejewski and C. A. Klein, "Obstacle avoidance for kinematically redundant manipulators in dynamically varying environments," *The international journal of robotics research*, vol. 4, no. 3, pp. 109–117, 1985.

[10] A. Hirakawa and A. Kawamura, "Trajectory planning of redundant manipulators for minimum energy consumption without matrix inversion," in *Proceedings of IEEE International Conference on Robotics and Automation*, vol. 3, 1997, pp. 2415–2420 vol.3.

[11] A. R. Hirakawa and A. Kawamura, "Proposal of trajectory generation for redundant manipulators using variational approach applied to minimization of consumed electrical energy," in *1996 4th International Workshop Proceedings on Advanced Motion Control, AMC-MIE*, vol. 2. IEEE, 1996, pp. 687–692.

[12] M. Shibata and K. Ohnishi, "Time-optimal trajectory planning for robot manipulators based on the distortive configuration space method," in *20th International Conference on Industrial Electronics, Control and Instrumentation, IECON*, vol. 2, 1994, pp. 1052–1057 vol.2.

[13] D. Verscheure, B. Demeulenaere, J. Swevers, J. De Schutter, and M. Diehl, "Time-optimal path tracking for robots: A convex optimization approach," *IEEE Transactions on Automatic Control*, vol. 54, no. 10, pp. 2318–2327, 2009.

[14] A. Ata and M. Sa'adah, "Soft motion trajectory for planar redundant manip-

ulator," in *9th International Conference on Control, Automation, Robotics and Vision, ICARCV*, 2006, pp. 1–6.

[15] H. Tanaka, M. Takahara, and M. Minami, "Trajectory tracking control redundant manipulators based on avoidance manipulability," in *SICE 2004 Annual Conference*, vol. 3, 2004, pp. 1962–1967 vol. 3.

[16] J. Kim, G. Marani, W. K. Chung, and J. Yuh, "A general singularity avoidance framework for robot manipulators: task reconstruction method," in *IEEE International Conference Proceedings on Robotics and Automation, ICRA*, vol. 5, 2004, pp. 4809–4814 Vol.5.

[17] R. Stevenson, B. Shirinzadeh, and G. Alici, "Singularity avoidance and aspect maintenance in redundant manipulators," in *7th International Conference on Control, Automation, Robotics and Vision, ICARCV*, vol. 2, 2002, pp. 857–862 vol.2.

[18] M. T. Turvey, "Coordination." *American psychologist*, vol. 45, no. 8, p. 938, 1990.

[19] P. Morasso, "Spatial control of arm movements," *Experimental Brain Research*, vol. 42, no. 2, pp. 223–227, 1981.

[20] M. C. Tresch, P. Saltiel, and E. Bizzi, "The construction of movement by the spinal cord," *Nature neuroscience*, vol. 2, no. 2, pp. 162–167, 1999.

[21] M. L. Latash, *Neurophysiological basis of movement*. Human Kinetics Urbana Champaign, IL, 1998.

[22] S. Arimoto, "A natural resolution of Bernsteîn's degrees-of-freedom problem in case of multi-joint reaching," in *IEEE International Conference on Robotics and Biomimetics, ROBIO*. IEEE, 2004, pp. 88–95.

[23] N. Bernshteîn, *The co-ordination and regulation of movements*. Pergamon Press, 1967.

[24] N. A. Bernsteîn, *Dexterity and its development*. Psychology Press, 1996.

[25] H. T. A. Whiting, *Human motor actions: Bernsteîn reassessed*. Access Online via Elsevier, 1983.

[26] O. Sporns and G. M. Edelman, "Solving Bernsteîn's problem: A proposal for the development of coordinated movement by selection," *Child development*, vol. 64, no. 4, pp. 960–981, 1993.

[27] M. L. Latash, "Flexion-reflex of the limb, crossed extension-reflex, and reflex stepping and standing," *Journal of Physiology*, vol. 40, pp. 28–121, 1910.

[28] L. H. Ting and J. L. McKay, "Neuromechanics of muscle synergies for posture and movement," *Current opinion in neurobiology*, vol. 17, no. 6, pp. 622–628, 2007.

[29] L. H. Ting, "Dimensional reduction in sensorimotor systems: a framework for understanding muscle coordination of posture," *Progress in brain research*, vol. 165, pp. 299–321, 2007.

[30] W. A. Lee, "Neuromotor synergies as a basis for coordinated intentional action," *Journal of Motion Behaviour*, vol. 16, no. 2, pp. 135–170, 1984.

[31] M. L. Latash, "Motor synergies and the equilibrium-point hypothesis," *Motor control*, vol. 14, no. 3, p. 294, 2010.

[32] M. C. Tresch and A. Jarc, "The case for and against muscle synergies," *Current Opinion in Neurobiology*, vol. 19, no. 6, pp. 601 – 607, 2009, motor systems Neurology of behaviour. [Online]. Available: http://www.sciencedirect.com/science/article/pii/S095943880900124X

[33] J. Konczak and J. Dichgans, "The development toward stereotypic arm kinematics during reaching in the first 3 years of life," *Experimental Brain Research*, vol. 117, no. 2, pp. 346–354, 1997.

[34] D. R. Lametti and D. J. Ostry, "Postural constraints on movement variability," *Journal of neurophysiology*, vol. 104, no. 2, pp. 1061–1067, 2010.

[35] J. Won and N. Hogan, "Stability properties of human reaching movements," *Experimental Brain Research*, vol. 107, no. 1, pp. 125–136, 1995.

[36] T. Kaminski and A. Gentile, "A kinematic comparison of single and multijoint pointing movements," *Experimental brain research*, vol. 78, no. 3, pp. 547–556, 1989.

[37] D. Whitney, "Resolved motion rate control of manipulators and human prostheses," *IEEE Transactions on Man-Machine Systems*, vol. 10, no. 2, pp. 47–53, 1969.

[38] T. Yoshikawa, "Manipulability of robotic mechanisms," *The international journal of Robotics Research*, vol. 4, no. 2, pp. 3–9, 1985.

[39] S. Jeon, "Recursive field estimation and tracking for autonomous manipulation," *Robotica*, vol. 30, no. 5, pp. 743–753, 2012.

[40] C.-C. Cheah, "Task-space pd control of robot manipulators: unified analysis and duality property," *The International Journal of Robotics Research*, vol. 27, no. 10, pp. 1152–1170, 2008.

[41] S. Arimoto, J.-H. Bae, H. Hashiguchi, and R. Ozawa, "Natural resolution of ill-posedness of inverse kinematics for redundant robots under constraints," *Communications in Information & Systems*, vol. 4, no. 1, pp. 1–28, 2004.

[42] S. Monckton and D. Cherchas, "Jacobian transpose control: a foundation for multiagent manipulator control," in *IEEE International Conference on Systems, Man and Cybernetics, Intelligent Systems for the 21st Century*, vol. 4, 1995, pp. 3391–3396 vol.4.

[43] M. Takegaki, "A new feedback method for dynamic control of manipulators, asme," *Journal of Dynamic Systems, Measurment, and Control*, vol. 103, p. 119, 1981.

[44] J. Kober, E. Oztop, and J. Peters, "Reinforcement learning to adjust robot movements to new situations," in *Proceedings of the Twenty-Second international joint conference on Artificial Intelligence, vol. 3*. AAAI Press, 2011, pp. 2650–2655.

[45] J. Peters and S. Schaal, "Learning to control in operational space," *The International Journal of Robotics Research*, vol. 27, no. 2, pp. 197–212, 2008.

[46] S. Arimoto, M. Sekimoto, and K. Tahara, "Iterative learning without reinforcement or reward for multijoint movements: A revisit of Bernsteîn's DOF problem on dexterity," *Journal of Robotics*, vol. 2010, 2010.

[47] A. Spiers, G. Herrmann, C. Melhuish, and T. Pipe, "A neural network method of learning human motion by observation in operational space," in *2010 10th IEEE-RAS International Conference on Humanoid Robots (Humanoids)*. IEEE, 2010, pp. 86–91.

[48] C. Melchiorri and J. K. Salisbury, "Exploiting the redundancy of a hand-arm robotic system," 1990.

[49] R. Volpe and P. Khosla, "Manipulator control with superquadric artificial potential functions: theory and experiments," *IEEE Transactions on Systems, Man and Cybernetics*, vol. 20, no. 6, pp. 1423–1436, 1990.

[50] E. Rimon and D. Koditschek, "Exact robot navigation using artificial potential functions," *IEEE Transactions on Robotics and Automation*, vol. 8, no. 5, pp. 501–518, 1992.

[51] S. Arimoto, M. Sekimoto, H. Hashiguchi, and R. Ozawa, "Physiologically inspired robot control: A challenge to Bernsteîn's degrees-of-freedom prob-

lem," in *Proceedings of the 2005 IEEE International Conference on Robotics and Automation, ICRA*. IEEE, 2005, pp. 4500–4507.

[52] M. Sekimoto, S. Arimoto, S. Kawamura, and J.-H. Bae, "Skilled-motion plannings of multi-body systems based upon riemannian distance," in *IEEE International Conference on Robotics and Automation, ICRA*. IEEE, 2008, pp. 1233–1238.

[53] M. Sekimoto, S. Arimoto, B. I. Prilutsky, T. Isaka, and S. Kawamura, "Observation of human multi-joint arm movement from the viewpoint of a riemannian distance," in *ICCAS-SICE*. IEEE, 2009, pp. 2664–2669.

[54] H. Collewijn, C. J. Erkelens, and R. Steinman, "Binocular co-ordination of human horizontal saccadic eye movements." *The Journal of Physiology*, vol. 404, no. 1, pp. 157–182, 1988.

[55] F. Harashima and S. Suzuki, "Human adaptive mechatronics-interaction and intelligence," in *2006 9th IEEE International Workshop on Advanced Motion Control*. IEEE, 2006, pp. 1–8.

[56] S. Suzuki, F. Harashima, and K. Furuta, "Human control law and brain activity of voluntary motion by utilizing a balancing task with an inverted pendulum," *Advances in Human-Computer Interaction*, vol. 2010, 2010.

[57] W. Brockett, "Minimum attention control," in *Proceedings of the 36th IEEE Conference on Decision and Control*, vol. 3. IEEE, 1997, pp. 2628–2632.

[58] L. A. Montestruque and P. J. Antsaklis, "On the model-based control of networked systems," *Automatica*, vol. 39, no. 10, pp. 1837–1843, 2003.

[59] H. Rehbinder and M. Sanfridson, "Scheduling of a limited communication channel for optimal control," *Automatica*, vol. 40, no. 3, pp. 491–500, 2004.

[60] Y. Uno, M. Kawato, and R. Suzuki, "Formation and control of optimal trajectory in human multijoint arm movement," *Biological cybernetics*, vol. 61, no. 2, pp. 89–101, 1989.

[61] B. Xie, J. Zhao, and Y. Liu, "Human-like motion planning for robotic arm system," in *2011 15th International Conference on Advanced Robotics (ICAR)*. IEEE, 2011, pp. 88–93.

[62] S. Yamada, Y. Kanamaru, and K. Bessho, "The transient magnetization process and operations in the plunger type electromagnet," *IEEE Transactions on Magnetics*, vol. 12, no. 6, pp. 1056–1058, 1976.

[63] J. Walsh, *Asset Protection and Security Management Handbook*. CRC Press, 2002.

[64] G. Honey, *Electronic access control*. Newnes, 2000.

[65] A. A. Sivarao, Y. Taufik, R. K. Haery Ian, S. Tin, and U. T. M. Melaka, "Critical review of electro-mechanical door locking system and proposal towards development of innovative super energy saving door locking system," *International Journal of Engergy and Innovative Technology (IJEIT)*, vol. 2, no. 5, pp. 201–207, 2012.

[66] L. Pérez-Lombard, J. Ortiz, and C. Pout, "A review on buildings energy consumption information," *Energy and Buildings*, vol. 40, no. 3, pp. 394 – 398, 2008. [Online]. Available: http://www.sciencedirect.com/science/article/pii/S0378778807001016

[67] J. D. Rogers, R. I. Schermer, B. L. Miller, and J. F. Hauer, "30-MJ superconducting magnetic energy storage system for electric utility transmission stabilization," *Proceedings of the IEEE*, vol. 71, no. 9, pp. 1099–1107, 1983.

[68] P. Firpo and S. Savio, "Optimized train running curve for electrical en-

ergy saving in autotransformer supplied ac railway systems," in *International Conference on Electric Railways in a United Europe*, 1995, pp. 23–27.

[69] A. Novitskiy and H. Schau, "Energy saving effect due to the voltage reduction in industrial electrical networks," in *Electric Power Quality and Supply Reliability Conference (PQ), 2010*, 2010, pp. 67–72.

[70] M. S. Patwardhan, "Use of solar energy for electrical energy conservation: A case study," in *2011 Nirma University International Conference on Engineering (NUiCONE)*, 2011, pp. 1–5.

[71] P. Campo, M. Piotrowicz, W. Maranda, and P. Sekalski, "Energy saving by compensation of daylight deficiences in buildings," in *Proceedings of the 17th International Conference Mixed Design of Integrated Circuits and Systems (MIXDES)*, 2010, pp. 510–513.

[72] M. Fragano and P. Crosetto, "Solid state key/lock security system," *IEEE Transactions on Consumer Electronics*, no. 4, pp. 604–607, 1984.

[73] W. A. Wahyudi and M. Syazilawati, "Intelligent voice-based door access control system using adaptive-network-based fuzzy inference systems (ANFIS) for building security," *Journal of Computer Science*, vol. 3, no. 5, pp. 274–280, 2007.

[74] I.-K. Hwang and J.-W. Baek, "Wireless access monitoring and control system based on digital door lock," *IEEE Transactions on Consumer Electronics*, vol. 53, no. 4, pp. 1724–1730, 2007.

[75] A. N. Rimmer, "Access control violation prevention by low-cost infrared detection," in *Defense and Security*. International Society for Optics and Photonics, 2004, pp. 823–830.

[76] E. O. Ranft, G. Van Schoor, and C. d. Rand, "Self-sensing for electro-

magnetic actuators. part ii: Position estimation," *Sensors and Actuators A: Physical*, vol. 172, no. 2, pp. 410–419, 2011.

[77] B. Hanson and M. Levesley, "Self-sensing applications for electromagnetic actuators," *Sensors and Actuators A: Physical*, vol. 116, no. 2, pp. 345–351, 2004.

[78] K. Sivadasan, "Analysis of self-sensing active magnetic bearings working on inductance measurement principle," *IEEE Transactions on Magnetics*, vol. 32, no. 2, pp. 329–334, 1996.

[79] M. Ehsani, I. Husain, and A. B. Kulkarni, "Elimination of discrete position sensor and current sensor in switched reluctance motor drives," *IEEE Transactions on Industry Applications*, vol. 28, no. 1, pp. 128–135, 1992.

[80] Z. Sun, N. C. Cheung, J. Pan, S. Zhao, and W.-C. Gan, "Design and simulation of a magnetic levitated switched reluctance linear actuator system for high precision application," in *IEEE International Symposium on Industrial Electronics, ISIE*. IEEE, 2008, pp. 624–629.

[81] D. Vischer and H. Bleuler, "Self-sensing active magnetic levitation," *IEEE Transactions on Magnetics*, vol. 29, no. 2, pp. 1276–1281, 1993.

[82] T. Mizuno, K. Araki, and H. Bleuler, "Stability analysis of self-sensing magnetic bearing controllers," *IEEE Transactions on Control Systems Technology*, vol. 4, no. 5, pp. 572–579, 1996.

[83] N. Morse, R. Smith, B. Paden, and J. Antaki, "Position sensed and self-sensing magnetic bearing configurations and associated robustness limitations," in *Proceedings of the 37th IEEE Conference on Decision and Control*, vol. 3. IEEE, 1998, pp. 2599–2604.

[84] A. Bissell, "Cusum techniques for quality control," *Applied Statistics*, pp. 1–30, 1969.

[85] R. Andre-Obrecht, "A new statistical approach for the automatic segmentation of continuous speech signals," *IEEE Transactions on Acoustics, Speech and Signal Processing*, vol. 36, no. 1, pp. 29–40, 1988.

[86] R. J. Di Francesco, "Real-time speech segmentation using pitch and convexity jump models: Application to variable rate speech coding," *IEEE Transactions on Acoustics, Speech and Signal Processing*, vol. 38, no. 5, pp. 741–748, 1990.

[87] M. Basseville, A. Benveniste, G. Moustakides, and A. Rougée, "Detection and diagnosis of changes in the eigenstructure of nonstationary multivariable systems," *Automatica*, vol. 23, no. 4, pp. 479–489, 1987.

[88] I. V. Nikiforov and I. N. Tikhonov, "Application of change detection theory to seismic signal processing," in *Detection of abrupt changes in signals and dynamical systems*. Springer, 1986, pp. 355–373.

[89] D. E. Gustafson, A. S. Willsky, J.-Y. Wang, M. C. Lancaster, and J. H. Triebwasser, "ECG/VCG rhythm diagnosis using statistical signal analysis-I. identification of persistent rhythms," *IEEE Transactions on Biomedical Engineering*, no. 4, pp. 344–353, 1978.

[90] M. E. Basseville and I. V. Nikiforov, "Detection of abrupt changes: theory and application," 1993.

[91] I. N. Gibra, "Recent developments in control chart techniques," *Journal of Quality Technology*, vol. 7, no. 4, pp. 183–192, 1975.

[92] S. Roberts, "Control chart tests based on geometric moving averages," *Technometrics*, vol. 1, no. 3, pp. 239–250, 1959.

[93] J. M. Lucas and M. S. Saccucci, "Exponentially weighted moving average control schemes: properties and enhancements," *Technometrics*, vol. 32, no. 1, pp. 1–12, 1990.

[94] E. Page, "Continuous inspection schemes," *Biometrika*, vol. 41, no. 1/2, pp. 100–115, 1954.

[95] M. A. Girshick and H. Rubin, "A Bayes approach to a quality control model," *The Annals of mathematical statistics*, vol. 23, no. 1, pp. 114–125, 1952.

[96] A. Shiryaev, "The problem of the most rapid detection of a disturbance in a stationary process," in *Soviet Math. Dokl*, vol. 2, no. 795-799, 1961.

[97] A. Wald, *Sequential analysis*. Courier Dover Publications, 2004.

[98] M. Pollak and D. Siegmund, "Approximations to the expected sample size of certain sequential tests," *The Annals of Statistics*, pp. 1267–1282, 1975.

[99] G. Lorden, "Procedures for reacting to a change in distribution," *The Annals of Mathematical Statistics*, pp. 1897–1908, 1971.

[100] T. L. Lai, "Sequential changepoint detection in quality control and dynamical systems," *Journal of the Royal Statistical Society. Series B (Methodological)*, pp. 613–658, 1995.

[101] T. Tanzawa and T. Tanaka, "A dynamic analysis of the dickson charge pump circuit," *IEEE Journal of Solid-State Circuits*, vol. 32, no. 8, pp. 1231–1240, 1997.

[102] K. Kashiwase, H. Kobayashi, N. Kuroiwa, N. Hayasaka, T. Myono, T. Suzuki, T. Iijima, and S. Kawai, "Dynamics of dickson charge pump circuit," in *Proceedings 15th Symposium on Circuits and Systems in Karuizawa*, 2002, pp. 375–380.

[103] M. K. Kazimierczuk and L. Starman, "Dynamic performance of pwm dc-dc boost converter with input voltage feedforward control," *IEEE Transactions on Circuits and Systems I: Fundamental Theory and Applications*, vol. 46, no. 12, pp. 1473–1481, 1999.

[104] I. Kondo, "Direct current booster with test circuit," May 30 1995, US Patent 5,420,505.

[105] D. Christiansen and D. G. Fink, *Electronics engineers' handbook*. McGraw Hill, 1997.

[106] N. R. Stansel, *Induction heating*. McGraw-Hill Book Company, 1949.

[107] J. Davies and P. Simpson, *Induction heating handbook*. IET, 1979.

[108] J. J. Feeley, "A simple dynamic model for eddy currents in a magnetic actuator," *IEEE Transactions on Magnetics*, vol. 32, no. 2, pp. 453–458, 1996.

[109] C. Dodd and W. Deeds, "Analytical solutions to eddy-current probe-coil problems," *Journal of applied physics*, vol. 39, no. 6, pp. 2829–2838, 1968.

[110] J. C. Young, S. D. Gedney, and R. J. Adams, "Eddy current analysis using a nyström-discretization of the volume integral equation," 2013.

[111] P. D. Agarwal, "Eddy-current losses in solid and laminated iron," *Transactions of the American Institute of Electrical Engineers, Part I: Communication and Electronics*, vol. 78, no. 2, pp. 169–181, 1959.

[112] Y. Yoshida, K. Nakamura, and O. Ichinokura, "A method for calculating eddy current loss distribution based on reluctance network analysis," *IEEE Transactions on Magnetics*, vol. 47, no. 10, pp. 4155–4158, 2011.

[113] L. Zhu and C. R. Knospe, "Modeling of nonlaminated electromagnetic suspension systems," *IEEE/ASME Transactions on Mechatronics*, vol. 15, no. 1, pp. 59–69, 2010.

[114] D. Ribbenfjard and G. Engdahl, "Novel method for modelling of dynamic hysteresis," *IEEE Transactions on Magnetics*, vol. 44, no. 6, pp. 854–857, 2008.

[115] J. Sykulski and R. Stoll, "Magnetic field modelling and calculation of reflected impedance of inductive sensors," *IEEE Transactions on Magnetics*, vol. 28, no. 2, pp. 1426–1429, 1992.

[116] S. Arimoto, H. Hashiguchi, and R. Ozawa, "A simple control method coping with a kinematically ill-posed inverse problem of redundant robots: Analysis in case of a handwriting robot," *Asian Journal of Control*, vol. 7, no. 2, pp. 112–123, June 2005.

[117] J. Scholz and G. Schoner, "The uncontrolled manifold concept: Identifying control variables for a functional task," *Experimental Brain Research*, vol. 126, pp. 289–306, 1999.

[118] S. Arimoto, H. Hashiguchi, M. Sekimoto, and R. Ozawa, "Generation of natural motions for redundant multi-joint systems: A differential-geometric approach based upon the principle of least actions," *Journal of Robotic Systems*, pp. 583–605, June 2005.

[119] M. Takegaki and S. Arimoto, "A new feedback method for dynamic control of manipulators," *Transactions of ASME Journal of Dynamic Systems, Measurement, and Control*, vol. 103, no. 2, pp. 119–125, 1981.

[120] Y. Asari, H. Sato, T. Yoshimi, K. Tatsuno, and K. Asano, "Development of model-based remote maintenance robot system. iv. a practical stiffness control method for redundant robot arm," in *Proceedings of the 1993 IEEE/RSJ International Conference on Intelligent Robots and Systems, IROS*, vol. 2, 1993, pp. 1245–1251 vol.2.

[121] S. A. A. Moosavian and E. Papadopoulos, "Modified transpose jacobian control of robotic systems," *Automatica*, vol. 43, no. 7, pp. 1226–1233, 2007.

[122] H. Kaneko, T. Arai, K. Inoue, and Y. Mae, "Real-time obstacle avoidance for robot arm using collision jacobian," in *1999 IEEE/RSJ International*

*Conference Proceedings on Intelligent Robots and Systems, IROS*, vol. 2. IEEE, 1999, pp. 617–622.

[123] M. Karimi and S. A. A. Moosavian, "Modified transpose effective jacobian law for control of underactuated manipulators," *Advanced Robotics*, vol. 24, no. 4, pp. 605–626, 2010.

[124] D. E. Chang and S. Jeon, "Damping-induced self recovery phenomenon in mechanical systems with an unactuated cyclic variable," *Journal of Dynamic Systems, Measurement, and Control*, vol. 135, pp. 021 011–1, 2013.

[125] T. Kane and M. Scher, "A dynamical explanation of the falling cat phenomenon," *International Journal of Solids and Structures*, vol. 5, no. 7, pp. 663–666, 1969.

[126] J. E. Marsden, "Geometric foundations of motion and control," *Motion, Control and Geometry*, pp. 3–19, 1997.

[127] C. Frohlich, "Do springboard divers violate angular momentum conservation?" *American Journal of Physics*, vol. 47, no. 7, 1979.

[128] D. E. Chang and S. Jeon, "On the damping-induced self-recovery phenomenon in mechanical systems with several unactuated cyclic variables," *arXiv preprint arXiv:1302.2109*, 2013.

[129] N. Elia and S. K. Mitter, "Stabilization of linear systems with limited information," *IEEE Transactions on Automatic Control*, vol. 46, no. 9, pp. 1384–1400, 2001.

[130] W. Prager, "Numerical computation of the optimal feedback law for nonlinear infinite time horizon control problems," *CALCOLO*, vol. 37, no. 2, pp. 97–123, 2000. [Online]. Available: http://dx.doi.org/10.1007/s100920070010

[131] C. Navasca and A. J. Krener, "Patchy solutions of hamilton-jacobi-bellman partial differential equations," in *Modeling, Estimation and Control*. Springer, 2007, pp. 251–270.

[132] D. L. Lukes, "Optimal regulation of nonlinear dynamical systems," *SIAM Journal on Control*, vol. 7, no. 1, pp. 75–100, 1969.

[133] C. Navasca and A. Krener, "Solution of hamilton jacobi bellman equations," in *Proceedings of the 39th IEEE Conference on Decision and Control*, vol. 1. IEEE, 2000, pp. 570–574.

[134] Y. Choi, W. K. Chung, and Y. Youm, "Robust control of manipulators using hamiltonian optimization," in *IEEE International Conference Proceedings on Robotics and Automation*, vol. 3. IEEE, 1997, pp. 2358–2364.

[135] S. Bordignon and M. Scagliarini, "Monitoring algorithms for detecting changes in the ozone concentrations," *Environmetrics*, vol. 11, no. 2, pp. 125–137, 2000.

[136] A. A. Sivarao, Y. Taufik, R. K. Haery Ian, S. Tin, and U. T. M. Melaka, "Critical review of electro-mechanical door locking system and proposal towards development of innovative super energy saving door locking system," *US Patent No*, vol. 6, no. 325,429, p. B1.

[137] *UL1034: Burglary-resistant electronic locking mechanisms*, Underwriters Laboratories (UL), Northbrook, Illinois, 2004.

[138] R. L. Stoll, *The analysis of eddy currents*. Clarendon Press Oxford, 1974.